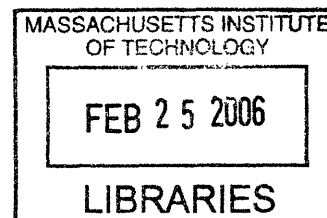# Continuous Flow Separation Techniques for Microchemical Synthesis

By

Jason G. Kralj

B.S. Chemical Engineering

Texas Tech University, 2000

Submitted to the Department of Chemical Engineering in Partial Fulfillment of the

Requirements for the Degree of

Doctor of Philosophy in Chemical Engineering

at the

MASSACHUSETTS INSTITUTE OF TECHNOLOGY

[February 2006]
December 2005

ARCHIVES

Author... 12/22/05

Jason G. Kralj
Department of Chemical Engineering
November 2005

Certified by.. 12/22/05

Klavs F. Jensen
Lammot duPont Professor of Chemical Engineering
Professor of Materials Science and Engineering
Thesis Supervisor

Certified by.. 12/22/05

Martin A. Schmidt
Professor of Electrical Engineering and Computer Science
Thesis Supervisor

Accepted by..

Daniel Blankschtein
Professor of Chemical Engineering
Chairman, Departmental Committee on Graduate Students

1

Continuous Flow Separation Techniques for Microchemical Systems

By

Jason G. Kralj

Abstract

Performing multistep microchemical synthesis requires many techniques from combining micromixers in series to the development of continuous microfluidic separation tools. Safety, high heat and mass transfer rates, and cost savings all continue to motivate microreactor development as a research tool, but many reactions generate a variety of (by)products including solid particles, immiscible fluids (gas and liquid), and miscible components requiring purification. We have endeavored to develop microfluidic systems which compliment existing microreactor technology, using forces that grow stronger with decreasing length scales such as electric fields and interfacial phenomena, and to use straightforward microfluidic mixers for kinetic studies of energetic material synthesis.

Dielectrophoresis was used to study the continuous separation of polystyrene particles based on size. Essentially, a microfluidic particle "ratchet" was created using a soft-lithography microchannel and slanted interdigitated electrodes which provide a transverse force component on the particles. Experimental behavior agreed well with the model predictions, and 4 & 6 micron particles were continuously separated.

Liquid-liquid extraction is another useful tool for microchemical synthesis and well-suited to small length scales because high mass transfer rates can be attained. However, emulsion formation and phase separation can provide significant challenges to continuous processing. To address breaking emulsions, a microfluidic tool was developed that uses AC E-fields to enhance coalescence of emulsified phases even where high surfactant concentrations are present, transforming the flow regime from disperse to slug. Phase separation of immiscible fluids is achieved by interfacial tension using porous membrane films which selectively wet only one fluid phase. An integrated mixer-contactor-separator was fabricated and used to separate fluids with low interfacial tensions due to miscible components. Solvent extraction and solvent switching were demonstrated using the device, which help enable continuous multistep microchemical synthesis.

Kinetic studies and optimization of energetic material synthesis were performed with a relatively simple micromixers-in-series setup for diazotization and nucleophilic substitution reactions. Typical batch operation is performed in sub-ambient conditions with copper salts to precipitate the product and avoid degradation, resulting in a slow, hazardous, laborious synthesis. High heat and mass transfer enabled studying reaction temperatures at 30°C to obtain kinetic parameters for both reaction steps. In addition, an

optimum pH range for the substitution reaction was found, which will lead to a streamlined, faster process.

Though still early in their development, these new tools will hopefully open the door to a range of new chemical syntheses and applications under conditions unachievable on the macroscale. Full integration of these technologies will enable multistep chemistry in microfluidic systems, which in turn will allow screening of new compounds, synthesis optimization, and reduction in chemical waste in a safe, efficient platform usable by chemists and biologists.

Thesis Supervisors: Klavs F. Jensen, Martin A. Schmidt

Acknowledgements

The years of my PhD study have been quite pleasant at times. Mostly, this has been quite a difficult and humbling experience. I was naïve when I first arrived at MIT (and probably still am), with little idea of the magnitude of the challenges that lay ahead of me. Because of that, I've had to rely a great deal on my mentors, friends, and family. Without their help, I could not have achieved as much as I have. Thank you.

I owe a great deal of thanks to Klavs for his guidance, patience, and support. His high standards and ability to maintain perspective on a problem while paying attention to detail (and explaining how to do all this) has helped me immeasurably to become a better researcher.

My co-advisor, Marty Schmidt, and my thesis committee, Professors Daniel Blankschtein and Pat Doyle, have provided useful feedback throughout my studies. Their insightful questions usually left me feeling a bit uneasy about my work, but I now understand that their intentions were always to help me think and grow as a researcher. I'm glad they always believed in my work and abilities.

I thank the faculty and staff of the Microsystems Technology Laboratories (MTL) for their help and expertise. I cannot imagine how any of the devices used in this thesis would have been made without their help.

Several members of the group, past and present, have also helped me along the way. Whether teaching me how to draw a photomask, staying late in the fab, collaborating on a project, or just listening to my problems, they've been a great resource. I hope to always be surrounded by such talented and brilliant people. Chapter 2 is the result of many hours of experimental work by Mike Lis, a high school senior at the time, whose tireless work ethic helped drive that project forward. Chapter 4 was done in collaboration with Hemantkumar Sahoo. His ability to look at problems from their fundamentals surely saved us weeks of frustration from failed experiments. And Chapter 5 was done in collaboration with Ed Murphy, whose approach of keeping problems small and simple helped keep us focused.

The first year "Goon Squad" gets special thanks for helping me through that first semester. I don't know how they've put up with me for this long without beating me with a stick. Thanks also to the Hampshire Street Poker Club and the Thirsty Ear Pub for giving my mind a break from silicon and separations. I will always remember my time here and the many friends I've made.

To my parents Ray and Sharon Kralj, I wish to express my sincerest gratitude. They have been supportive throughout my life. You always encouraged me to learn and try new things, which seems to have sunk in. And to the rest of my family, thank you for keeping me grounded and being so supportive.

And, of course, my thanks to Marianne for her love and support. She means the world to me.

Table of Contents

Table of Figures

11

13

14

16

Chapter 1. Introduction

1.1 Microchemical Systems

Microchemical systems, or microfluidic systems for chemistry, have developed rapidly over the last decade. The hallmark of microchemical systems is the small length scale (10^{-6} - 10^{-4} m) of the features found in these devices. Such small length scales give access to a wide range of phenomena not typically observed at larger length scales. For example, surface and viscous forces usually dominate gravitational and inertial forces, sometimes requiring development of different techniques for chemical processing.

Devices are fabricated from a range of materials including glass, silicon, polymer, and metal to meet application-specific needs such as high heat transfer rates, chemical inertness, durability, or disposability. Similar to microelectromechanical systems (MEMS), microfluidics utilize many of the fabrication techniques found in integrated circuit processing, primarily photolithography and etching [1, 2].

Microchemical systems have excellent performance with respect to heat/mass transfer, safety, and reagent utilization made possible by the small volumes of material used. As a result, systems can be run under conditions that could be dangerous on the benchtop. Microreaction technology has been applied to several chemical applications such as high density portable power generation [3, 4]; testing of small amounts of catalyst

17

[5-7]; low waste, reagent utilization, and fast reaction space scanning for reaction optimization [8]; and low-volume chemical synthesis [9-11]. Integrated detection and online monitoring such as Raman, IR, and UV-Vis spectroscopy enable *in situ* chemical measurements for chemical kinetics and reaction mechanism studies that are difficult to study in other systems [12, 13]. It is clear that microchemical systems are gaining acceptance in the chemical community and will become increasingly useful as research and industry adopt high-throughput screening methods and "green chemistry" protocols.

1.2 Motivation for Multistep Microchemical Processing

It is becoming increasingly important to improve the rate of new materials screening and synthesis optimization for scaleup to production. In particular, synthesis optimization is often a labor-intensive trial-and-error process and sometimes never fully achieved. On the benchtop scale, the number of parameters that can be adjusted per day in a synthesis is small. Also, the use of pilot plants to optimize a process before taking it to production scale is still common. These setups consume large amounts of material and adapt slowly to changing conditions, making it difficult for engineers to properly design a process. Perhaps the worst-case scenario of multistep processing is one where a recipe-specific process with little or no kinetic data or reaction pathway is used. This can result in batch processing that needlessly takes days to complete instead of hours or even minutes. Thus, development of chemistry tools capable of adjusting conditions quickly with fast sample collection rates and parallel operation can have a significant impact on the time required to optimize a specific chemical synthesis pathway.

1.3 Motivation for Continuous-flow Microfluidic Separators

The focus of work in microchemical systems has begun to shift towards multistep chemical synthesis (i.e. total synthesis). Multistep processing requires separations technologies analogous to distillation and extraction that complement the existing microreactors. However, separations techniques to connect reaction steps largely do not exist. Design rules and robust devices have not been developed, and there are few demonstrations of the integration of separation and reaction units. Generally, three different kinds of separators exist for microfluidic applications: batch separation (e.g. chromatography), separating particles from suspensions, and continuous multiphase extractions. This thesis focuses primarily on contributions to continuous particle and continuous liquid-liquid extraction.

1.3.1 Solid Particle Sorting

Solid particle separations in microchannels involve sorting a variety of compounds including crystallized species, biological particles (whole cells and organelles), and polymeric beads. Traditional sieving is difficult and sedimentation is too slow and imprecise. Microfluidic platforms offer perhaps the best control for particle sorting on the 0.1-10 μm length scale due to the laminar flow behavior and length scales comparable to the particle sizes. The selection criteria can vary, with common examples including size/shape [14-16] and fluorescence (i.e. cytometry) [17]. There are inherent difficulties to working with solids in microchannels, including significant wall-interactions due to the high surface-to-volume ratio typical of microdevices and clogging. For these reasons, it is common to use dilute concentrations of particulate matter,

surfactants, and maintain channel sizes several orders of magnitude larger than the solid species.

Particle sorting on the microscale requires use of two forces of approximately equal magnitude, where at least one of those forces can be adjusted. Typically, hydrodynamic drag is one of the forces and resists particle motion. The second force finding favor in the microfluidic community is dielectrophoresis because it is driven by large E-field gradients easily generated in microdevices, and separation depends on the material properties of the particle and surrounding medium instead of surface charge.

Microparticle sorting techniques can generally be applied across different applications, and validation of each technique is commonly accomplished using polymer beads that are readily available, can be functionalized with different surface groups, and tagged with fluorescent compounds. Modeling of device behavior with these particles allows researchers to apply new sorting techniques to application-specific systems, but this is often done at a level insufficient to fully describe the physics in the system. Understanding the limitations, scaling of the forces, and resulting complete behavior is critical to gaining insight into the actual performance and gives a measure of predictability for other related systems.

1.3.2 Continuous Multiphase Extraction

1.3.2.1 Fluid Contacting for Mass Transfer

Continuous chemical separations processes, such as liquid-liquid extraction, have two major process steps that must be addressed: mixing/fluid contacting, and phase separation [18]. Mixing is a diffusive process by nature, and the rate of mixing scales

20

with the square of the characteristic length. Small length scales inherent to microfluidic systems facilitate good mixing and decrease processing times through high mass transfer rates. When this thesis work began, contacting of immiscible fluids for high mass transfer rates in multiphase reactions had recently been demonstrated using hydrogenation reactions [19]. Burns and Ramshaw were among the first to exploit high mass transfer for separations by performing a single-step extraction. In their system, they found slug flow could efficiently be used for liquid-liquid contacting because of the internal recirculation of the slugs and short length scales for diffusion and penetration of the chemical species of interest [20]. Others have devised a variety of systems for the contacting of immiscible fluids, including the aforementioned slug flow, laminar co-current and counter-current flow, and emulsification [21-25]. In these works, single-step processes such as solvent extraction, impurity removal, and product purification have been demonstrated. Laminar flow of two immiscible fluids is difficult to maintain without surface modifications because of the energy penalty in generating contiguous surface areas compared with slugs. Also, laminar flow tends to have diffusion-only mass transfer, resulting in poor performance; though phase separation is somewhat easier because of the laminar behavior. By comparison, emulsions have very good mass transfer because of large surface-to-volume ratios and characteristic length scales smaller than the microfluidic channels. However, phase separation is more difficult because the droplets must first be coalesced and then separated. Thus, improved utilization of the high mass transfer rates in continuous microfluidic systems requires new insights and techniques for phase separation.

1.3.2.2 Phase Separation

The second step in an extraction process, phase separation, is complex and requires the management of multiple phenomena such as surface tension and fluid dynamics. In single-phase flow, fluids can be controlled in a microdevice by adjusting the channel size and length to affect the pressure drop. In multiphase flow systems, interfacial and surface forces must also be included in the analysis, especially in microfluidic systems where those forces are much stronger than those generated by hydrodynamic pressure. In addition, one or more forces that act preferentially on one of the phases and scale favorably with decreasing length scales are required to induce phase separation. Generally, the lack of continuous, robust methods to perform phase separation has prevented chemical extraction from being implemented in multistep syntheses.

As already mentioned, dispersed phases are known to provide good mixing on the macroscale because of high surface-to-volume ratios. These phases tend to coalesce rapidly settle out by gravity in traditional macroscale chemical processing equipment such as distillation and extraction columns. On the microscale, coalescence does not occur on-chip because droplets follow streamlines in the laminar flow and typically interact little without some external force. Moreover, systems using surfactants to generate dispersed flow present a challenge because they can be slow to coalesce [26]. The process flow is broken because fluids must be collected and allowed to settle before further processing.

In addition, surface forces dominate gravitational forces at small length scales. This is equivalent to a zero-gravity environment and makes separation using sedimentation slow or even impossible. Thus, microchemical systems require an entirely

22

different method of phase separation. Jhunjhunwala found that surface forces could be used in combination with capillary structures to separate the phases for gas-liquid flow [27]. For gas-liquid systems this principle works well, as the surface energies of each phase are very different, allowing most liquids to wet common materials such as glass, metals, and plastics. Liquid-liquid systems, though, are more difficult to control because the phases have similar surface energies, giving much smaller forces to drive this type of separation. Overcoming this challenge enables the use of extraction and other multiphase liquid-liquid flow applications, such as phase transfer reactions, where phase separation is required for multistep synthesis.

1.4 Thesis Objectives and Overview

The main objective of this thesis is to develop and characterize chemical and physical separations in microfluidic systems for use in multistep chemical synthesis. By examining the fundamental issues that impede linking reactors to separators, I identify several challenges. A secondary objective is to use phenomena that scale favorably with decreasing size rather than try to recreate traditional unit operations for separation. In doing so, it is possible to generate simple solutions to the aforementioned challenges that take advantage of the small length scales rather than view them as an obstacle. Where possible, I use well-established theory describing the fundamental phenomena to explain experimental results and behavior observed in these systems. Important design parameters and challenges affecting separator performance are also documented for the development of future work in the area of continuous-flow microfluidic separators.

The next chapter describes the work undertaken to use dielectrophoresis in a microdevice for the manipulation and separation of microparticles based on size

23

differences. The device behavior is described using a theoretical model for particle motion and compared with experimental behavior. Particle separation is also achieved using the same device design. Chapters 3 and 4 describe our study of two major issues limiting the use of continuous flow extraction in microchemical systems. First, the use of emulsions for extraction is studied including examination of extraction enhancement using surfactants and the subsequent demulsification of the two phases using electric fields. Next, liquid-liquid phase separation is studied in systems where differences in interfacial forces and wetting properties act as the driving force. Model solvent extraction processes are studied using substantial fractions of partially miscible components, including mixing and mass transfer effects. By using these chemical mixtures, we aim to address the issues likely to exist in multistep chemical processing. Chapter 5 examines a multistep synthesis process using energetic materials and intermediates. Studying the kinetics of such systems is enabled by microreaction technology due to improved safety. Moreover, optimization of a multistep synthesis can be rapidly achieved using microdevices. Last, Chapter 6 summarizes and draws conclusions from this thesis and discusses the prospects for continued work in microseparations and multistep microchemical systems. The appendicies include detailed fabrication processes, photolithography masks, packaging schemes for the devices, and material stability studies

Chapter 2. Continuous Dielectrophoretic Size-Based Particle Sorting

2.1 Introduction

The need to separate micron sized objects, e.g., cells and crystals, drives advances in microfluidic systems for particle separations [28]. Manipulation and sorting of 0.1-10 μm particles is difficult by mechanical methods such as sieving or sedimentation. The small dimensions of microfluidic channels have advantages for particle separation since flow is laminar profile and large electric fields can be realized. In particular, dielectrophoresis (DEP) has proved useful for manipulating micron sized particles [29-31]. The DEP force on a body results from a non-uniform electric field, and it is attractive (positive) or repulsive (negative) depending on the relative dielectric behavior of the particle in the surrounding medium. A variety of microfluidic systems have been devised to manipulate and sort biological material, such as whole cells and organelles. These devices typically rely on hydrodynamic drag and a unique electrode structure to generate electric field gradients that separate particles into different positions in the moving fluid. There are several examples using DEP in combination with pressure-driven flow for field-flow fractionation [32-36], in continuous flow with deflector

structures [16, 37], with electrophoresis and insulating post arrays [15, 38], for cell traps [39, 40], and for separation by frequency effects [41-43].

Analysis and simulation of the particle behavior in microdevices have shown several effective approaches to achieve particle separation, each with advantages and difficulties [31, 44, 45]. It was concluded that a top-and-bottom electrode structure performs superior to the planar array for negative DEP because stronger E-field gradients are generated and particles are forced away from walls where non-uniform flow and non-specific particle adhesion can occur. However, compared with a simple planar electrode array, top-and-bottom electrodes are difficult to fabricate because the array must be aligned and sealed carefully. Custom systems must be designed for these purposes, and the overall process is slow. As an alternative, a planar electrode array generates sufficiently strong E-field gradients to realize DEP in microfluidic channels fabricated using soft-lithography techniques. The simple geometry facilitates modeling of the E-fields, allowing rapid simulation of the DEP force and particle motion.

Here, continuous-flow size-based dielectrophoretic particle sorting and manipulation is both modeled and demonstrated in a microfluidic device. Polystyrene micro spheres suspended in a neutrally-buoyant aqueous solution flow continuously across an array of slanted, planar, interdigitated electrodes. The behavior of a single particle bead is modeled using a force balance between DEP and hydrodynamic drag. Particles experience a transverse dielectrophoresis force that depends on particle size and electric-field strength. Larger particles are deflected more than smaller particles, and consequently, particles suspensions are separated by size into different transverse positions as they flow down the length of the device. This behavior was verified by

experimentally tracking the flow of monodisperse particle suspensions through the device. We also demonstrated the separation of 4 and 6 micron particles under continuous flow conditions. The model predicts that the transverse particle displacement in the interdigitated electrode device has a 4th order size and voltage dependence, which provides particle separation with high sensitivity with potential applications in biological and crystal separations.

2.2 Experimental

2.2.1 Device Fabrication

Device fabrication involved two parts, fabrication of the electrodes and the microfluidic channel. First, the planar electrode array, 50 μm wide, 50 μm spaced, with a 45 degree slant over a 10 x 30 mm area (see Figure 2.1), was created on a 150-mm Pyrex 7740 wafer (Bullen Ultrasonics; Eaton, OH). Negative photoresist was spincoated to ~ 2 μm thickness, then exposed and developed to define the electrode structures for a lift-off process. The wafer was subsequently subjected to e-beam deposition of platinum (100 nm thickness with a 10 nm titanium adhesion layer). Acetone was used to remove the photoresist and excess metal to complete the liftoff, and individual devices were cut with a diesaw. Wires were attached to the electrodes using silver-filled conductive epoxy (McMaster-Carr; Atlanta, GA).

Microfluidic channels were molded by soft-lithography techniques [46]. SU-8 10 photoresist (MicroChem Corp.; Newton, MA) was spincoated to the desired thickness (~28 μm), and processed using the supplier's recipe. The fabricated channels were 500 μm wide and 28 μm deep. The SU-8 master mold was silanized using n-octyl-

27

triethoxysiloxane (United Chemical Technologies, Inc.; Bristol, PA) before molding with degassed polydimethylsiloxane (PDMS, mixed 10:1 w/w with its activator, Dow Corning; Midland, MI) to ensure good release. The PDMS was then baked for ~ 3 hours at 70°C in an oven. The devices were diced by razor blade, inlet and outlet holes were made with a punch, and the surfaces cleaned with Scotch tape (3M; St. Paul, MN) before oxygen plasma ashing for 35 s. The PDMS and electrode array were then contacted to create a permanent seal. Finally, Upchurch tubing (PEEK, 1/16" OD) for fluid connections was attached by epoxy (Oak Harbor, WA) (Figure 2.1).

2.2.2 Particle Separation Experiments

A syringe pump (KD Scientific; Holliston, MA) delivered liquid to the device. Hamilton gas-tight syringes (Hamilton; Reno, NV) of 1 and 5 mL sizes were used for the solutions. A B&K 4017 function generator (B&K Precision Corporation; Yorba Linda, CA) delivered the voltage to the device with a peak-to-peak maximum of ~ 12 V and frequency range of 0.1-10 MHz. Digital images were captured using a Coolpix 990 digital camera (NikonUSA; Melville, NY) in combination with a Leica MZ12 stereoscope (Leica Microsystems Inc.; Bannockburn, IL) (Figure 2.2).
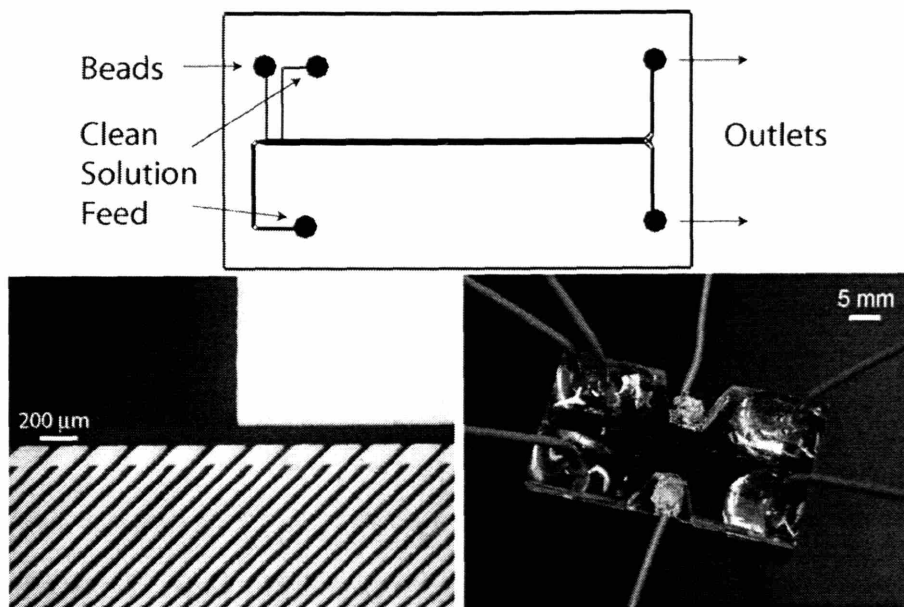
Figure 2.1 Schematic of the device with three inlets and two outlets (top). The stream carrying the beads is flow focused away from the wall to avoid sidewall effects. The channels are cast in PDMS and placed upon an array of electrodes (bottom-left). The packaged microfluidic device (bottom right) has a footprint of 40x25 mm.
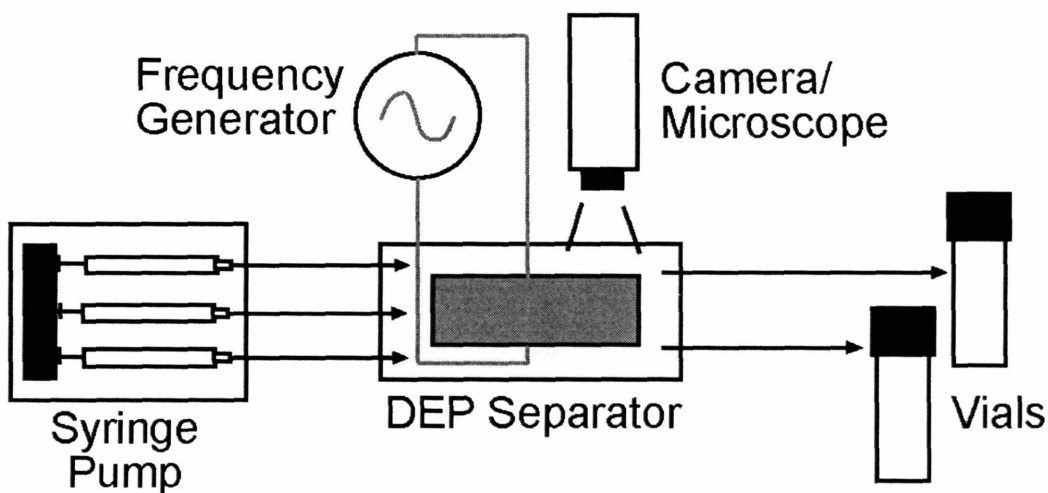
Figure 2.2 Schematic of experimental setup

The system was operated using pressure-driven flow and negative DEP. Use of high frequency (~1 MHz) AC fields prevented electrolysis, Joule heating, and double-

29

layer effects [28]. The polystyrene particle suspensions contained different sizes of spheres (2, 4.13, 5.09, 5.63, and 6.02 μm, Bangs Laboratories; Fishers, IN) and were diluted in an aqueous solution of DI water with 0.01 wt% Tween 20 (JT Baker, Phillipsburg, NJ) and sucrose (~0.15-0.16g per 1g H_2O; Mallinckrodt, Hazelwood, MO) to bring the specific gravity to 1.06. Typical suspension concentrations were ~10^{-4} vol/vol. In all experiments, we used low bead concentrations so that particle-particle interactions could be considered negligible [47]. Beads readily adhered to the channel walls in the absence of surfactant. Any adhering beads could easily be removed using a combination of sonication and flowing 1% surfactant solution, which enabled reuse of the devices.

Typical total flowrates were 0.7-5.6 μl/min. Flow-focusing was used on the particle stream entering the device at a 5:1:1 ratio (fluid:beads:fluid) to move them away from the wall (Figure 2.3). Initial experiments without flow focusing showed that particles near the sidewall were trapped due to non-uniform E-fields near the corners. After focusing, the average initial position of the beads is 21.4% into the channel.

Particle motion in the device was quantified using digital videos. The videos were exported to Adobe ImageReady (Adobe; San Jose, CA) for image analysis where the image scale factor was calculated and individual particles traced. A baseline reference video was taken under zero-voltage conditions (flow only) to ensure steady state before beginning experiments. The data from ~30 particles were averaged at each flowrate/voltage condition from video clips of 30-45 seconds. The outlet locations were recorded and statistical regression performed on the data to determine the effects of

voltage, flow rate, and particle radius. At each set of experimental conditions, the statistical average was determined along with a 95% confidence interval (Student t-test).
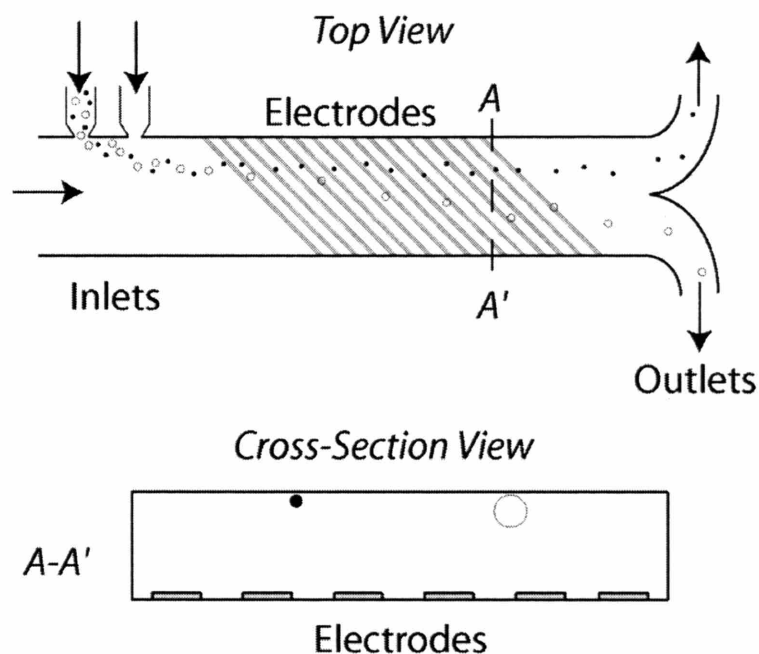
Figure 2.3 (Top) A schematic showing flow-focusing of the bead suspension at the inlets, separation of the particles across the electrodes, and flow splitting using the laminar flow profile. Arrows indicate the direction of fluid flow. (Bottom) A cross-sectional view of the flow channel showing the locations of the planar electrodes and the beads during operation.

2.2.3 Device Simulation

The system of ordinary differential equations describing the particle trajectories was integrated numerically using Maple8 software (MapleSoft; Waterloo, ON, Canada) with a 4th order Runga-Kutta Fehlberg method. The E-field was modeled using FEMLAB (Comsol; Burlington, MA) with the Electromagnetics module for predicting the electrostatic behavior. We used a two-dimension model (described in the following

section) with symmetry boundary conditions, reflecting the periodic structure of the array.

2.3 Theoretical Analysis and Results

2.3.1 Theoretical Model of Device Performance

2.3.1.1 Dielectrophoretic Force

In order to gain insight into the performance of the DEP device, we developed a model describing the hydrodynamic and dielectrophorectic forces determining the particle flow paths in the microfluidic channel. The DEP force is described as follows: [30, 31]

$$\underline{F}_{DEP} = 2\pi R^3 \varepsilon_0 \varepsilon_1 \beta \underline{\nabla} \left| E^2 \right| \quad \text{with} \quad \beta \equiv \left(\frac{\varepsilon_2 - \varepsilon_1}{\varepsilon_2 + 2\varepsilon_1} \right) \tag{2.1}$$

Here R is the particle radius and ε_0 is the permittivity of free space. In the case of a polystyrene bead in water, the real part of the dielectric constants at 1.1 MHz are approximately $\varepsilon_2 = 2.5$ and $\varepsilon_1 = 80$ respectively. Examination of the DEP force term reveals that it is proportional to the cube of the particle radius. Second, the dielectric constants of the particle and surrounding medium play a significant role in the particle behavior. The Clausius-Mossotti factor, β as defined in Equation (2.1), can be positive or negative, thereby directing a particle either towards or away from field gradient maxima. For this system under the conditions described above, negative DEP (nDEP) will occur. Particles experiencing nDEP will be forced away from the electrode structures towards the channel

32

top, which has important implications in modeling the electric field and the hydrodynamic drag on the particles (see below).

The gradient in the electric field, $\nabla|E^2|$, acts to drive particle motion; this requires modeling the E-field. Rather than solve the E-field over the volume of the device, we simplified our analysis to 2-D using the periodic structure of the electrodes. A cross-section of the E-field perpendicular to the flow was solved using FEMLAB (see Figure 2.3a). Only the E-field near the channel top is relevant as nDEP drives particles away from the electrodes. Values of the square of the E-field at one particle radius from the top in the x-direction were extracted from the numerical model and closely resembled a sine wave with a period equal to the electrode spacing (Figure 2.4b). Moreover, in order to map the E-field along the length of the channel (the z-direction), a term was added adjusting the phase of the E-field with the position in the channel (Figure 2.5). The resulting approximation to $|E^2|$ then takes the form:

$$|E^2| = AV^2 \sin\left(\frac{2\pi z}{\lambda_z} - \frac{2\pi x}{\lambda_x}\right) + AV^2 \tag{2.2}$$

The amplitude of the wave is A, V is the voltage applied at the electrodes, and λ is the electrode spacing. The gradients of $|E^2|$ with respect to x (transverse to the flow) and z (parallel to the flow) are then:

$$\frac{\partial|E^2|}{\partial x} = \frac{2\pi}{\lambda_x} AV^2 \cos\left(\frac{2\pi z}{\lambda_z} - \frac{2\pi x}{\lambda_x}\right) \tag{2.3a}$$

$$\frac{\partial|E^2|}{\partial z} = -\frac{2\pi}{\lambda_z} AV^2 \cos\left(\frac{2\pi z}{\lambda_z} - \frac{2\pi x}{\lambda_x}\right) \tag{2.3b}$$

33

The height of the channel is an important model parameter since the magnitude of the E-field and the E-field gradient decreases roughly inversely with channel height.
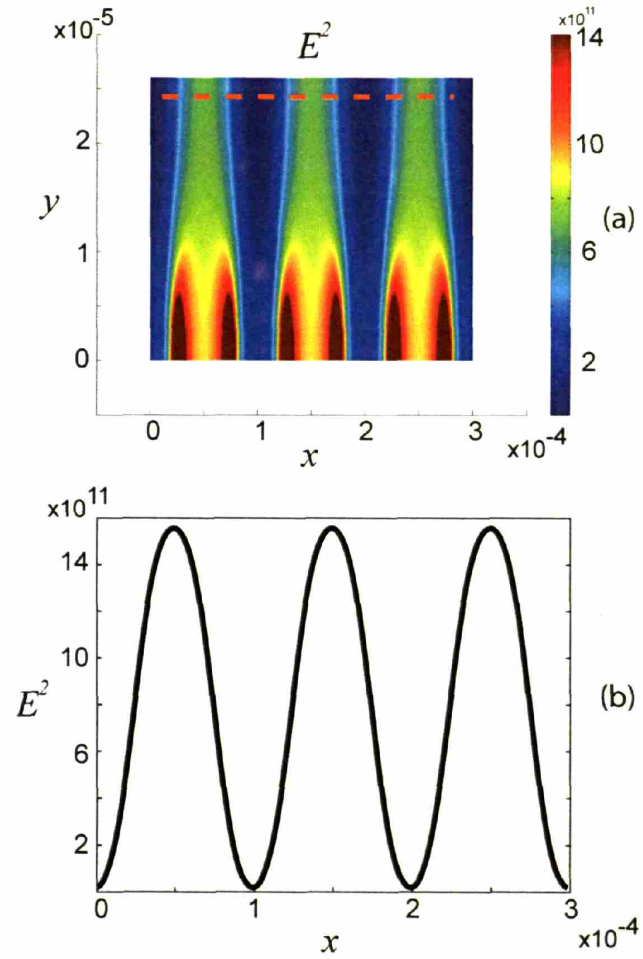
Figure 2.4 FEM Model of E^2 in the channel cross section for an applied voltage of 10V (a), with E^2 values extracted 3 μm from channel top (b). At this height in the channel, the E^2 can be represented by a sine wave.
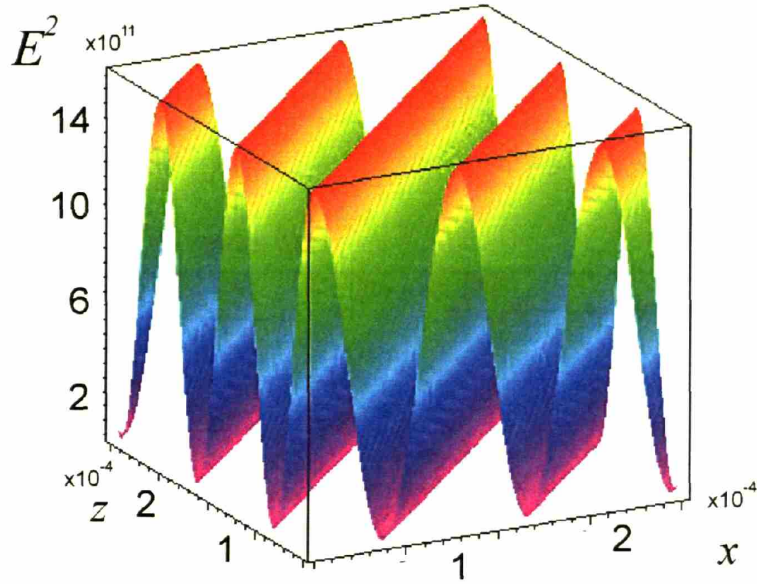
Figure 2.5 The periodic electrode structure requires fitting the E-field to the geometry. The amplitude and position are normalized to the maximum value of E^2 and channel width, respectively.

2.3.1.2 Hydrodynamic Drag Force

We neglect gravity since the particles are density matched with an aqueous sucrose solution. This addition of sucrose lowers the dielectric constant of the water ~10% [48]. Because the particle Reynolds number (*Re*) is < 0.01 at all times, viscous forces dominate and Stokes law describes the viscous drag force: [49]

$$\underline{F}_{drag} = -6\pi\mu R\underline{v} \tag{2.4}$$

The viscosity of the solution is μ, particle radius is R, and the particle velocity vector is $\underline{v}$.

The large aspect ratio (~20:1) gives a flow profile similar to that of parallel-plate geometry except for a region next to the side walls of width equal to ~ one channel height

35

[49]. As a result, the velocity profile is parabolic between the channel top and bottom. The nDEP force forces the particles toward the E-field minima, here the channel top, causing particles of different size to flow at different velocities when subjected to the same flowrate (Figure 2.6).
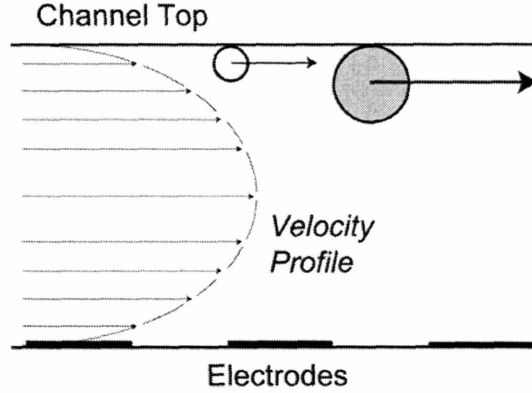
Figure 2.6 Particles of different size flow at different velocities when subjected to the same flowrate in a parabolic velocity profile.

In addition, the proximity of the particle to the channel wall causes an increase of the viscous drag [50]. Happel and Brenner show that particles very near the wall, ~1% of a particle radius from the channel top, the calculated drag force would be ~3 times greater than if the particle were flowing in the bulk.

2.3.1.3 Force Balance

At steady state, the DEP force is balanced by the viscous drag.

$$\underline{F}_{DEP} + \underline{F}_{drag} = 0 \tag{2.5}$$

Substituting Equations (2.1) and (2.4) yields:

$$6\pi\mu R\underline{v} = 2\pi R^3 \varepsilon_0 \varepsilon_1 \beta \underline{\nabla} \left| E^2 \right| \tag{2.6}$$

36

By inserting the approximation to $\nabla|E^2|$, Equations (2.3a) and (2.3b), and formulating the result in transverse (x) and length (z) coordinates, we obtained the flowing system of ordinary differential equations (ODEs) with the initial condition of an arbitrary displacement x_o and z_o.

$$v_x = \frac{dx}{dt} = \frac{2\pi R^2}{3\mu\lambda_x} \varepsilon_0 \varepsilon_1 \beta A V^2 \cos\left(\frac{2\pi z}{\lambda_z} - \frac{2\pi x}{\lambda_x}\right) \tag{2.7a}$$

$$v_z = \frac{dz}{dt} = v_o - \frac{2\pi R^2}{3\mu\lambda_z} \varepsilon_0 \varepsilon_1 \beta A V^2 \cos\left(\frac{2\pi z}{\lambda_z} - \frac{2\pi x}{\lambda_x}\right) \tag{2.7b}$$

The extra velocity term in the z-direction arises from fluid convection in the absence of a field. The resulting set of coupled first-order ODEs were solved by numerical integration to obtain the x and z trajectories. Flow rate, particle size, and E-field strength affect the transverse particle displacement (Figure 2.7).
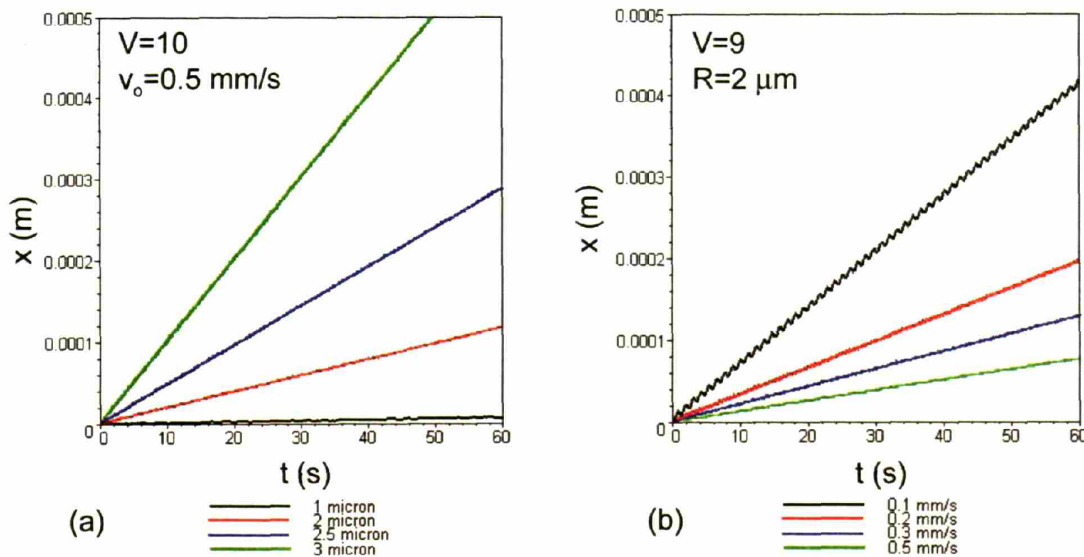
Figure 2.7 Model predictions showing the transverse particle displacements as a function of time for different particle sizes (a) and flow rates (b), holding other variables constant.

37

2.3.2 Analytical Solution Describing Particle Motion

It was possible to develop an analytical solution to the model can be developed if the second term on the right-hand side of Equation (2.7b) is small compared to v_o. This is the lubrication approximation, which is commonly used to simplify systems of ODEs where variations of one variable are of a different scale than the other [49]. In this case, v_z reduces to v_o and z becomes $v_o t$. Inserting this result into Equation (2.7a) leads to the following expression:

$$v_x = \frac{dx}{dt} = \frac{2\pi R^2}{3\mu\lambda_x}\varepsilon_0\varepsilon_1\beta A V^2 \cos\left(\frac{2\pi v_o t}{\lambda_z} - \frac{2\pi x}{\lambda_x}\right) \tag{2.8}$$

The solution takes the form:

$$x = v_o t - \frac{2}{w_1}\arctan\left(\frac{\sqrt{C^2 v_o{}^2 - 1}}{C v_o + 1}\tan\left(\frac{w_1\sqrt{C^2 v_o{}^2 - 1}}{2C}t\right)\right) \tag{2.9}$$

$$with \quad \frac{1}{C} = \frac{2\pi R^2}{3\mu\lambda_x}\varepsilon_0\varepsilon_1\beta A V^2$$

The arctan function is piecewise continuous and has a half period every

$$t = \frac{(2N+1)\pi}{w_1\sqrt{v_o{}^2 - \frac{1}{C^2}}} \quad N \geq 0 \tag{2.10}$$

A plot of Equation (2.9) shows the behavior of the function (Figure 2.8).
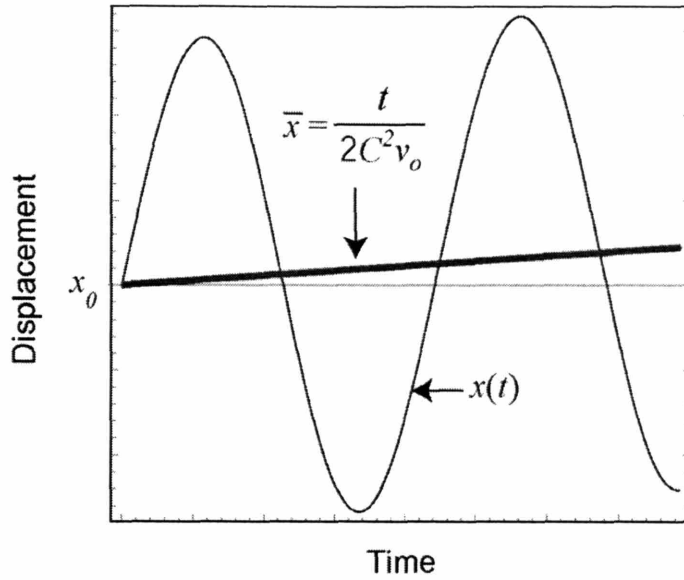
Figure 2.8 The general behavior of the function x from Equation 2.9 and the approximation for the average displacement $\bar{x}$ from Equation 2.11.

The average displacement ($\bar{x}$) is estimated in terms of a line that passes through the function at each point of discontinuity. The slope of that line ($\bar{m}$) gives the scaling of the system, which can be expanded with a Taylor series about $1/C^2=0$.

$$\bar{x} = v_o t - \frac{\pi}{w_1}, \quad \bar{m} = \frac{\bar{x}}{t_1} = v_o - \sqrt{v_o^2 - \frac{1}{C^2}} = \frac{1}{2C^2 v_o} + O\left(\frac{1}{C^4}\right) \tag{2.11}$$

For values of $1/C < 0.5\ v_o$, less than 1% error is introduced into $\bar{m}$. Typical values for $1/C$ are less than $0.02\ v_o$.

Substitution of the original terms for C reveals the particle displacement at the outlet of the device has a 4th order dependence on voltage and size, and a 2nd order dependence on flow rate.

$$x\Big|_{outlet} = m\frac{L}{v_o} = \frac{\left(\dfrac{2\pi}{3\mu\lambda_x}\varepsilon_0\varepsilon_1\beta A\right)^2 L}{2} R^4 V^4 \frac{}{v_o^2} \tag{2.12}$$

L is the total length of the channel. Other parameters of the system, the dielectric constant and viscosity of solution and electrode spacing, also have a 2nd order effect on the particle displacement. Equation (2.12) shows that reductions in the viscosity and electrode spacing could increase particle displacement, while lowering the dielectric constant can decrease particle displacement.

2.4 Results and Discussion

2.4.1 Particle Separation Experiments

A particle mixture containing 4.13 and 6.02 μm particles (referred to as 4 and 6 um hereafter) was processed in order to demonstrate the separation of two distinctly different particle sizes. The theoretical model suggested good separation would be possible at 10V and 4 μL/min. Experimentally, we found that the desired separation could be achieved at an applied voltage of 10V and flowrate of 1.5 μL/min. Visual inspection confirmed the particles were separated at the end of the channel and flowed through different outlets (Figure 2.9). Though the flowrates of the model and experiments differ by ~2.7x, the model provided a good initial estimate for the experimental conditions required to induce separation in this system.
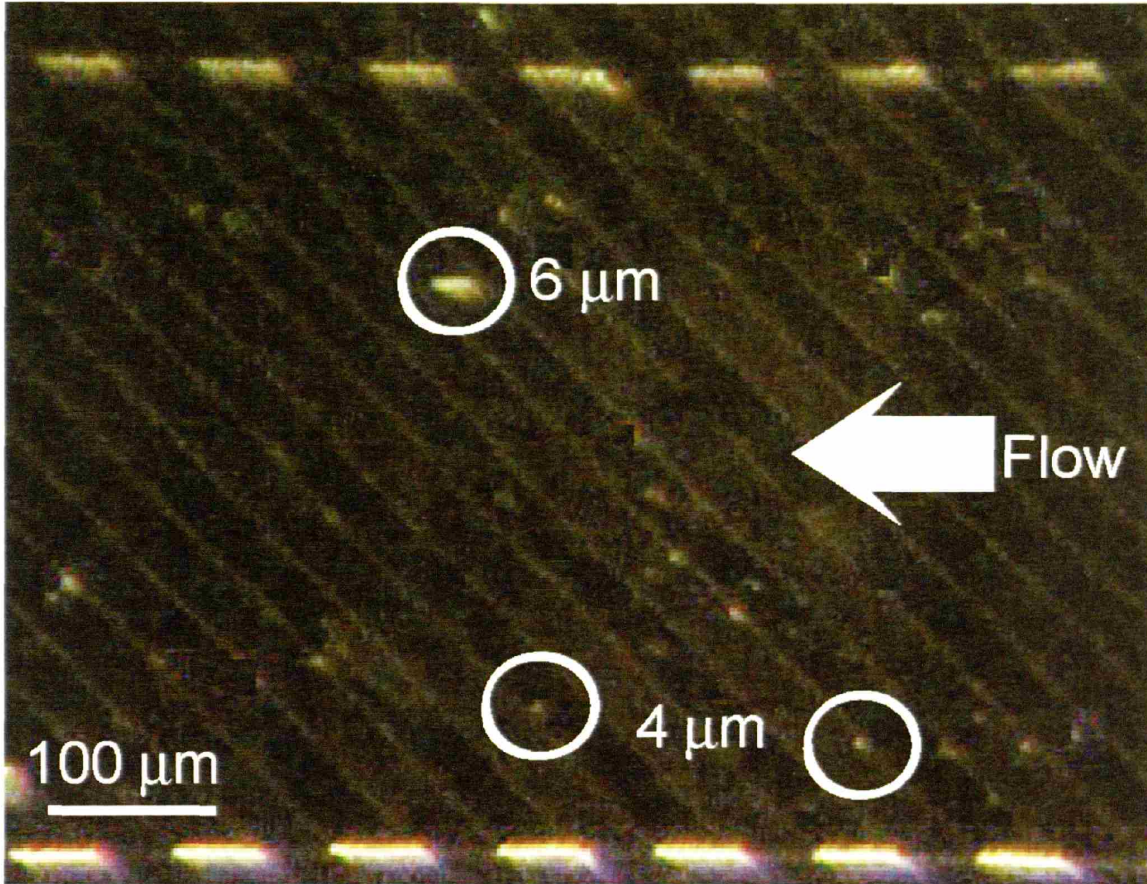
Figure 2.9 Snapshot of 4 and 6 μm particles after separation near the device outlet.

2.4.2 Single-Sized Particle Behavior

Experimental results agreed well with the theoretical model. We first examined the limiting cases when the hydrodynamic drag force is either much less than or much greater than the DEP force. At low flowrates we observed all beads being deflected across the channel by the first few electrodes. This agrees with previous findings when the DEP force is much stronger than the drag force [16]. At high flowrates we observed no deflection of the beads. We also noticed that the beads traveled at a velocity corresponding to 2.5-3 times less than the predicted value from the parabolic velocity

profile, confirming enhanced drag effects due to the particles' close proximity to the channel top.

We next quantified device behavior under conditions where the DEP force was strong enough to deflect particles a fraction of the channel width. Using the scaling arguments determined theoretically in Equation (2.12), the total transverse particle displacement (x) was scaled by R^4 and V^4. Individual data sets showed the V^4 and flowrate dependencies (Figure 2.10). All data were plotted with the theoretical model values on a log-log scale vs. the inverse flowrate (Figure 2.11). The slope of the model line is 2, indicating a square dependence on the inverse flowrate. A statistical regression of the data gives an average slope of 1.70 ± 0.20, giving good agreement with the model. The most likely sources of error are the uncertainty of the exact initial position of the particles entering the microchannel, channel height, solution dielectric constant, and solution viscosity.
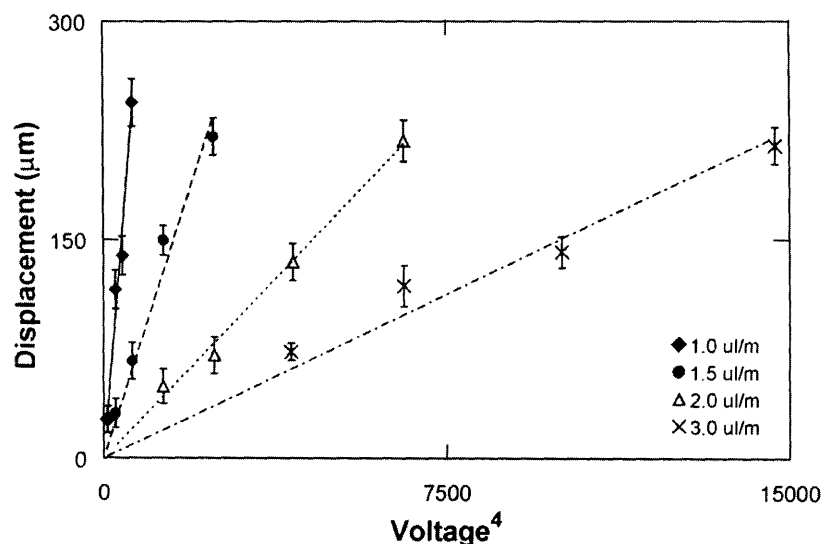
Figure 2.10 Data showing the voltage and flowrate dependencies on transverse displacement of 6 μm particles.

42

10^{18}

10^{17}

10^{16}

10^{15}

10^{14}

10^{13}

o Data
----- Average
· 95% CI
— Model

x_{final}/V^4R^4

Inverse Velocity $(m/s)^{-1}$

100   1000   10000   100000
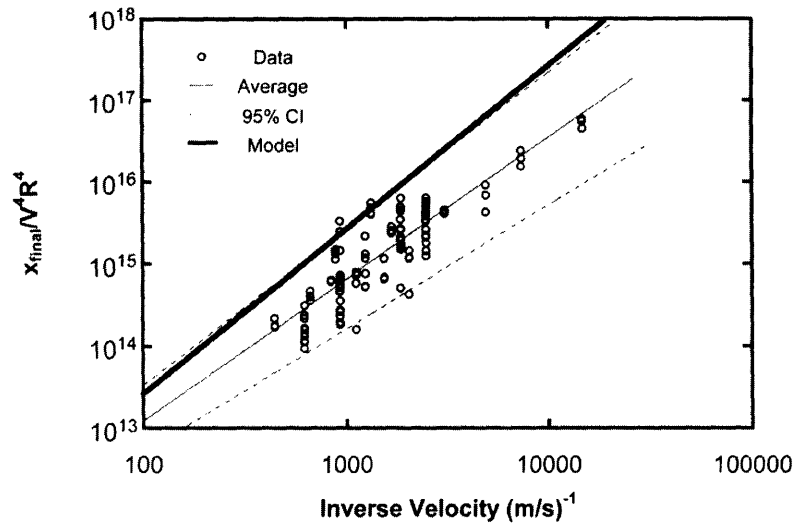
Figure 2.11 Data and model values show good agreement. The slope of the model on the log-log plot is 2, while the regression of the data is 1.7±0.2. All units are SI.

2.5 Conclusions

We have constructed a microfluidic device that creates an asymmetric body force using DEP and hydrodynamic drag on solid microparticles to translate them across a thin channel. The device has a simple design and can easily be fabricated using metal lift-off and soft-lithography techniques. Slanted, narrowly-spaced, interdigitated electrodes were critical features of the design. The small spacing allowed fabrication of 300 electrodes along the length of the device, each generating large asymmetric E-field gradients to drive DEP.

We developed a theoretical model for the particle behavior in the device. An analytical solution of the particle displacement as a function of time revealed a 4th order voltage and particle size dependence, and a 2nd order flowrate dependence. The fluidic device was used to separate of a mixture of 4 and 6 μm particles with parameters from

43

the model used as initial estimates for the flowrate and voltage used in the experiment. The model was further verified experimentally by measuring the average transverse displacement of nearly-monodisperse particles in solution for a range of particle sizes, applied voltages, and flowrates.

The device design and model could be applied to similar particle-solvent systems, such as crystals in solution and aqueous biological systems. In particular, the model could be used to aid the design of DEP separator devices using only the physical parameters of the system. Further reductions in the electrode spacing and channel height would make it possible to separate smaller particle mixtures with good efficiency.

Chapter 3. Electric-field Enhanced Coalescence for Surfactant-Enhanced Liquid-Liquid Extraction

3.1 Motivation for E-field Enhanced Coalescence of Disperse Phases

Microfluidic separation techniques have been demonstrated for analysis on chip [51], but continuous chemical separation methods still need to be developed for on-chip multi-step chemical synthesis. Microfluidic extraction separation methods typically take advantage of the high surface-to-volume ratio (S/V) inherent in microchannels. Co-flowing streams typically have to be stabilized by surface modifications - for example the hydrophobic nature of the solvent channel is enhanced along with the hydrophilic character of the aqueous channel to prevent the interface from undulating and ultimately breaking into segments of alternating immiscible fluids (slug flow). A typical co-flowing microfluidic device allows mass transfer along a small interface, with a diffusion path length roughly corresponding to the width of the fluid - usually 10-100 μm. Surface modification can also provide sufficient stabilization to allow counter-current extraction over a small range of flow conditions [23].

Slug flow can be advantageous in separation processes since internal recirculation in the slugs increases mixing and consequently mass transfer between slugs and the

45

surrounding fluid [52, 53]. Dispersed flow in which droplets are smaller than the channel diameter offers potentially further improvement in separation speed. The time to equilibrium scales with the diffusive path length squared. Therefore, if a droplet of radius 20 μm is created, the extraction time would be expected to decrease ~ 25-fold compared to a 100 μm wide flow. For typical liquid-phase diffusion coefficients, the two phases would equilibrate in less than one second.

The use of droplets to enhance extraction is a common procedure in conventional laboratory practice. A mixture of two immiscible liquids (e.g., organic and aqueous) are shaken to create droplets, which are then allowed to coalesce and the two continues phases are separated through a funnel. However, this process is often frustrated by the formation of a stable emulsion that can be difficult to break, especially when surfactants are employed. Such emulsions can persist from minutes to weeks or even be thermodynamically stable. Similar issues would be expected to arise in microsystems when creating highly dispersed microdroplets. Therefore, an active system promoting coalescence would have to be a critical element in any emulsion enhanced liquid-liquid separation scheme. Otherwise, any improvement in extraction would be more than offset by the difficulty of breaking the emulsion.

Electric fields have been used to remove water from organic liquids since the early 20th century for dewatering of crude oil [54]. Applying large voltages across a tube with crude cause water droplets to agglomerate, coalesce, and settle [55]. The important factor in this electrocoalescence (EC) process is the electric field (E-field). For oilfield production purposes, typical E-field strengths are 10-100 kV/m, usually applied as thousands of volts over several centimeters. Producing the same E-field in a microfluidic

system requires only ~10 V because of the small electrode spacing ~100 μm. The EC phenomenon itself is complex and has been studied for dilute emulsion systems [56]. However, for most systems relevant to chemical synthesis (volume fractions >1%), multibody interactions present significant challenges for quantitative modeling of the coalescence behavior. Use of alternating current (AC) eliminates electrolysis of water observed in some systems with high water fractions [55].

The formation of emulsions is enhanced by the use of the surfactants, and the presence of these surfactants can further increase the separation efficiency through reverse micelle extraction (RME). When the surfactant concentration is raised above its critical micelle concentration (CMC), sphere-like micelles form and can be used to entrap and improve the extraction of hydrophilic compounds. Examples include the removal of antibiotics from an aqueous fermentation broth [57] and the removal of dyes from an aqueous phase [58]. With proper selection of surfactants and concentrations, it is possible to use surfactants to both stabilize the disperse flow and increase extraction efficiency.

Microfluidic systems have previously been used to create emulsions [59, 60]. Here, we used a simple magnetically-stirred micromixer and focused on the design and microfabrication of a new microfluidic device for demulsifying a dispersed phase by electrocoalescence. Reproducibly breaking emulsions is shown to be possible even at high surfactant concentrations. As case studies, the emulsion based extraction procedure is applied to the extraction of phenol and p-nitrophenol from an aqueous phase to an organic phase. Finally, a general model for the reverse micelle enhanced extraction is formulated to determine the extraction efficiency for each organic/aqueous/surfactant system.

3.2 Microfluidic Electrocoalescer Design

The device is designed to take an emulsion and use electric fields to coalesce many small droplets into larger droplets and allow gravity separation outside of the device (Figure 3.1). An electric potential is applied on the sidewalls to generate the electric fields that enhance droplet interaction and coalescence.
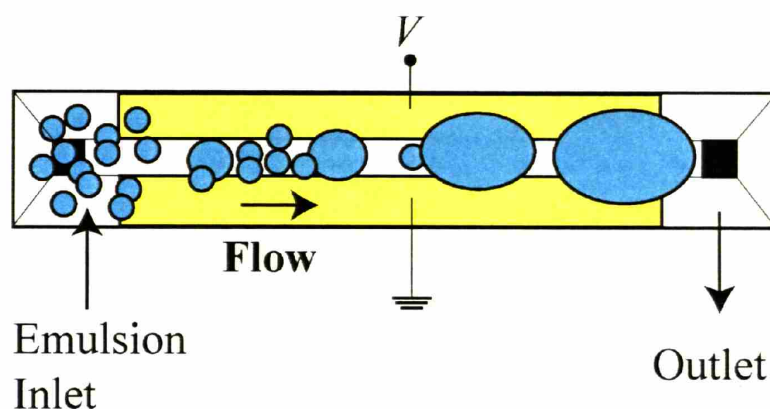
Figure 3.1 Schematic showing the device operation. A water-in-oil emulsion (blue spheres) enters the device and flows across electrodes patterned on the sidewalls of the channel (yellow), which cause the conductive aqueous droplets to coalesce. After the droplets become large slugs, they pass out of the device.

Fabrication of the microfluidic separation device (see Figure 3.2) began with three 150 mm double side polished (100) silicon wafers (SiliconQuest) coated with 200 nm stoichiometric silicon nitride deposited by chemical vapor deposition and a 150-mm Pyrex 7740 wafer (Bullen Ultrasonics) with holes predrilled for electrical and fluidic access. Using standard photoresist, we patterned channels on the first wafer (I), inlet ports on the second wafer (II), and a shadow mask on the third silicon wafer. The silicon nitride was etched in the open areas by SF_6 plasma. Next, all three wafers were etched anisotropically through the entire wafer in a hot 20% KOH solution (80° C, 8 hr). The

48

remaining nitride was removed using 85% phosphoric acid at 120° C. The resulting channel dimensions were 20 mm long, 650 μm deep, 100 μm wide at the bottom, and 970 μm wide at the top, corresponding to a total volume of ~ 35 μl. A 450 nm thermal oxide was then grown (1000°C, 66 m) on the channel and inlet ports wafers.
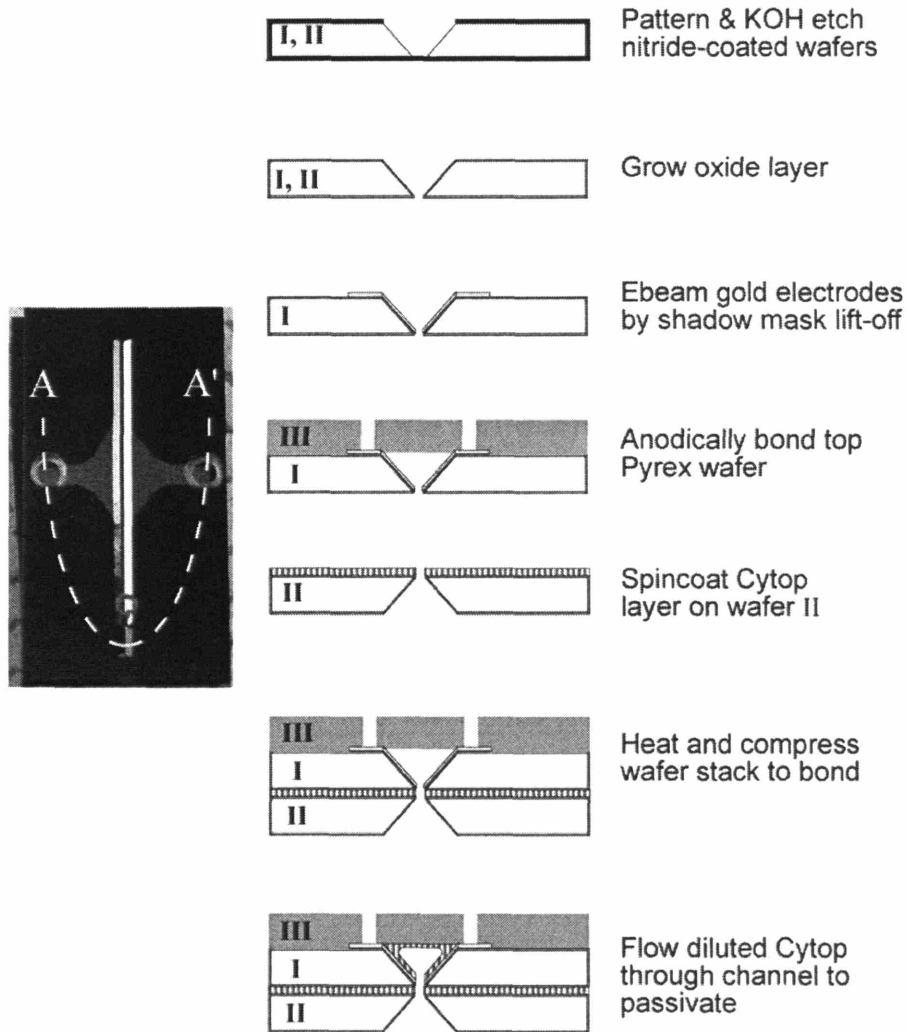
Figure 3.2 The general fabrication process using standard microfabrication tools is shown above (right). The view is through a cross-section of the device (left, A-A').

The electrodes were defined by aligning the shadow mask over the channels, then attaching with a small amount of photoresist as adhesive. The 100 nm gold electrodes

49

were then deposited on a 10 nm chromium adhesion layer by e-beam evaporation. The shadow mask was removed with acetone. The fluid channel was formed by anodic bonding of the channel wafer and the Pyrex wafer (III). Individual pieces of the wafer stack (I & III) and the inlet ports (II) were cut using a diesaw.

The inlet port layer (II) was affixed to the channel stack (I & III) with 9 wt% CYTOP (Asahi Glass Co), a fluoropolymer. The backside of the inlet ports (II) was coated with a thin layer of CYTOP and the solvent as evaporated in an oven at 90°C for 1-2 hr. The channel-Pyrex stack (I & III) was then aligned by microscope with the inlet ports. The resulting 3-wafer stack was subsequently placed carefully on a hotplate, ~ 20 kg weight added, and the temperature brought to ~ 200°C (above the reflow point of the polymer). After 4-6 hr, the temperature was decreased to ambient and the weight removed.

The electrodes in each individual device were passivated by a thin layer of CYTOP. A piece of 1/16" PEEK tubing (Upchurch) was affixed to the top Pyrex layer by epoxy. The fluid channel was filled with a dilute solution of CYTOP (1 wt%) and the device was then placed in a 70°C oven overnight to evaporate the solvent. The resulting thin fluoropolymer film prevented electrolysis and electrical short-circuiting of the devices.

3.3 Experimental Setup

Extraction generally follows a three-step process: phase contact, chemical equilibration, and phase separation. In particular, phase separation is often the most difficult step when dealing with dispersed flow for reasons already discussed. Hence,

development of the phase separation device is critical for microchemical extraction technology.

3.3.1 Experimental Conditions

In a typical electrocoalescence experiment, a mixture of HPLC grade hexane (>99.5% n-hexane and isomers, VWR Scientific), 1-10 wt% Span 80 (used as received, Asahi Chemical Co), and 0.1 M aqueous phosphate buffer solution (prepared using >99% mono- and dibasic sodium phosphate salts from Burdick & Jackson) were mixed in a 10:1 volumetric (v/v) ratio in a small magnetically-stirred vessel (300 μl) at a stirring rate of 500-800 rpm. The reagents were fed continuously to the mixer and the resulting water-in-oil emulsion was directed to the coalescence device at a flow rate of 55 μl/min. In each set of experiments, the flow rate, stirring speed, and fluid compositions were held constant and the applied voltage on the electrodes was varied.

As a model study, phenol and p-nitrophenol (>99% Aldrich Chemical) were extracted from an aqueous phase (5 mM phosphate buffer solution, pH 7) into hexane by varying the surfactant (Span 80) concentration 1-10 wt%. Total flowrates of organic and aqueous solutions were 30-60 μl/min at a 2:1 volumetric flow ratio. The initial aqueous-phase phenolic compound concentrations were 100 ppm. Analysis of the organic phase was performed using a Rainin Dynamax dual-pump HPLC with a Waters CN-HP column (3.9x150 mm). The flow schedule was 99.5%–95% (v/v) hexane/isopropanol at 1 ml/min total flow rate. The UV detection wavelength was 270 nm.

3.3.2 Device Packaging

The device was connected to macro-fluidic elements by compression sealing to a custom-made fluidic interface (Figure 3.3). This interface was constructed from aluminum, Plexiglas, and a Viton gasket, with machined ports for Upchurch ¼"-28 connectors. The electrodes were contacted to the device by pogo-pins (Interconnect Devices, Inc.) epoxied into the compression plate. These pins were subsequently connected with 50 Ω alligator clips to a function generator (BK Precision 4017) capable of 0-12 V and frequencies of 0.1 Hz - 2 MHz. Fluids were delivered with a syringe pump (Cole Parmer 74900 series) with Hamilton Gastight syringes. A Leica stereo-microscope MZ12 with a color CCD camera (COHU 2222-1000) was used to examine the device.

3.3.3 Modeling and Analysis

Femlab (Comsol) with the electromagnetics package was used to solve Maxwell's equations and model the quasisteady E-field. The droplet size in the emulsion entering into the separation device was characterized by digital still images obtained under no flow conditions. Device performance was characterized by recording movies and off-line determining droplet sizes in individual frames. Droplet sizes were measured by pixel width and height (Adobe ImageReady) and scaled using the known channel dimension. 8-20 droplets were measured over 8-15 images for statistical analysis using a Student t-test for 95% confidence interval.
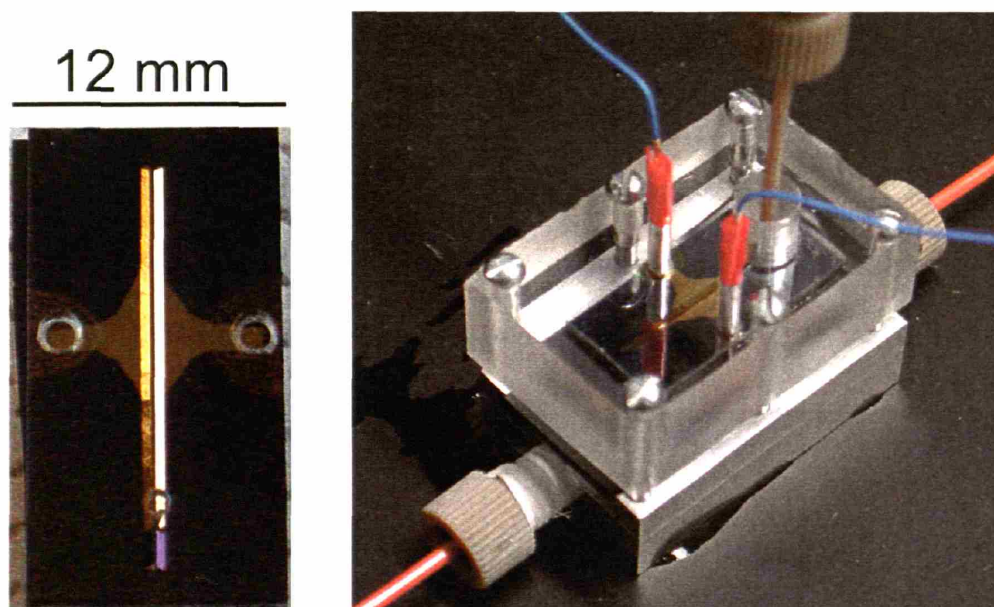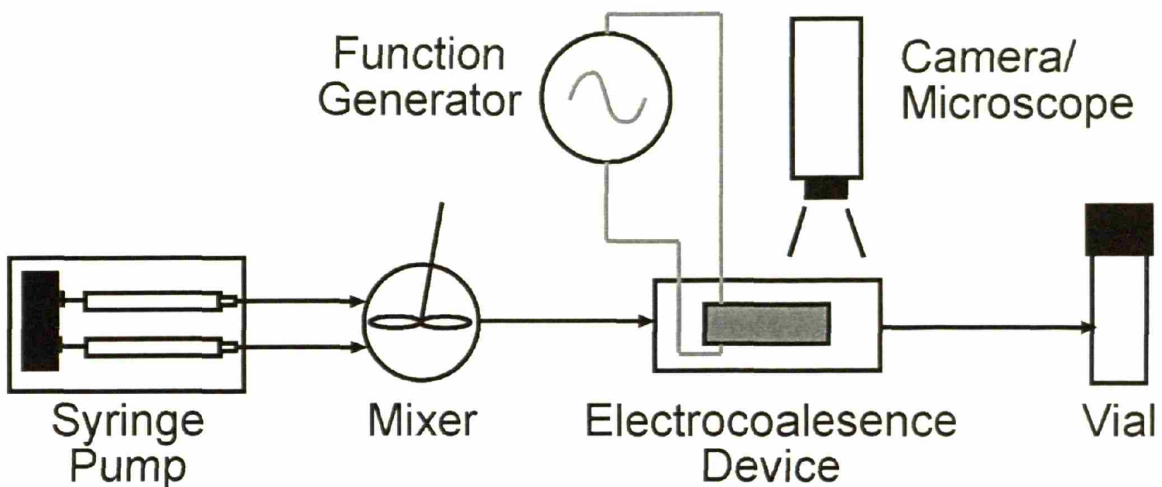
Figure 3.3 Experimental setup (top), finished device with large holes for electrical connections (bottom left), packaged device with fluidic connections and electrodes (bottom right).

3.4 Results

3.4.1 Electric Field Enhanced Coalescence

We identified E-fields capable of "breaking" a water-in-hexane emulsion. Under no applied E-field, the emulsion flowed through the device with no visible coalescence. When collected in vials the emulsions persisted for 5 days or more. Under low- to

moderate potentials (1-6 V) no significant coalescence was detected (see Figure 3.4 and Figure 3.6). Increasing the applied potential beyond 6 V led to rapid coalescence with large droplets. The average droplet size steadily increased with increasing voltage until the size became constrained by the channel width. The resulting increase in droplet size from ~50 μm to ~500 μm corresponds to a 1000-fold increase in droplet volume and can be readily collected and phase-separated. The V-shaped channel from the KOH etching was advantageous because the E-field was strongest where the aqueous droplets settled and collected (Figure 3.7). Inversion of the device significantly reduced the amount of coalescence corresponding with poorer device performance due to gravitational forces. In this case, gravitational forces are significant for the emulsified droplets because they do not interact with the channel surface until they coalesce. In addition, the aqueous phase does not wet the CYTOP-coated channel surface well.
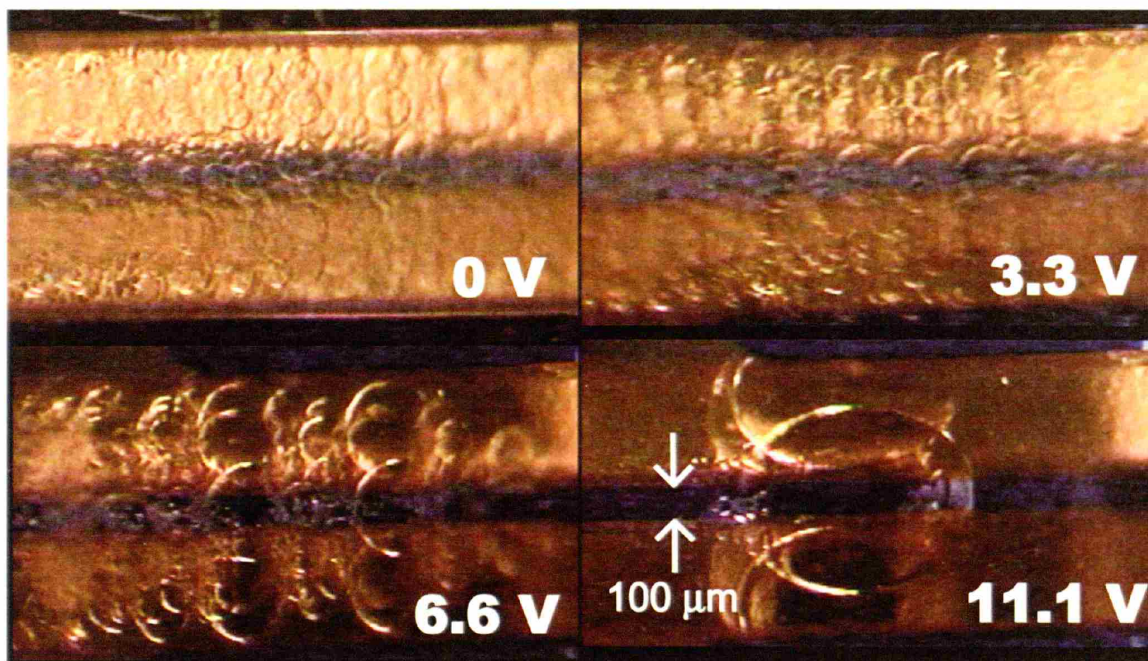
Figure 3.4 Droplets flowing at the outlet of the device. As the field strength increases, the droplets coalesce rapidly until single bubbles the size of the channel hydraulic diameter (slugs) form.

54

3.4.2 Theoretical Discussion of E-field Enhanced Coalescence

Davis [61] examined the forces and fields of two charged conducting spheres in a uniform E-field (Figure 3.5). He found that the E-field intensification between the two spheres results from the surface charges on the spheres separated by a dielectric medium and becomes stronger as the spheres approach each other and scales with the square of the inverse separation length (s), dielectric constant of the surrounding medium (ε_1), the square of the sphere radius (R), and square of the nominal electric field (E). In the absence of charge, the forces are described as follows, where a_j is the particle size, $F_{E,ij}$ are the force terms, ψ the angle of incidence of the E-field, and F_1, F_2, and F_3 complicated series expressions.
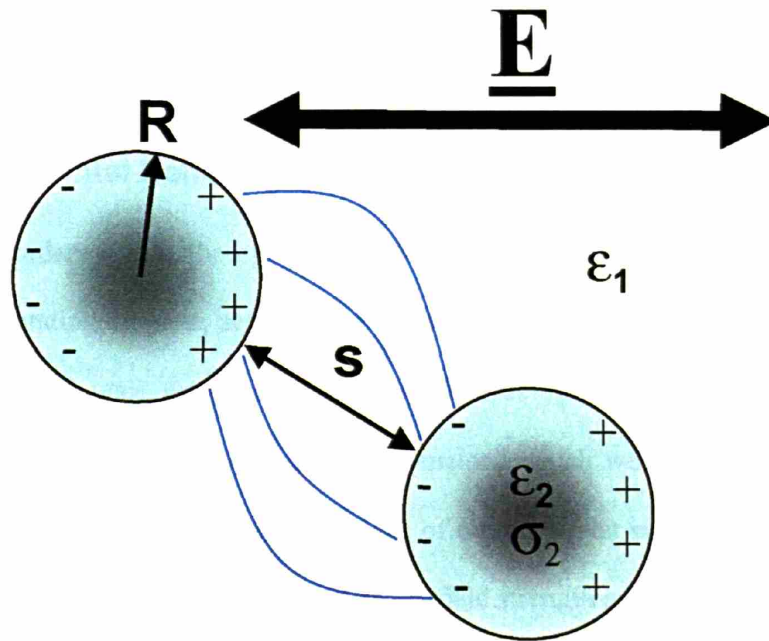
Figure 3.5 Schematic showing two conducting droplets suspended in a non-conducting dielectric medium with an applied electric field. The electrical forces acting on these droplets are given in Equation (3.1).

$$F_{E,ij}{}^{r} = 4\pi\varepsilon a_j{}^2 E_o{}^2 \left(F_1 \cos^2 \psi + F_2 \sin^2 \psi \right)$$
$$F_{E,ij}{}^{\theta} = 4\pi\varepsilon a_j{}^2 E_o{}^2 F_3 \sin 2\psi$$

(3.1)

These equations describe how charges on the sphere surfaces interact depending on their orientation with respect to the applied E-field, with the sign of F_1 always positive, and F_2 and F_3 always negative. Hence, the system is self-aligning barring the presence of other forces, though the magnitude of each is only relevant at short length scales.

Zhang, et al. [56] used this model to numerically simulate population dynamics of a dilute suspension of conductive (aqueous) spheres in a surrounding medium subjected to gravity sedimentation. A strong correlation between the applied field strength and the coalescence rate (change in average droplet size with time) was seen for the water/2-ethyl-1-hexanol system, which studied E-field strengths from 0-100 kV/m and an initial droplet size of 3 μm.

3.4.3 Experimental Behavior of Disperse Flow Subjected to E-fields

In accordance with theory, we observed that large droplets interacted strongly with the surrounding droplets, accounting for the majority of the coalescence events. The initial coalescence rates were fast when droplet spacing was small, but these rates reduced quickly when mostly large droplets remained which were orthogonal to the E-field and far apart. The non-linear dependence of outlet droplet size on voltage suggests that the model predictions [56, 61] correlating E-field strength and interparticle forces are correct at low V, but channel size limits the droplet size at high V (see Figure 3.6).

Flow rates were increased as high as 0.4 ml/min at 11 V, but surprisingly flow rate did not appear to significantly decrease the outlet droplet size. The optimal voltage

frequency for this system was ~10 kHz. We observed electrolysis of the aqueous droplets occurred at frequencies below ~1 kHz and less coalescence at frequencies greater than ~100 kHz. Examination of the complex dielectric constant reveals the source of this behavior:

$$\varepsilon_i = \varepsilon_{i,o} - \frac{\sigma_i}{\omega} j \qquad (3.2)$$

where ε_i is the complex dielectric constant, $\varepsilon_{i,o}$ is the simple dielectric constant, and the imaginary portion is the ratio of the conductivity σ_i and the field frequency ω. Aqueous salt solutions behave as conductors at low frequency and dielectrics at high frequency. We speculate that dielectrophoresis effects or electrowetting on the insulated electrodes might inhibit droplet alignment and subsequent coalescence at high frequencies [62], while at low frequencies electrolysis causes gas bubbles to form instead of coalescing the aqueous droplets.

3.5 Surfactant-Aided Extraction

Additives such as surfactants can affect the distribution of a chemical species between organic and aqueous phases. Here we model the system using an equilibrium model [63]. A completely hydrophobic surfactant (low Hydrophile-Lipophile Balance) is assumed and the concentration is above the critical micelle concentration.
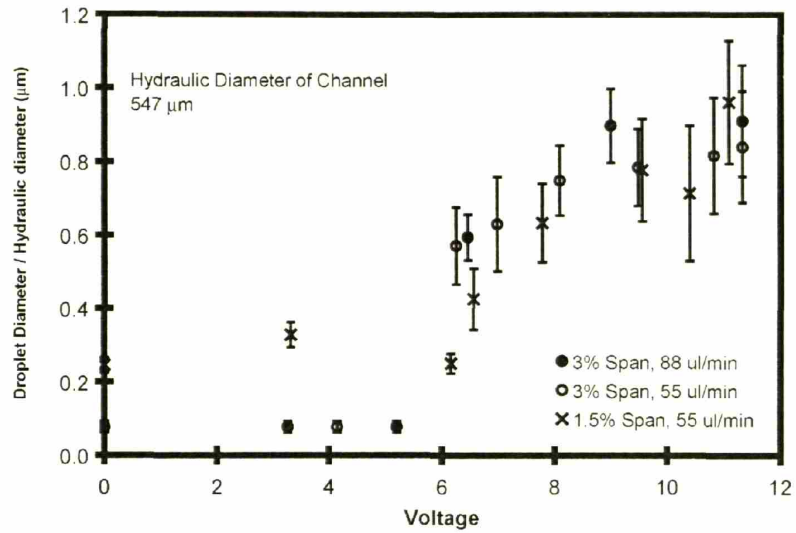
Figure 3.6 The outlet droplet diameter shows non-linear behavior as a function of voltage. A transition is observed around 6 V, above which coalescence is clearly observed.
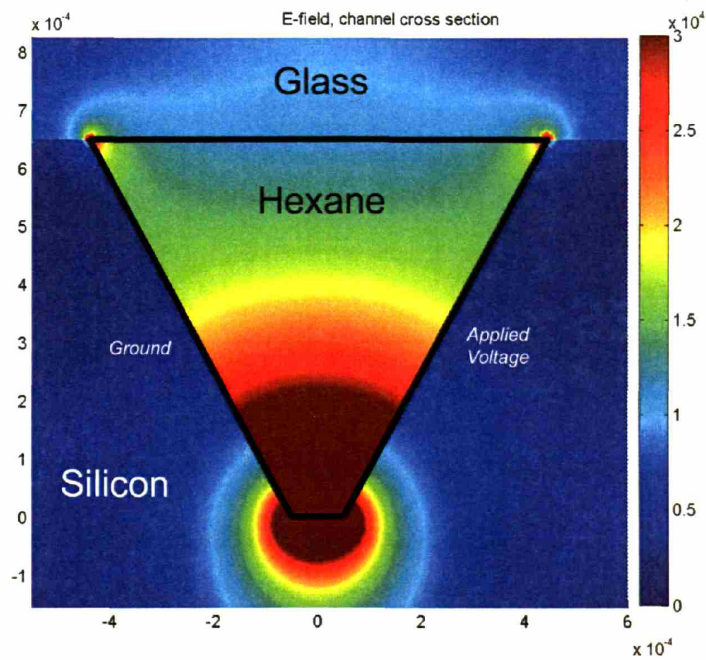
Figure 3.7 FEM of the electric field through a cross-section of the channel (black lines denote channel boundaries). Note that the E-fields are strongest near the bottom (~100 kV/m), which is where the aqueous droplets settle.

Here C_{aq} and C_{org} represent the concentration of extractant in aqueous and organic phases, respectively. S is the concentration of surfactant, which is directly proportional to the micelle concentration if we assume uniform micelle size. M is the concentration of micelle-extractant complexes.

$$\frac{C_{org}}{C_{aq}} = K_1 \tag{3.3}$$

$$\frac{M}{C_{org}S} = K_2 \tag{3.4}$$

The initial and equilibrium concentrations in the system are related by a materials balance:

$$C_{init} = \frac{V_{org}}{V_{aq}}\left(C_{org} + K_2 C_{org}S\right) + \frac{C_{org}}{K_1} \tag{3.5}$$

Solving for C_{org} we obtain:

$$C_{org} = \frac{C_{init}}{\dfrac{1}{K_1} + \alpha\left(1 + K_2 S\right)} \tag{3.6}$$

where α is the ratio of the volumes of organic and aqueous phases (V_{org}/V_{aq}). The HPLC analysis measures the combined M and C_{org} concentrations.

$$C_{meas} = C_{org} + M = C_{org} + K_2 C_{org} S \tag{3.7}$$

Inserting the above expression, we obtain the following expression, which can be fit to experimental data to determine the unknown equilibrium constants, K_1 and K_2.

59

$$C_{meas} = \frac{C_{init}(K_1 + K_1 K_2 S)}{1 + \alpha(K_1 + K_1 K_2 S)} \qquad (3.8)$$

At the limiting condition, $S=0$, the quantity of extractant measured in the organic phase is a function of K_1 and the liquid volume ratio α. For large concentrations of S, all of the extractant can theoretically be extracted into the organic phase with a concentration scaled by α. For large values of K_1 (i.e. when the extractant readily partitions into the organic phase), the effectiveness of the surfactant is reduced. On the other hand when K_1 is small, enhancement of the extraction by the presence of reverse micelles can be significant.

Since hexane is a relatively poor solvent for the phenol and p-nitrophenol compounds compared to water, there is little effect from varying pH on the partition coefficient. However, surfactants improve the extraction efficiency, especially for p-nitrophenol (Figure 3.8). Fadnavis *et al.* show similar results with the extraction of oxytetracycline using Aerosol OT and isooctanol [57]. By fitting the parameters for K_1 and K_2 (see Table 3.1) we can estimate the pure-component distribution of the compounds (K_1) and the affinity of the extractant for the surfactant ($K_1 K_2$). Thus, we can evaluate and select surfactants with the highest $K_1 K_2$ values to improve extraction efficiency.
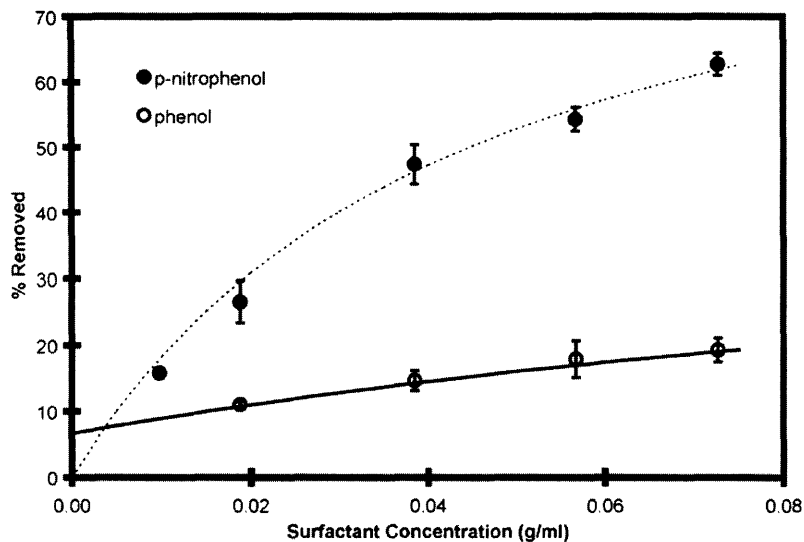
Figure 3.8 The fraction of the organic compounds removed from the aqueous phase varies with the surfactant concentration. The model is shown as the curves as fit to the data.

Table 3.1 Fitted Extraction Model Parameters (seen in Figure 3.8)

Parameter	Phenol	p-Nitrophenol
K_1	0.079	$2.37 \cdot 10^{-6}$
K_1K_2 (mL/g)	3.34	11.16

3.6 Conclusion

We have demonstrated a microfluidic device for electro-coalescence of droplets as part of an emulsion-based scheme for extraction in microfluidic systems. Emulsions have large interfacial areas for mass transfer, but they are often difficult to break once formed. In the current scheme, an emulsion is created in a micro mixer and then broken by electrocoalescence of the droplets into easily separated segments of immiscible liquids. The electrocoalescence device is capable of increasing droplet sizes to the width

61

of the channel, which in our experiments corresponds to a ~1000-fold decrease in droplet number density. In the next chapter, the issues surrounding phase separation in a microchannel will be addressed. The extraction technique could ultimately be combined with microreactors as part of a multistep synthesis scheme.

Chapter 4. Integrated Liquid-liquid Extraction and Phase Separation by Capillary Forces

4.1 Introduction

Development of continuous microfluidic chemical separators is needed for multistep microchemical processing. Common separation processes, such as liquid-liquid extraction, are complicated in a microdevice by the fact that mixing, contacting, and phase separation must be implemented continuously. At this scale, gravitational forces are small compared with surface forces, so it is difficult or impossible to achieve complete phase separation using differences in density. For example, it is not possible to create a microscale version of a traditional two-component distillation where the liquid phase settles and the gas phase rises. Also, the relative strength of the surface forces compared with other forces (e.g. momentum) can make it difficult to form high surface-to-volume ratios for mass transfer in immiscible phase contacting. Alternating slugs tend to form at low velocities instead of thin films or disperse droplets that better facilitate mass transfer [64].

Differences between existing microfluidic extraction devices are seen mainly in mass transport by the way immiscible fluids are contacted. Side-by-side immiscible fluids in co-current and counter-current flow arrangement offer the advantage of phase

separation by laminar flow splitting, but often have relatively poor surface-to-volume ratios and/or low throughput [21, 23-25, 65-68]. The critical issue is maintaining phase separation in these systems, which is usually achieved using small interfacial areas to maintain capillary pressure or surface treatment. In particular, surface modifications (e.g. hydrophobic silanes) tend to degrade with time either through limited solubility in the solvent or susceptibility to chemical attack. For reliable liquid-liquid separation, surface modifications must either not be necessary (ideally), renewed each time (expensive), or made permanent (a difficult task) for the system of interest.

The second method uses slug or dispersed flow for convective mass-transfer between the phases. Convection improves mass-transfer and enables high overall throughput relative to laminar co-current flow, but suffers in that phase separation must be addressed [20-22, 52, 53, 69-75]. Surface- and interfacial forces have been shown to drive microfluidic phase separation of gas-liquid systems [76-78]. However, the interfacial forces (i.e. capillary pressure) in liquid-liquid systems are often low due to small interfacial tensions and contact angles of the liquid-liquid-solid interface approaching 90°.

In addition, there is interest in the integration of individual process steps onto a single device for lab-on-a-chip applications. An integrated design decreases the number of device-device fluid connections that can leak or add dead volume to a process, but it typically takes longer to fabricate and has a lower manufacturing yield than single-function devices. For example, chemical separations benefit from integration of mixing, contacting, and phase separating because the same steps are used for most chemical extraction processes. Mass transfer rates are similar across a variety of chemical species

and chemical compatibility can be ensured by using glass or silicon as the material of construction. However, further integration with reaction units is less desirable than a modular approach that enables tailoring reaction and separation processes to each specific application.

We realized effective liquid-liquid phase separation by using a thin porous fluoropolymer membrane that selectively wets non-aqueous solvents, has average pore sizes in the 0.1-1 µm range, and has a high pore density giving high throughput. Pressure drops throughout the microfluidic network were modeled using laminar flow behavior, and operating regimes for the membrane phase separator were determined based on hydrodynamic pressure drop and capillary pressure forces. A microdevice with a PTFE membrane sandwiched between microchannels was used to verify the capillary pressure-induced phase separation behavior in a hexane/isopropanol/water system.

We investigated the behavior of a microfluidic device designed for solvent extraction that integrates mixing, extraction, and phase separation processes. Mixing and mass transfer were modeled in this system to establish the operating limits, and phase separation was predicted based on the performance of the sandwiched-membrane device. The integrated devices were constructed using silicon micromachining, and model chemical systems were used for phase separation only, solvent extraction, and solvent switching. We found that the device was capable of completely separating several organic-aqueous and fluorous-aqueous liquid-liquid systems, even with high fractions of partially miscible compounds. In each case, extraction was equivalent to one equilibrium extraction stage. This process was then used to perform a solvent switch of the antibiotic erythromycin ethylsuccinate from N,N-dimethylformamide to dichloromethane. Though

only a single stage extraction was demonstrated here, multistage extraction could be realized using multiple devices in series.

4.2 Experimental

4.2.1.1 Device Fabrication

We fabricated two devices in this study, one to explore the phase separation principle (Figure 4.1), and the other to examine the phase separation combined with mixing and extraction (Figure 4.4). First, we fabricated a device which compressed a membrane between two microchannels machined in polycarbonate. After this proof-of-concept, a silicon device was fabricated to mix, contact, and separate the phases which incorporated the membrane by compression sealing with a microfluidic chuck.
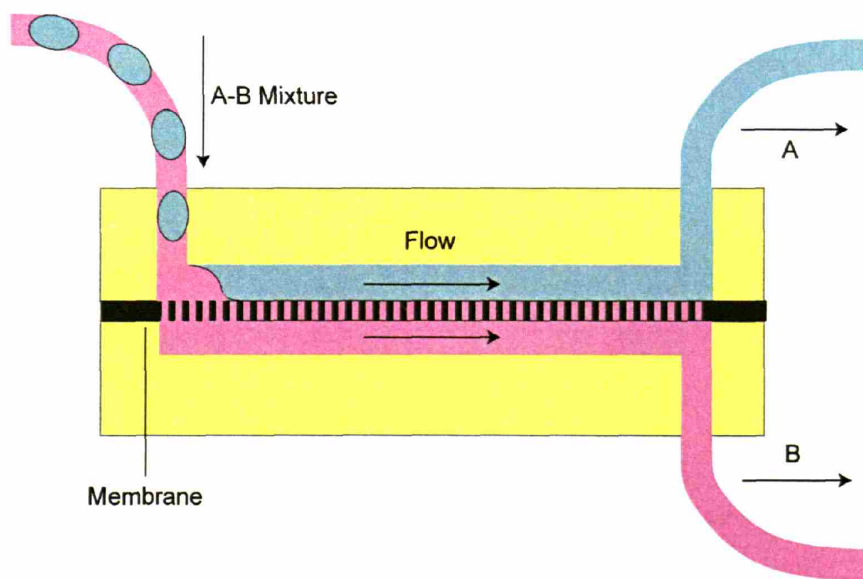
Figure 4.1 A schematic of the phase separation using capillary forces. Phase A passes over the membrane while B passes through and out a separate outlet.

66

4.2.1.2 Polycarbonate Compressed Membrane Device

Standard machining techniques were employed to fabricate 0.5 x 0.5 x 20 mm channels in two pieces of polycarbonate (see Figure 4.2). Inlets and outlets were 0.5 mm holes drilled directly into the channels, and ¼"-28 screws with 1/16" Tefzel tubing (Upchurch Scientific; Oak Harbor, WA) were used for fluid connections. A piece of Zefluor membrane (~7x30 mm from 47-mm disk and separated from the support, Pall Company; East Hills, NY) was placed between the two pieces to divide the channels, and compressed using 10 1/16" hex-nut screws.
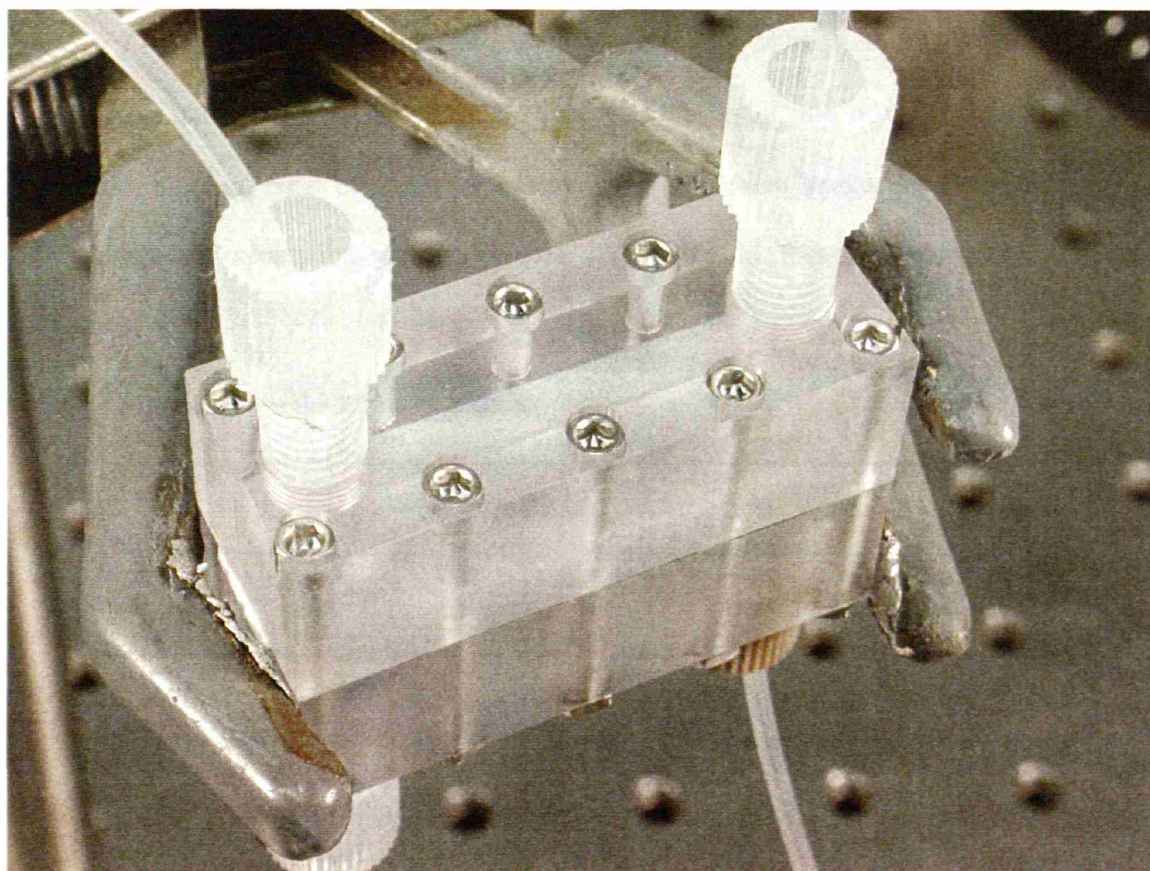
Figure 4.2 The polycarbonate compressed membrane separator is shown with fluidic connections. The device is 10 x 50 x 20 mm in size.

Flowrates of organic and aqueous solutions were varied between 10 and 2000 μl/min. Hamilton Gastight Syringes (Reno, NV) of 1, 5, and 10 mL volumes were used, and PTFE tubing was connected using luer fittings (Upchurch Scientific). Hexane (VWR Scientific; West Chester, PA), isopropanol (VWR Scientific), and DI water (from a Milli-Q water system, 18.2 MΩ; Billerica, MA) were delivered by syringe pump (Harvard Apparatus; Holliston, Massachusetts), mixed and contacted using T-mixers (Upchurch Scientific), and fed to the phase separator.

4.2.1.3 Integrated Silicon Device

The microfluidic separator needed to be capable of handling more than 10 μl/min total flow, and preferably 100 μl/min or more. As a result, the mixer, contactor, and separator must all meet this goal. A schematic of the device layout shows the mixing, contacting, and separation sections (Figure 4.3). Table 4.1 lists the dimensions of the channel.

Table 4.1 Dimensions in the Silicon Microdevice

	Length (mm)	Height (μm)	Cross-sectional Area (μm²)	Volume (μL)	d_h (μm)
Mixer	340	71	3531	1.2	52
Contactor	400	156	29574	11.8	158
Separator	21	648	684047	14.0	663

Silicon microdevice processing consisted of micromachining a silicon wafer using MEMS bulk fabrication techniques (see Figure 4.4).
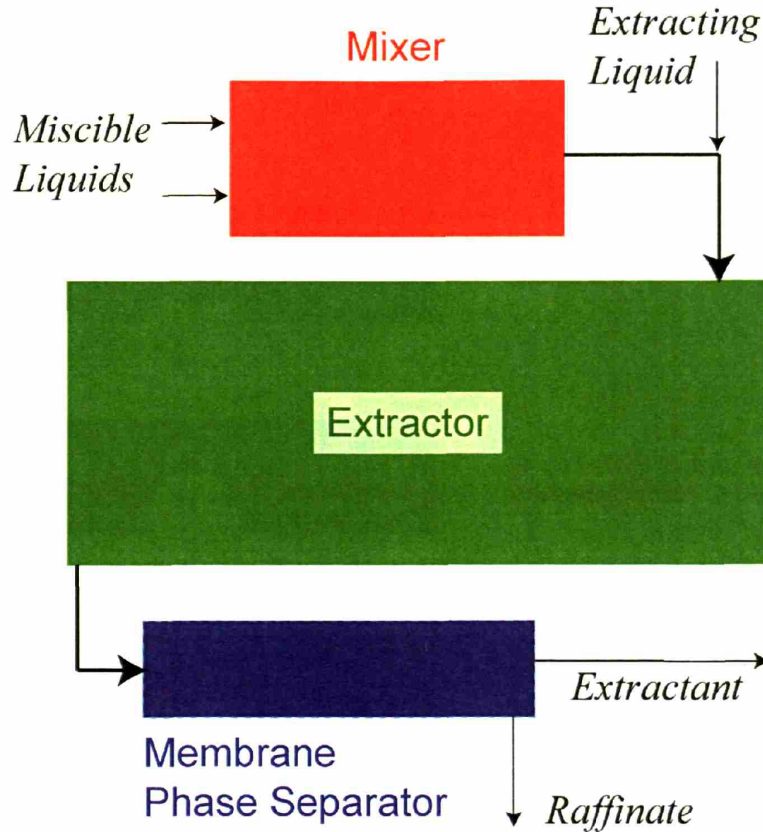
Figure 4.3 Schematic of the integrated extraction device. There are 3 inlets, two for miscible species that feed to the mixer (red), and one for immiscible phase contacting. The extraction occurs in the central section (green), and phase separation is achieved by the membrane phase separator (blue) where there are outlets for the organic (raffinate) and aqueous (extractant) fluids.

Beginning with a 650-700 μm thick (100) double-side polished silicon wafer (SiliconQuest; Santa Clara, CA) coated with 500 nm low-stress nitride, the backside was spincoated with positive photoresist, patterned, and developed to define the fluid ports and membrane trench. SF_6/O_2 plasma was used to etch the nitride layer, exposing the underlying silicon. Next, the wafer was etched in 25 wt% KOH at 85°C to a depth of 320-340 μm, depending on the wafer thickness.

69

Silicon Wafer with 500 nm
Low Stress Silicon Nitride

Silicon Nitride Layer Patterned
and Etched

25 wt% KOH Etch to Define
Backside Features

Repeat process for Frontside
Features

Etch Nitride Film with
49% HF

Anodically Bond Pyrex Glass
Wafer to Cap Flow Channels
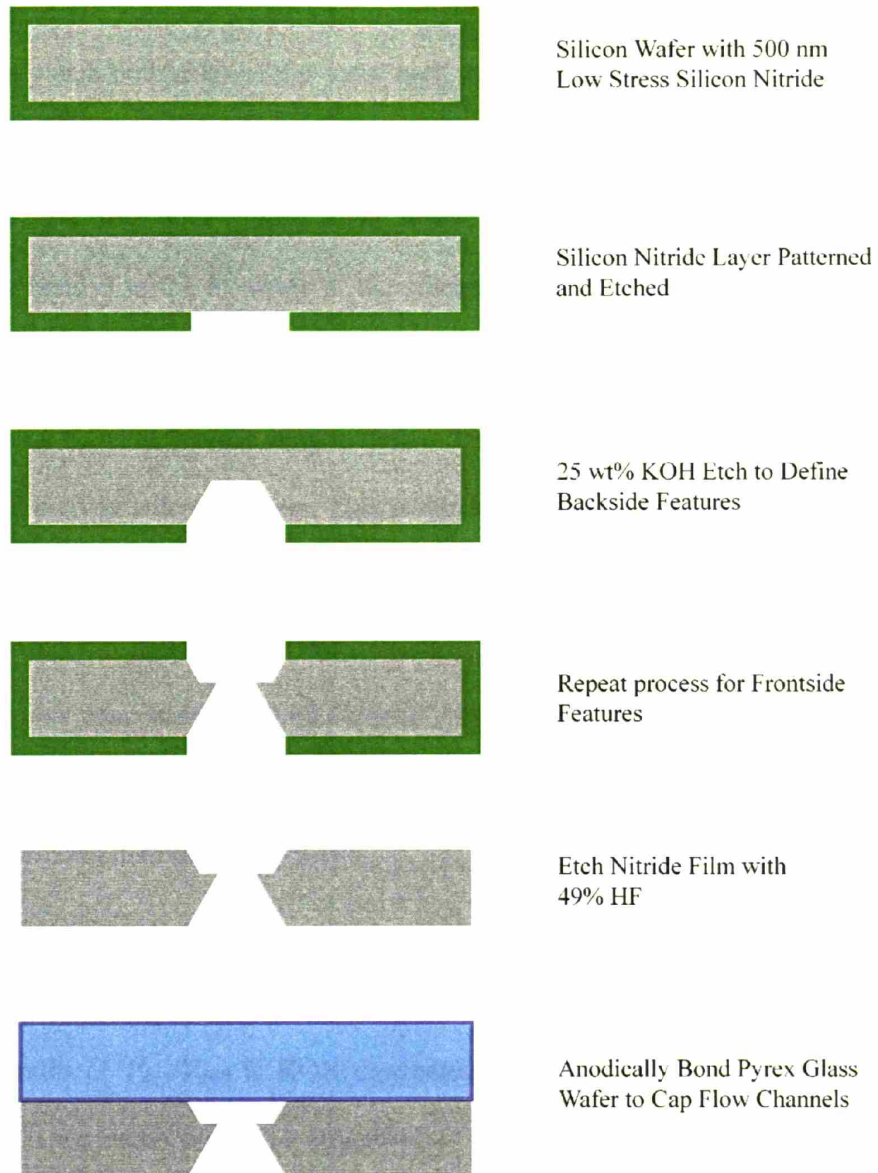
Figure 4.4 Silicon microfabrication process

The wafer was cleaned with a piranha bath (3:1 concentrated sulfuric acid: 30% hydrogen peroxide), and the frontside was aligned to backside features and patterned using positive photoresist to define the main flow channels for the mixer, contactor, and membrane trench. The frontiside silicon nitride layer was patterned and etched the same way as the backside, and again the wafer was subjected to a hot 25 wt% KOH solution to

70

concurrently etch both sides of the wafer until the inlets meet the flow channel, ~190 μm on both sides. The wafer was cleaned and 49% HF was used to etch the remaining nitride. Finally, a 762 μm thick Pyrex 7740 wafer (Bullen Ultrasonics; Eaton, OH) was anodically bonded to the frontside of the silicon device and individual devices were cut using a diesaw (Figure 4.5).

Using KOH etch processing to define flow channels can result in the over-etching of exposed convex silicon corners. This is due to the significantly faster etch rate of the <411> crystal plane compared to the <100> (~1.5x). Small "tabs" can be used at these exposed corners to significantly reduce the amount of overetching [79]. To minimize film stress that may concentrate at these exposed corners, we selected low-stress nitride as the KOH mask layer. However, we did not compare devices produced by the different nitride films (i.e. stoichiometric vs. low-stress).

$$\frac{V_{411}}{V_{100}} D_e = 0.857\left(0.424B - 0.4w_2 + 0.4w_3\right) \tag{4.1}$$

The etch ratio of V_{411}/V_{100} is KOH concentration dependent [80], D_e is the depth of etching, B is the width of the tab structure, w_2 is the resolution limit of lithography, and w_3 is the desired width of the channel (Figure 4.6). The maximum depth the corner compensation structure can protect is given by the following inequality:

$$D_e \leq \frac{\left(w_3 - w_2\right)}{0.398 + 0.730\dfrac{V_{411}}{V_{100}}} \tag{4.2}$$

As a rule of thumb, the maximum etch depth is ~ 0.6-0.7 the channel width (w_3).

Fluids were delivered using Harvard Apparatus syringe pumps at flowrates ranging from 1-60 µL/min, depending on the syringe and chemical species. DI water (Milli-Q) and N,N-dimethylformamide (Sigma-Aldrich; Milwaukee, WI) were loaded into plastic syringes (B&D Scientific; Franklin Lakes, NJ), and the organic solvents dichloromethane (DCM) and diethyl ether (Sigma-Aldrich) were loaded into a removable needle Hamliton Gastight syringe. For solvent switch experiments, erythromycin ethylsuccinate (MP Biomedicals, Inc.; Eschwege, Germany) was dissolved in DMF and switched to DCM.
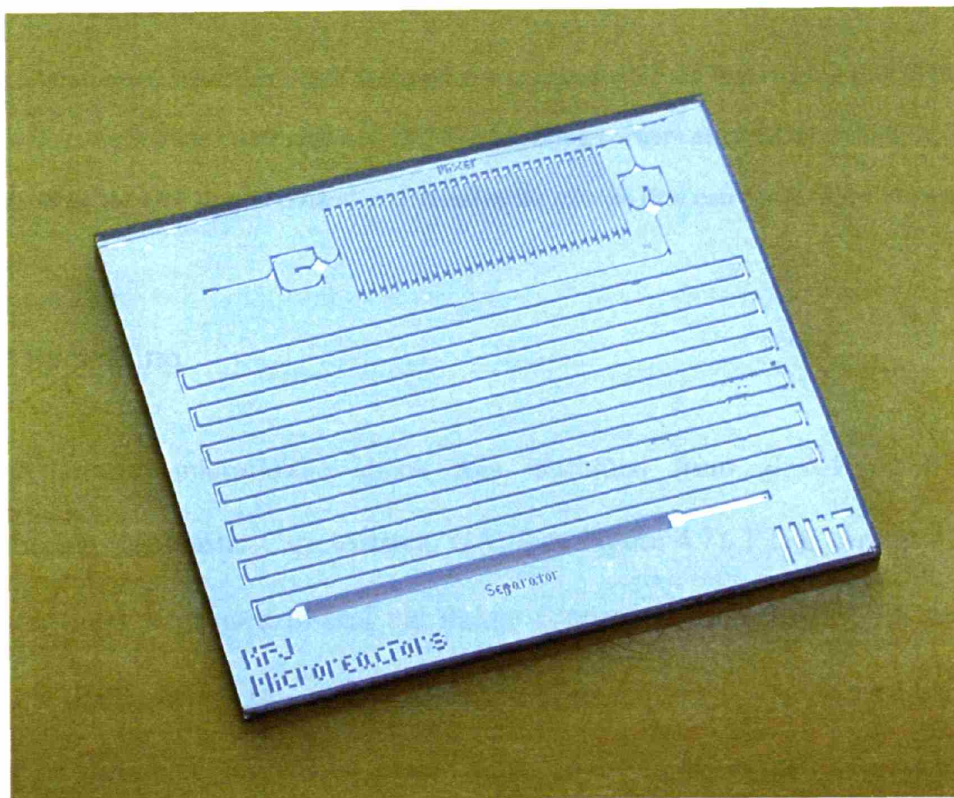
Figure 4.5 Integrated extractor with mixer (top), contactor (middle), and separation trench (bottom). The device is 35 x 30 x 1.4 mm in size.
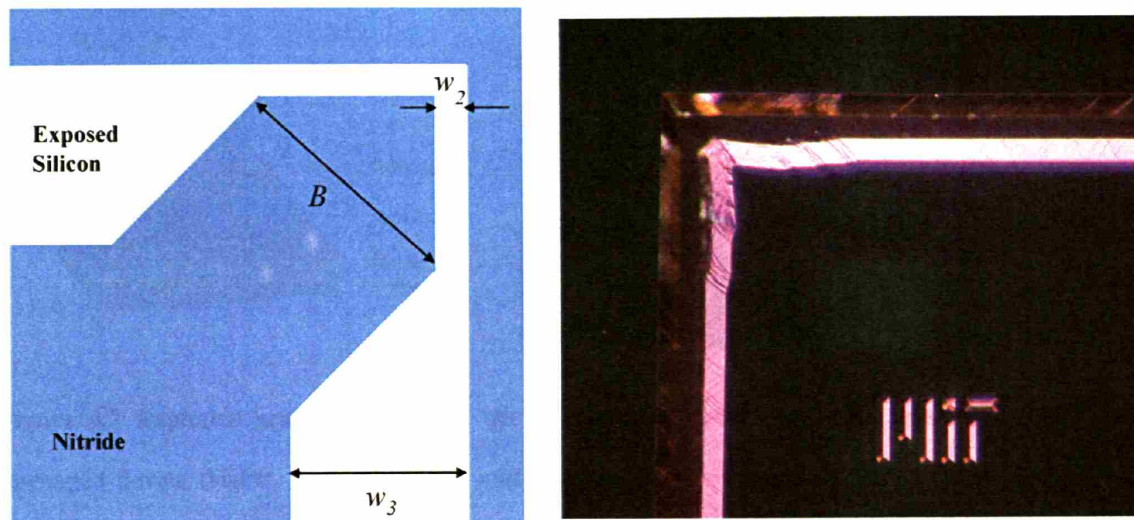
Figure 4.6 Photomask structures (left) designed to compensate for the fast etching rate of the exposed convex corners during the KOH etch process. The resulting corners after KOH etching (right) reveal that controlling the etch time is critical and stress in the nitride film can cause slight imperfections in the corners.

4.2.1.4 Packaging

A custom microfluidic chuck was machined from glass-filled PTFE and polycarbonate (McMaster-Carr; Atlanta, GA) (see Figure 4.7). PTFE o-rings (TEF-003, McMaster-Carr) were used to seal the fluidic connections and the 0.5 μm pore PTFE membrane (Pall) was cut to ~ 8x25 mm from a 47-mm disc and compressed between the trenches on the chuck and silicon device. Fluid connections on luer-type syringes were made using luer fittings (Upchurch Scientific), while Valco fill ports (VISF-2; Houston, TX) were used on the Hamilton Gastight syringe. 1/16" OD PTFE tubing with 0.01"-0.02" ID and ¼"-28 screw fittings were used to connect to the fluid chuck.
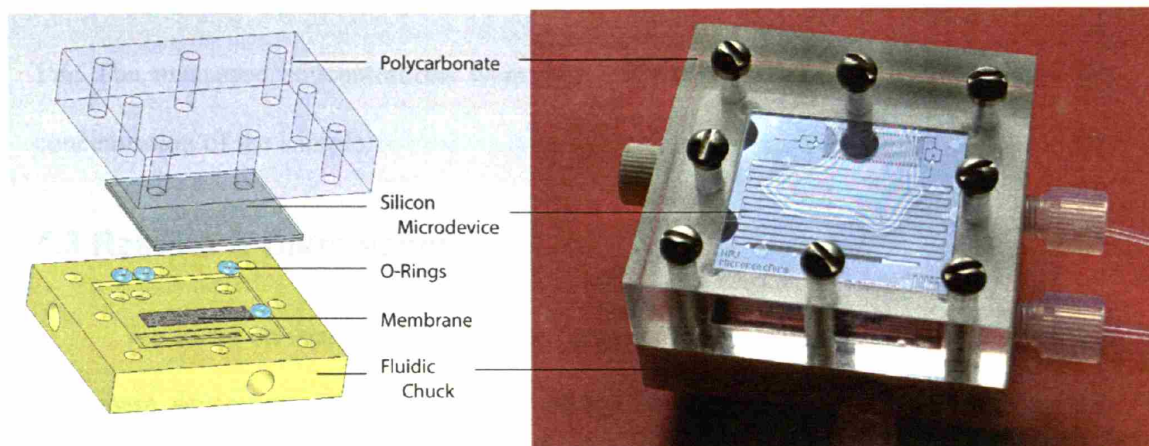
Figure 4.7 Exploded schematic view of the microfluidic device and packaging (left), and final packaged device (right). The membrane and silicon microdevice are sealed by compression using Teflon o-rings with the fluid chuck and polycarbonate top plate.

4.2.1.5 Analytical

For phase separation-only experiments, visual inspection of the outlet fractions was used to confirm no immiscible phase passed to the wrong outlet. The use of red and blue dyed aqueous pH 4 and 10 buffers (VWR Scientific) made this straightforward. Videos were also obtained for qualitative analysis at some flowrates using a COHU 2222-1000 color CCD camera (COHU; Poway, CA) and a Leica stereo-microscope MZ12 (Leica Microsystems Inc.; Bannockburn, IL).

For extraction analyses, we used HPLC (Waters; Milford, MA) with a reverse phase C-18 column and 0.1 M aqueous monobasic phosphate buffer at 1 mL/min for the aqueous extract. A calibration curve of the concentration vs. absorbance at 220 nm was prepared for known concentrations of extractant (DMF, VWR Scientific) in de-ionized water to quantify results. 25-100 µl of each sample was diluted in 900 µl of water and run 3 times. Variation in area counts between runs was less than 3% and typically less than

74

1%. The measured concentrations were then scaled by the dilution factor to give the concentration of the sample.

4.3 Results & Discussion

We focus on issues arising from solvent extraction, namely mass transfer effects and phase separation. The development of the liquid-liquid capillary phase separator capable of functioning with low interfacial tensions and no surface treatments is critical to achieving continuous flow processing in microchemical systems. To first test the limitations of the membrane phase separation principle, we perform flow experiments in a machined polycarbonate device with only the porous fluoropolymer membrane between two channels. Next, a silicon device incorporating the fluoropolymer membrane is used for solvent extraction to study integration of fluid mixing, contacting, and separating the phases.

4.3.1 Liquid-Liquid Phase Separation Using Capillary Forces

4.3.1.1 Theoretical Analysis

The immiscible liquids are delivered to the membrane separator by pressure driven flow where selective wetting and capillary pressure are used to induce and maintain separation of the two phases. During separation, the capillary pressure difference prevents the non-wetting phase from penetrating the porous membrane surface. In all cases, this pressure difference must be greater than the pressure drop used to drive the fluid flow:

$$\Delta P_c > \Delta P_{flow} \tag{4.3}$$

The aqueous phase, which wets the PTFE membrane poorly, passes across the membrane surface while the organic/fluorous phase wets and flows through the pores of the membrane (see Figure 4.1).

The Young-Laplace equation was used to model the interfacial pressure at the membrane surface using cylinders to represent the membrane pores:

$$\Delta P_c = \frac{2\gamma}{R}\cos\theta \qquad (4.4)$$

where γ is the interfacial tension, R the pore size, and θ the wetting angle. Typical pore sizes in the membrane were ~ 0.5 μm. To prevent the non-wetting phase from penetrating the capillaries, the capillary pressure must be greater than the pressure drop due to the outlet tubing. For γ=10 mN/m and θ=60°, the interfacial pressure $\Delta P_c = 40$ kPa or 0.4 bar.

$$\Delta P_c > \Delta P_1 \qquad (4.5)$$

For the wetting phase, the pressure conditions must be such that no wetting fluid flows though the non-wetting fluid outlet.

$$\Delta P_1 > \Delta P_2 + \Delta P_m$$
$$\Delta P_m = \frac{8\mu Q}{n\pi R^4} L \qquad (4.6)$$

The pressure drop through the membrane, as defined by the Hagen-Poiseuille equation, is ΔP_m, μ is the fluid viscosity, L is the capillary length, and n is the number of capillaries through which fluid is flowing. The membrane also has a high pore density ($\sim 10^8$

76

pores/cm^2), reducing hydrodynamic resistance of the wetting phase by distributing the flow (Figure 4.8).

Using Equations (4.5) and (4.6), we can formulate the pressure drop requirements in a capillary separator system.

$$\Delta P_c > \Delta P_1 > \Delta P_2 + \Delta P_m$$

$$\frac{2\gamma}{R}\cos\theta > \frac{8\mu Q}{\pi R_1^4}L_1 > \frac{8\mu Q}{\pi}\left(\frac{L_c}{nR^4} + \frac{L_2}{R_2^4}\right) \qquad (4.7)$$

From this equation it is clear that pore size and pore length must be small, while the number of pores must be large. Thus, a porous membrane film is the optimal solution for this application.
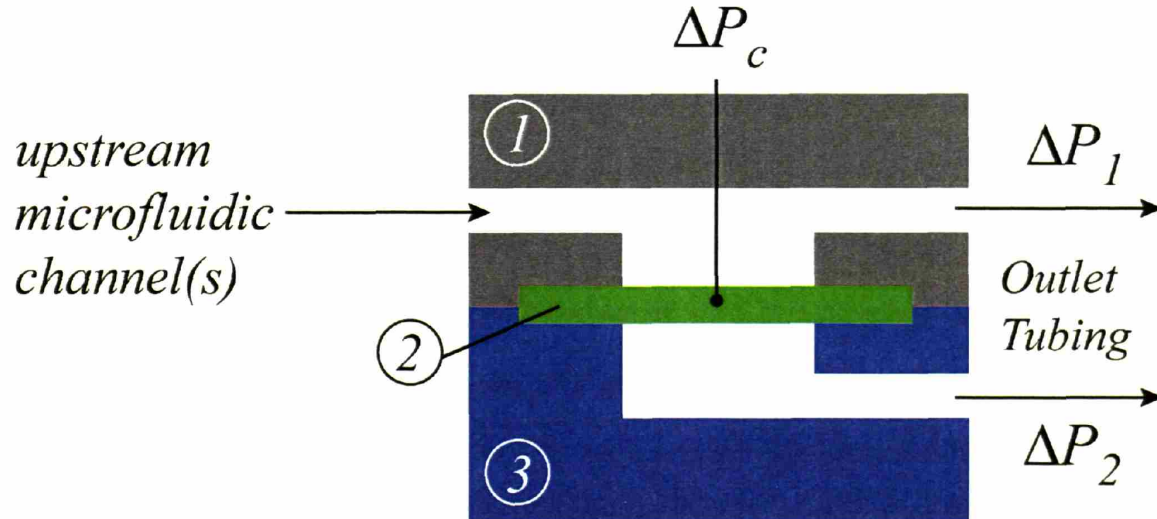
Figure 4.8 A schematic of the device construction with the silicon device (1), the porous Teflon membrane (2) and the machined fluidic chuck (3) in compression. The membrane is placed between two fluid channels and the pressure drops of the outlet streams controlled to ensure complete phase separation

4.3.1.2 Phase Separation Experimental Results

For each immiscible liquid-liquid system studied, we observed the organic or fluorous phase pass through the membrane while the aqueous phase was repelled by the membrane and passed out a second outlet in the polycarbonate-machined microdevices. Capillary forces were responsible for this separation, which was confirmed by drawing a less-dense organic phase against gravity through the bottom outlet port (see Figure 4.8). Aqueous-fluorous extraction and phase separation could be of interest for biological [81] and organic molecule synthesis studies, as fluorously-labeled compounds have a high affinity for the fluorous phase [82].

The effect of lowering the interfacial tension on separation capacity was tested on the polycarbonate device by adding isopropanol to hexane using a t-mixer (Upchurch). The maximum operating flowrate decreased significantly with increasing IPA vol%, though the polycarbonate device was still capable of separating > 100 μl/min of total fluid flow at 17 vol% IPA (see Figure 4.10) and 25 cm of 0.254 mm OD PTFE tubing on the aqueous outlet. At some concentration of IPA, the surface tension will decrease to a value at which point the inequality (4.7) is no longer valid, though we did not probe such high concentrations. The maximum mol fraction of IPA while retaining 2-phase behavior is ~42%, though significant amounts of the other two solvents become entrained in one another, resulting in poor extraction purity and yield [83].
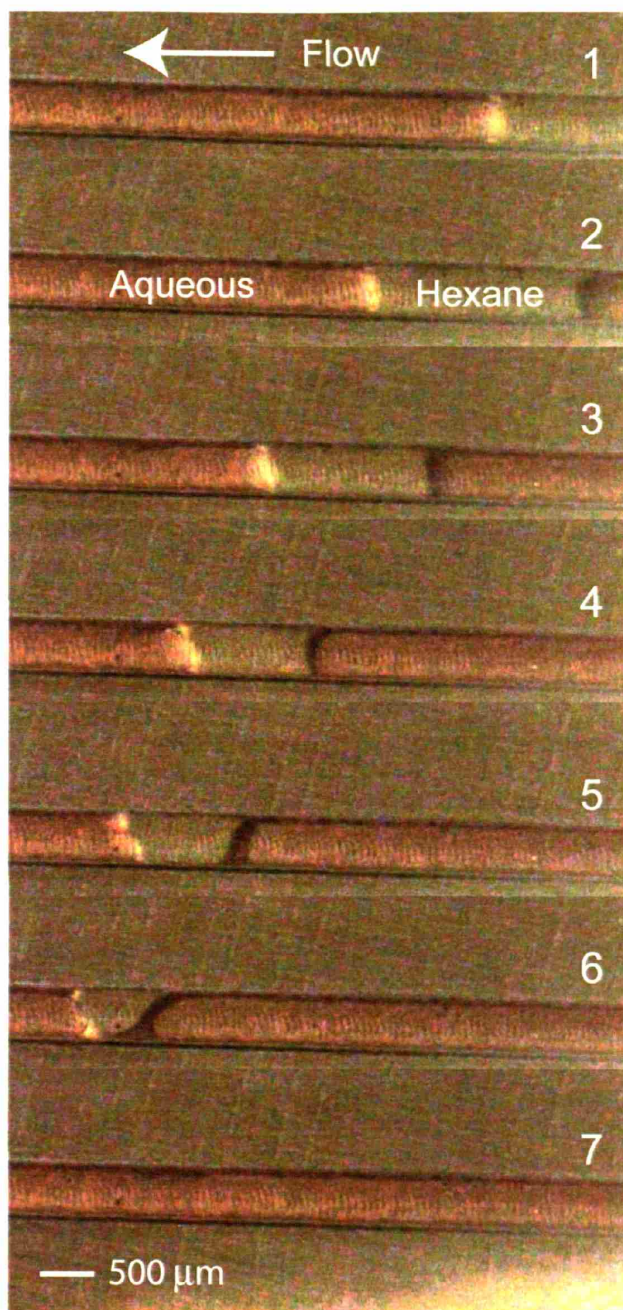
Figure 4.9 Sequential images (1-7) taken looking down onto fluids flowing atop the membrane. The images were captured from video of co-flowing immiscible aqueous (red) and hexane (clear) phases passing over the PTFE membrane. The hexane passes through the membrane and "disappears" from view. The total flowrate was 100 µl/min.
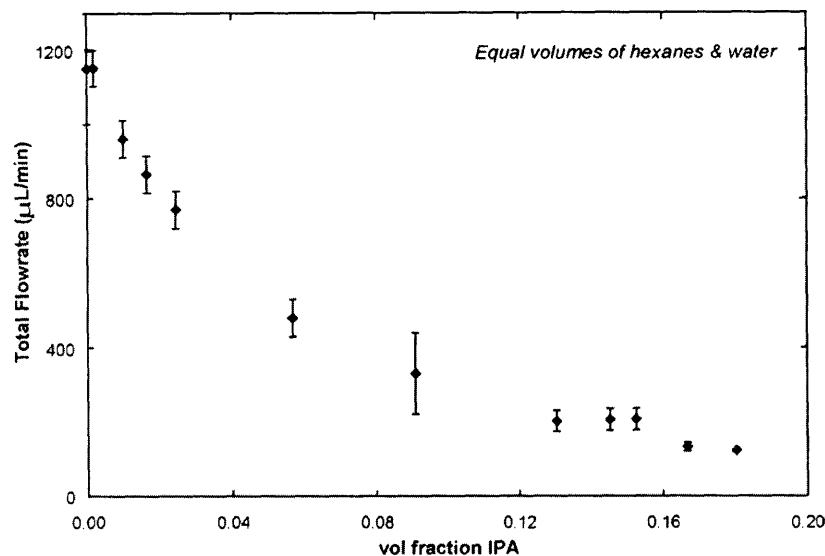
Figure 4.10 The effect of lowering the interfacial tension on phase separation performance was studied by adding IPA to a flow of hexane/water. The maximum operating flowrate decreased significantly with increasing IPA concentration, but phase separation was maintained at total flowrates less than 120 µL/min in all cases.

A sufficient difference in the surface wetting by the two immiscible phases is required for the device to function properly. For example, no suitable material was found to separate organic (hexane) and fluorous (perfluorohexane, Lancaster Synthesis, Inc.; Pelham, NH) phases. The materials studied included PTFE (Pall), cellulose (filter paper, VWR), and ethyl acetate (Sigma Aldrich).

4.3.1.3 Integrated Liquid-Liquid Extraction Device

In the integrated extraction device, characteristic times for mixing, contacting, and phase separation were examined to aid in characterizing device performance.

4.3.1.4 Diffusive Mixer

Mixing of miscible component is sometimes necessary in solvent extraction processes. In a solvent switch process, for example, the two miscible solvents must first be mixed to transfer the species of interest before the old solvent can be extracted. Based on previous works on diffusive mixing [84, 85], bifurcation of the flow once decreases the mixing time by a factor of 4. The diffusion path length was estimated as ¼ of the channel width (25 μm). Liquid diffusivities are $\sim 10^{-9}$ m^2/s, giving a mixing time of ~ 0.6 seconds and a maximum operating flowrate of ~ 120 μL/min. The pressure drop through the mixer alone would be ~ 10 bar at this flowrate.

4.3.1.5 Modeling of Mass Transfer with Slug Flow for Extraction

Simple mass transfer descriptions include a Fourier analysis for a stagnant fluid as reported previously [20], and one based on recirculating flow [86]. Although the Fourier analysis is well accepted for modeling stagnant films, the system is not stationary and convective transport is significant compared with diffusion.

The hydraulic radius was used to simplify the analysis. The shape of the channel is trapezoidal with all sides between 100-300 μm, suggesting that the characteristic channel dimensions should be valid for first-order approximations.

$$d_{hyd} = \frac{4A}{P} = \frac{4\left(H/2 \left(w_1 + w_2\right)\right)}{w_1 + w_2 + 2s}$$
$$s = \sqrt{H^2 + 0.25\left(w_1 - w_2\right)^2}$$

(4.8)

The characteristic velocity in the system is defined by the ratio of the flowrate to cross-sectional area. The mass transfer coefficient for the Taylor flow of bubbles in capillaries is given by Kreutzer, et al. [86] using penetration theory. Only the species flux at the end (cap) of the slug is considered to give the most conservative estimate for this design:

$$k_L a' = \frac{8\sqrt{2}}{\pi(L_1 + L_2)} \sqrt{\frac{DU}{d_{hyd}}} \qquad (4.9)$$

Here, the internal recirculation of the slug affects the mass transfer rate because of surface renewal. For our system, characteristic model parameters [87] gave a recirculation mass transfer coefficients ($k_L a$) of 0.26 s^{-1}.

Depending on the particular immiscible fluids used and surface properties of the flow channels, other models may more accurately characterize any experimentally observed mass transfer rates. The case where a thin immiscible fluid separates the wall and bubble is one example. However, from a general design standpoint we cannot assume these other modes of mass transfer will be present and are therefore excluded from the design calculations.

To model the time-dependant concentration behavior in this system it was assumed that interfacial mass transfer resistances for both liquid phases equal, all mass transfer resistances are lumped into the estimates for $k_L a$ and constant, and the chemical partition coefficient is assumed constant. The first assumption can be justified by the fact that diffusion coefficients of small molecules in all liquids are approximately the same; in addition this gives the slowest possible estimate for the time required to reach equilibrium. The second assumption is made to simplify the analysis by using the results

already obtained from more detailed studies, such as Kreutzer, et al [86]. And the last assumption is valid for dilute species partitioning between two phases. Species conservation equations can be written for the organic and aqueous phases.

$$\frac{dC_a}{dt} = k_L a \left(C_{ai} - C_a \right)$$

$$\frac{dC_b}{dt} = -k_L a \left(C_b - C_{bi} \right) \qquad\qquad (4.10\text{-}11)$$

$$K = \frac{C_{bi}}{C_{ai}}$$

The fluxes are matched and the partition coefficient utilized to eliminate the interfacial concentrations.

$$V_a k_L a \left(C_{ai} - C_a \right) = -V_b k_L a \left(K C_{ai} - C_b \right)$$

$$C_{ai} = \frac{\alpha C_a + C_b}{\alpha + K}, \quad \alpha \equiv \frac{V_b}{V_a} \qquad\qquad (4.12)$$

This allows rewriting of the coupled ordinary differential equations in terms of only two variables subjected to the boundary conditions $C_a(0)=0$, $C_b(0)=C_{bo}$ at $t=0$. The resulting coupled ODEs were solved and representative concentrations plotted (see Figure 4.11).

$$\frac{dC_a}{dt} = k_L a \left(\frac{\left(\alpha C_a - C_b \right)}{\alpha + K} - C_a \right)$$

$$\frac{dC_b}{dt} = -k_L a \left(C_b - \frac{K \left(\alpha C_a - C_b \right)}{\alpha + K} \right) \qquad\qquad (4.13\text{-}14)$$

$$C_a = \frac{C_{bo} \left(1 - \alpha K e^{-k_L a \cdot t} \right)}{\alpha + K}, C_b = \frac{C_{bo} \left(K + \alpha e^{-k_L a \cdot t} \right)}{\alpha + K}$$

Equilibrium times $\sim$ 20s were suggested by the model using the characteristic parameters, though $\sim$ 9s will give 90% extraction efficiency. Therefore, the expected

maximum operating flowrate for this system is at least 50 μl/min. These conservative design estimates will ensure that equilibrium is reached in the system at flowrates up to and possibly beyond this value. However, it is not possible to probe significantly higher flowrates due to the pressure drop associated with the mixer and the limitations of the fluid delivery system.
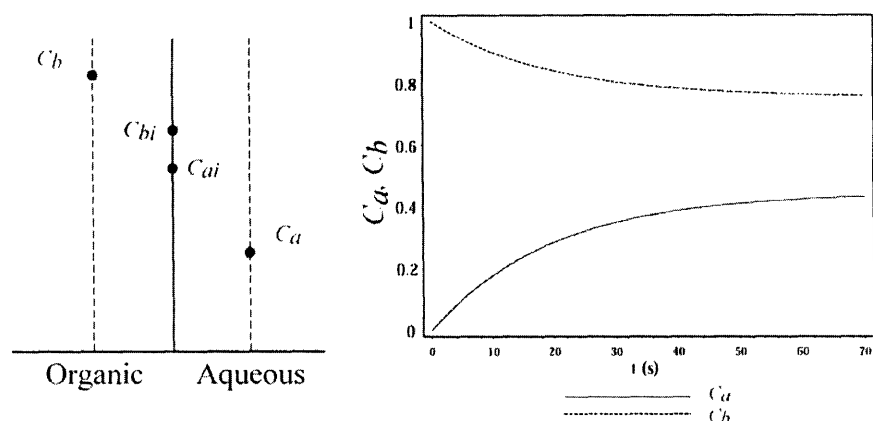
Figure 4.11 Representation of the concentration profiles in the aqueous and organic phases. The concentration profiles (normalized to C_{bo}) in both phases as described by the conservation equations.

4.3.1.6 Solvent Extraction

Large amounts of equilibrium data have been compiled for partially miscible systems and help simplify solvent selection for extraction [88]. However, finding an optimal solvent for a particular system requires some experimental work. As a model system, we chose to extract N,N-dimethylformamide (DMF) from an organic phase into water.

Methylene chloride (DCM) and diethyl ether (DEE) were each used as the non-polar organic solvent and the DMF fraction in the organic stream was varied from 1-20

84

mol%. The partition constant did not change significantly over this concentration range, as indicated by a linear plot of aqueous extract DMF mol fraction vs. the initial organic DMF mol fraction (Figure 4.12). We measured the concentration of DMF in the aqueous extract stream and performed a mass balance to calculate the extraction yield (Figure 4.13).

$$Y = \frac{N_{aq,DMF}}{N_{0,DMF}} = \frac{x_{DMF} N_{aq}}{y_{DMF} N_{org}} \qquad (4.15)$$
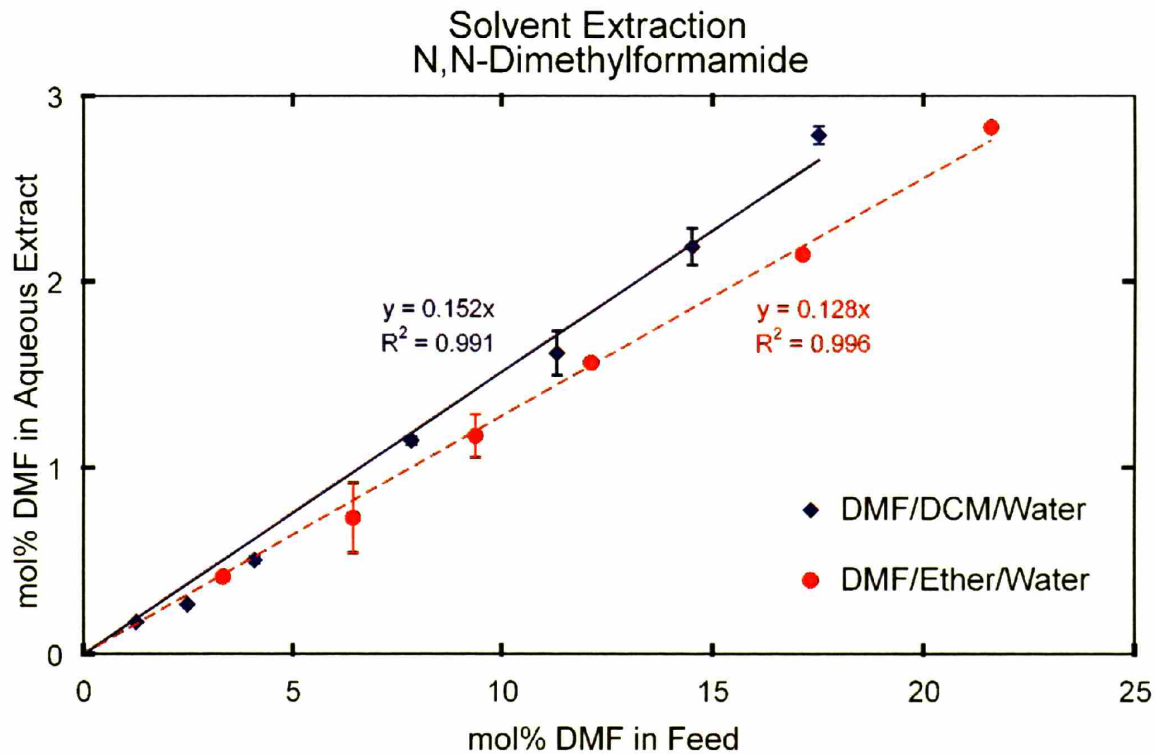
Figure 4.12 The partition coefficients of DMF in the DCM/water and DEE/water systems are nearly constant at low to moderate DMF concentration, as noted by the linear increase in aqueous extract concentration vs. the feed concentration.

For a system with a constant partition coefficient, the extraction yield is constant. The extraction yield values obtained from the microfluidic device agree well with the

equilibrium data obtained from shake-flask experiments for these two cases. The DCM/DMF/water values also agreed well with those reported in the literature [89]. Thus, each device is capable of a single equilibrium extraction stage.

It is known that using multiple extractor units in series gives better extraction of the partially miscible component [18]. The total extraction yield is power-law dependent on the number of stages (n), assuming a constant single-stage extraction yield. A process with a single stage yield of 60% will therefore remove ~94% of the undesired species in 3 stages. Multistage extraction processing and other opportunities in this area are discussed in the final chapter of this thesis.

Solvent Extraction Yield
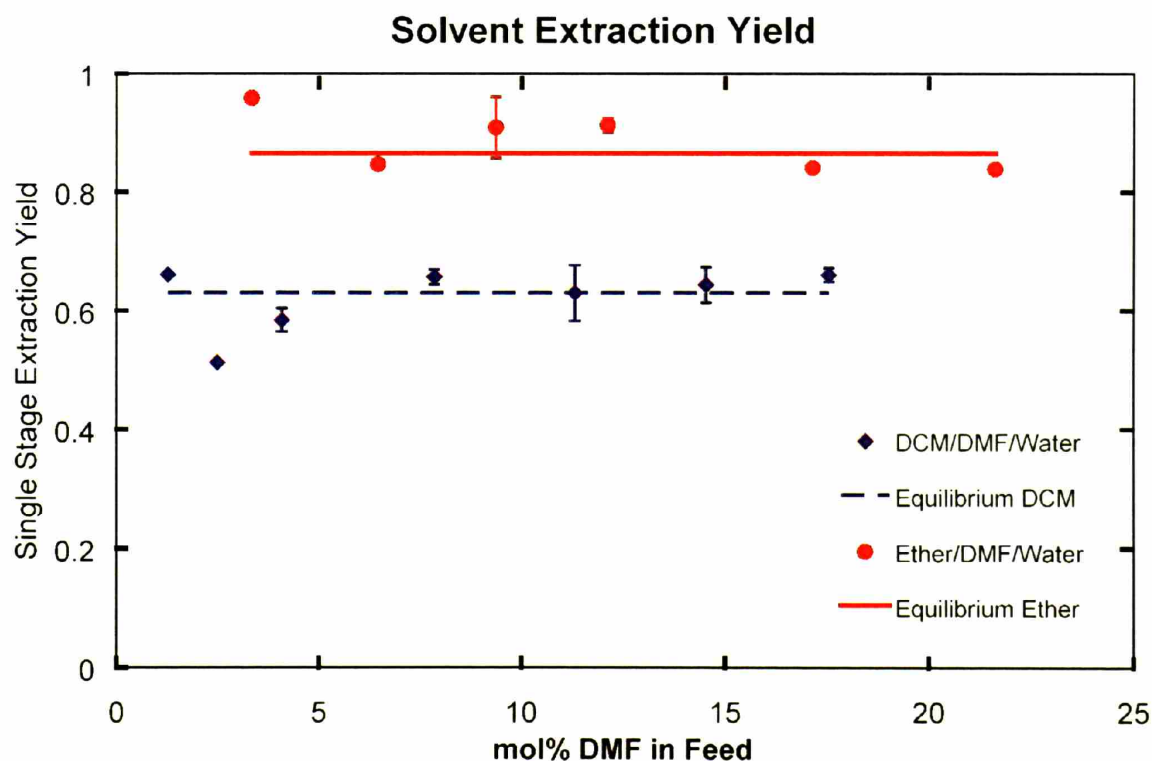
Figure 4.13 Extraction yield vs. DMF organic feed concentration. The solid lines indicate the average yield from shake flask equilibrium extraction experiments.

4.3.1.7 Solvent Switching

To demonstrate the practical application of this device, we extracted erythromycin ethylsuccinate (EES) from DMF into DCM, also known as a solvent switch. Erythromycin is a common antibiotic and a fermentation product of *Streptomyces erythreus*. A derivative of erythromycin, EES is sparingly soluble in water and can be prepared from pure erythromycin by esterification with a carboxylic acid in a polar organic medium with catalytic amounts of strong acid and heat. This modification is necessary for drug delivery because the ethylsuccinate group protects the antibiotic in acidic conditions similar to those found in the stomach, allowing the antibiotic to be delivered orally and in lower doses than had been used previously without significantly affecting the drug's efficacy.

To purify this compound, the polar solvent is removed using a solvent switch, leaving the EES in the non-polar organic phase. DEE and DCM are good candidates for this as they can be easily evaporated, leaving pure crystallized EES. We prepared a 1% EES solution in DMF and mixed with a T-contactor at a flow ratio of 1:10 using pure dichloromethane. This organic stream was then contacted 11:23.7 with water in the device where the DMF was extracted and the phases separated continuously. HPLC analysis of the aqueous stream showed no detectable EES. As further confirmation, droplets of the extract and raffinate were placed on a clean glass slide and allowed to dry. The aqueous extract left no noticeable residue, while the organic phase left a crystallized white powder.

4.4 Conclusions

Surface forces were used to continuous separate immiscible liquids in microfluidic devices. We have analyzed the fluid flow and pressures in microfluidic systems to model the conditions required for phase separation using capillary forces. It was shown that the capillary pressure difference must be much greater than the pressure used to drive the fluid flow through the device, and the pressure drop for the two fluid outlets must be adjusted so that the membrane non-wetting phase experiences a larger pressure drop than the membrane wetting phase. A thin, porous, PTFE membrane was selected for facilitating phase separation because of its small pore size, high pore density, and non-wettability with aqueous solutions. It was also not necessary to modify the surface properties with silanizing agents. A membrane-only device was capable of complete phase separation of aqueous/organic and aqueous/fluorous systems, even with high fractions of partially miscible components significantly lowering the capillary pressure. Separating organic/fluorous systems remains a challenge because both liquids wet a wide range of membrane materials.

Phase separation was implemented with mixing and liquid-liquid contacting to create an integrated microfluidic liquid-liquid extraction unit operation. The device was manufactured using silicon micromachining and packaged with the membrane using compression sealing to a fluidic chuck. In this device, solvent extraction of DMF from DCM and ethyl ether to the aqueous phase was performed and found to be equivalent to one equilibrium stage. An extraction of erythromycin ethylsuccinate from DMF to DCM was then carried out using the same device without any detectable loss of EES to the aqueous phase.

The devices and phenomena studied in this chapter are a step towards addressing the challenges in continuous microchemical separations processing. Looking ahead, multistage extraction could be performed using multiple devices in series. This would allow continuous processing and the same extraction yield as multiple shake-flask extractions performed during traditional chemical workup.

Chapter 5. Kinetic Studies of Sodium Nitrotetrazolate Formation via Multistep Synthesis in Microreactors

5.1 Introduction

The chemical kinetics of reactions involving hazardous and energetic reagents and intermediates have remained poorly understood due to significant challenges involving safety and heat/mass transfer. Microchemical systems now enable such studies with their inherent safety, low reagent consumption [8], and improved heat and mass transfer due to small characteristic length scales [11, 19, 90]. Many common single- and multiphase reactions have been demonstrated in microchemical systems [91]. In addition, running reaction experiments in parallel improves data collection rates [10, 92]. However, despite the ability of these systems to rapidly probe a wide range of reaction conditions, examples of multistep synthesis and optimization of reaction conditions using microchemical systems remain few in the literature.

As a model system, we study the diazotization and substitution of 5-aminotetrazole. The diazonium ion is a semi-stable species commonly used for substitution of a primary aromatic amine with other species (e.g. halides, cyano, nitro) or

90

to couple two aromatic species (e.g. azo dye formation). Diazonium ions should be kept in solution and used immediately because they tend to decompose to phenols in aqueous solution. This reaction usually involves treatment with nitrous acid in strong mineral acid at 0-5°C due to the highly exothermic nature of the diazotization and any subsequent reactions [93], and organic synthesis in protic solvents using amyl nitrites and catalytic amounts of strong acid is also possible [94]. The diazonium intermediate, 5-diazotetrazole, is highly explosive and should not be brought to dryness, making its generation and consumption in a continuous multistep synthesis approach attractive. Previous work has demonstrated multistep synthesis of azo dyes using the formation and coupling of diazonium intermediates [13].

We demonstrate the synthesis of sodium 5-nitrotetrazolate (NaNT) through the diazotization of 5-aminotetrazole and subsequent nitration. A kinetic analysis of the individual reaction steps is undertaken to obtain rate constants and activation energies. Insight into the reaction mechanism is gained by adjusting the pH conditions of the substitution reaction to optimize the reaction rate and streamline the overall synthesis. Diazotization reaction studies are performed in parallel to improve data acquisition rates. Lastly, we estimate the maximum rate of NaNT production per reactor chain based on the kinetic parameters and microreactor configuration used in this study.

5.1.1 Experimental

5.1.1.1 Microfluidic Mixer Design

We designed the mixer to use diffusive mixing enhanced by flow bifurcation. Diffusive mixing time scales with the square of the path length, hence a single flow

bifurcation results in a four-fold decrease in mixing time. The total width of the channel was 50 μm, giving a path length of 12.5 μm and a characteristic mixing time of ~ 0.16 s. We allowed 3x the characteristic mixing time to ensure complete mixing, or ~ 0.5 s.
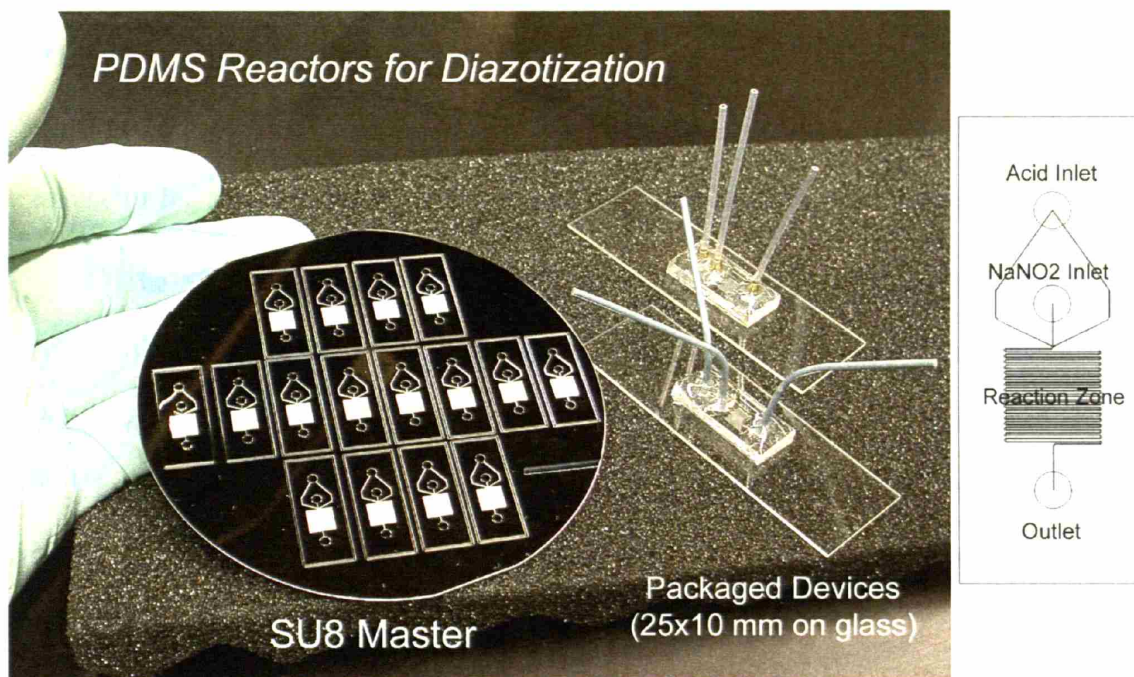
Figure 5.1 The silicon SU-8 master mold is shown next to packaged devices (left). A schematic of the device layout is also shown, with two inlets, a mixing/reaction volume, and outlet (right)

The mixers (Figure 5.1) were fabricated using a soft-lithography process. A 100-mm silicon wafer (Silicon Quest International, Inc.; Santa Clara, CA) was dehydrated for 60 min at 200°C. The wafer was transferred directly to a spin coater and ~ 3 mL of SU-8 2050 photoresist (MicroChem Corp.; Newton, MA) was coated onto the wafer at 750 rpm for 15 s, followed by 1000 rpm for 60 s. This was baked at 65°C for 1 min, then the temperature was ramped up to 95°C for 30 min to evaporate the solvent. A second coating of resist was spun on and the solvent bake repeated to bring the resist thickness to

~ 160 µm. We found that it was critical to maintain a level surface while baking the resist using this recipe or the film will be non-uniform.

We exposed the resist through a blank glass plate and transparency photomask (Pageworks; Cambridge, MA) for 45 ± 5 s (9 x 5s with 2s intermission), then baked the resist at 65°C for 1 min and 95°C for 12-15 min. The resist was developed in 30-60 minutes using PGMEA developer with frequent agitation and fresh developer.

The SU-8 master was then silane vapor treated using n-octyltriethoxysiloxane (United Chemical Technologies, Inc.; Bristol, PA) for 3-6 hours in a vacuum chamber. Polydimethylsiloxane (PDMS, Sylgard 184, Dow Corning; Midland, MI) was mixed 10:1 with its activator, degassed in a vacuum chamber to remove all bubbles, then cast onto the SU-8 master. The PDMS was baked for ~ 3 hours at 70°C. After coming to room temperature, the PDMS was removed.

Packaging of the PDMS devices required first cutting fluidic ports through the silicone rubber layer with a 5/64" punch. The surfaces are cleaned with tape thoroughly to remove all dust on the bonding areas. Pieces of silicon wafer were broken using a diamond scribe to a size just larger than the PDMS, then cleaned with isopropanol and dried with nitrogen. An oxygen plasma asher was used to clean the surface of any residual organics for 60 s. Using tape to protect the non-bonding surfaces, the silicon piece and PDMS device were plasma treated for 35 s, then removed from the chamber and contacted immediately. After resting for at least 5 minutes, about 5 cm of 1/16" OD (0.01" ID) PTFE tubing (Upchurch Scientific; Oak Harbor, WA) fitted with 1/16" metal ferrules were inserted into the holes made for the fluidic connections. The device was plasma treated for 60 s, and then 5-minutes epoxy was used to fix the tubing in place.

Fluidic connections were made with 1/16" tubing connections (Upchurch Scientific). Different lengths of 1/16" PTFE tubing were used to customize the reaction volume for each reaction study, with volumes of 3.3 and 62 μL (including the micromixer and depending on the residence time) for the diazotization reaction and 230 μL for the substitution reaction.

5.1.2 Procedures

Reagents were used as received and prepared in deionized water from a Milli-Q water purifier unless otherwise noted. For the diazotization reaction studies, 0.025 M 5-aminotetrazole (5-AT, Lancaster Synthesis, Inc.; Pelham, NH) was dissolved in 1.5 M sulfuric acid and 0.025 M and 0.05 M sodium nitrite (Alfa Aesar; Ward Hill, MA) were dissolved in water. The reagents were injected at equal flowrates ranging from 5-50 μL/min each and temperatures were adjusted to 5-30°C using a waterbath. 2M NaOH (Mallinkrodt Chemicals; Phillipsburg, NJ) was prepared and used to quench the reaction. The reaction volume was 3.3 μL, giving residence times from 2-10 s.

Sodium 5-nitrotetrazolate (NaNT) synthesis utilized 0.05 M 5-AT in 1.5 M sulfuric acid and 0.2 M sodium nitrite. These were fed through a 62 μl volume 1:1 at a total flowrate of 10 and 20 μl/min. The buffer stream to adjust pH in the second reaction step was 0.4 M citric acid monohydrate (Mallinkrodt) in 2 M NaOH. The nitration reaction volume was 230 μl and consisted of 1/16" ID PTFE tubing. A 4 M NaOH stream was used to quench the reaction using an Upchurch T-mixer. The acid, nitrite, buffer, and quench streams had a flow ratio of 1:1:n:1 where n was varied between 0.5-3. Flow at 5 and 10 μL/min of each acid/nitrite/buffer stream was studied.

5.1.3 Process

The synthesis of NaNT requires two reaction steps involving the diazotization of a primary amine followed by a de-diazotization/nitration reaction. For the first reaction step, we studied the kinetic parameters at several flowrates using a small reaction volume for a low residence time, followed by a quench.

To study the nitration reaction, we formed the diazonium ion in the first step using sufficient reaction volume to allow complete conversion followed by a second mixer to adjust the pH of the reaction and a relatively large reaction volume.

Parallelization of experiments allowed more efficient data collection (Figure 5.2). By running multiple reaction chains, we were able to study the order of reaction by varying a reagent concentration and double the data acquisition rate. The improved data acquisition rate compensates for a time-consuming setup.

HPLC analyses were performed on a Waters system with a 1525 binary pump, 717plus autosampler, and 2996 autosampler on a 3.9x150 mm C18 column (Waters WAT086344). A 0.1M monobasic phosphate buffer was pumped isocratically at 1 ml/min. Retention of all compounds was very low, though the NaNT was retained the longest with a peak absorbance near 256.7 ± 0.5 nm. Peak hydroxydiazonium absorbance is 261.5 ± 0.5 nm.
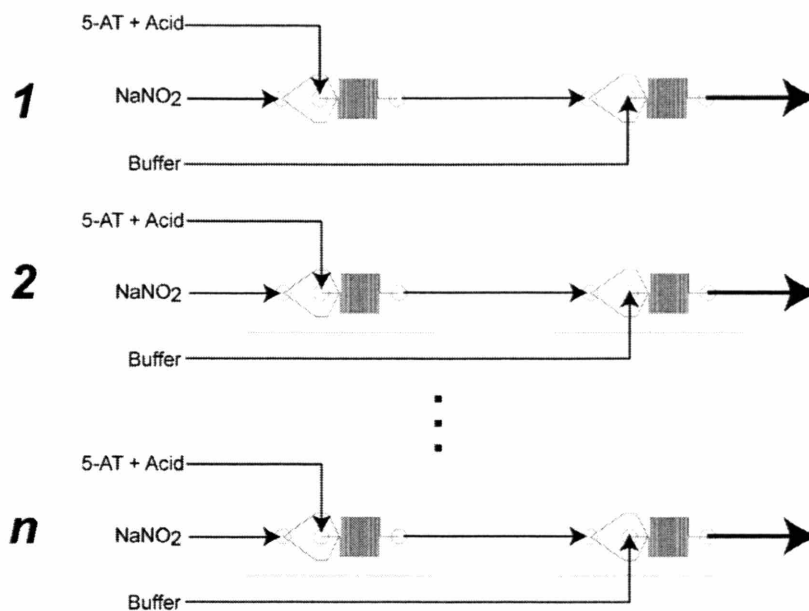
Figure 5.2 A schematic of a parallelized multistep reaction chain. As many as three parallel experiments were run in this study, limited by the number of spaces available on the syringe pumps.

5.2 Results

5.2.1 Reaction Model for Diazotization of 5-Aminotetrazole

The rate of formation of 5-diazotetrazole was assumed to be similar to other diazotization kinetic studies under moderately acidic (0.1-6.5 M) conditions. The rate equation includes terms for both the neutral and protonated amine, even though the former (i.e. the neutral form) reate is typically $3 \cdot 10^2$-$3 \cdot 10^4$ times faster [95].

$$(5.1)$$
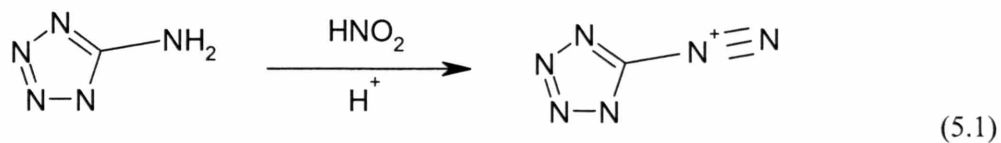
$$rate = k_1 [ArNH_2][HONO]h_o + k_2 [ArNH_3^+][HONO]h_o \qquad (5.2)$$

Since the first term is much faster than the second, we assume that the second term is negligible. Moreover, the acidity h_o is considered constant. The rate expression then takes the form:

$$rate = -\frac{d[5AT]}{dt} = k_1'[5AT][HONO] \tag{5.3}$$

The concentration of nitrous acid can be rewritten in terms of 5-AT to simplify the differential equation.

$$[HONO] = [5AT] + ([HONO]_o - [5AT]_o) \tag{5.4}$$

$$\frac{d[5AT]}{dt} = -k_1'[5AT]([5AT] + [HONO]_o - [5AT]_o) \tag{5.5}$$

Integration of Equation (5.5) can be integrated to give the concentration of 5AT as a function of time:

$$[5AT] = \frac{[5AT]_o - [HONO]_o}{[5AT]_o - [HONO]_o e^{([HONO]_o - [5AT]_o)k_1't}} \tag{5.6}$$

Rearranging and solving for the rate constant yields:

$$k_1' = \frac{\ln\dfrac{[5AT]_o([TzN_2] - [HONO]_o)}{[HONO]_o([TzN_2] - [5AT]_o)}}{([HONO]_o - [5AT]_o)t} \tag{5.7}$$

Practically, the diazonium can be converted to a hydroxydiazonium/nitrosylamine by quenching the reaction with strong base to produce a stable product that can be detected by HPLC. We assume that this quenching reaction is fast compared with the diazotization reaction because substituted phenyldiazonium ions reacts with a rate constant of 10^3-10^5 $M^{-1}s^{-1}$ at 23°C [95] and we use 1M NaOH to quench the reaction.

$$ (5.8) $$
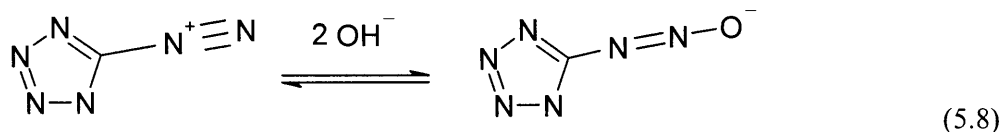
We assume an Arrhenius temperature dependence to give the rate constant as a function of the temperature and activation energy.

$$ k = k_o e^{\frac{-E_a}{RT}} \; ; \quad \ln k = \ln k_o - \frac{E_a}{RT} \qquad (5.9) $$

5.2.2 Experimental Results of 5-Aminotetrazole Diazotization

To obtain kinetic data for the system, temperature, flowrate, and concentration were varied. The concentrations of the reagents after mixing were 25 mM 5-AT in 0.75M sulfuric acid and 1 or 2 equivalents of nitrous acid for a parallel reaction setup. Under typical reaction conditions, the 5-AT was consumed in less than 1 min (Figure 5.3). We varied the total residence time in the system from 2-10 seconds (100-20 μl/min total flowrate through a 3.3 μl reaction volume). The kinetic parameters for the parallel experiments agreed well, supporting the second-order kinetic model [95]. We found the activation energy to be 37.8 ± 6.4 kJ/mol and the pre-exponential factor $\ln(k_o)$ to be 15.9 ± 2.7 $(M\ s)^{-1}$, giving 2.0 $(M\ s)^{-1}$ as the rate constant at 298 K (Figure 5.4)
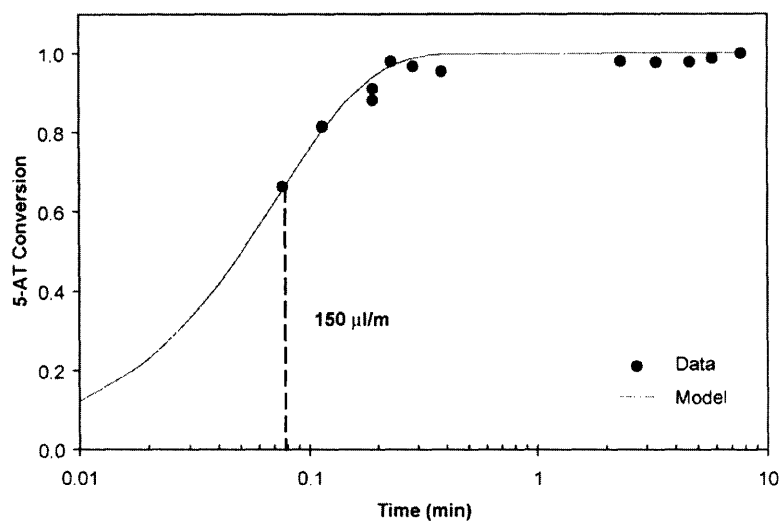
Figure 5.3 Conversion of 5-AT (C_o = 50 mM, 2 eq $NaNO_2$) to diazotetrazole proceeds in less than 1 minute, though the intermediate remains stable even at 20°C for more than 10 minutes.
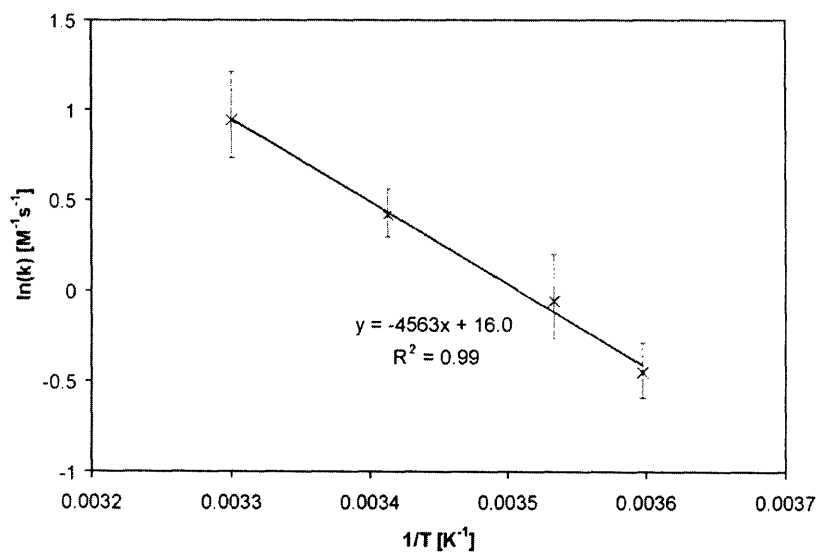
Figure 5.4 Determination of the kinetic parameters for 5-AT conversion to the diazonium. The slope is E_a/R and intercept $\ln(k_o)$. Data from two nitrous acid concentrations supports the overall second-order model.

5.2.3 Dediazotization/Nitration Reaction

The diazo group can be substituted with a nitro group on the tetrazolate ring to form 5-nitrotetrazolate, and nitrite ion is responsible for the dediazotization rather than nitrous acid. Dediazotization kinetics depends on the aromatic ring and its substituents, the substituting group, and temperature. By assuming a second-order rate equation, we arrive at the following:

$$\frac{d[NaNT]}{dt} = k_2 [TzN_2][NO_2^-] \tag{5.10}$$

The effect of pH on the reaction rate arises from the fast equilibrium between nitrite and nitrous acid (pKa ~3.27) and between the diazonium and diazohydroxide. The nitrite and diazonium concentrations can be written as:

$$\frac{[NO_2^-]}{[NO_2^-]_T} = \frac{10^{-pH+pK_a}}{1+10^{-pH+pK_a}}$$

$$\frac{[TzN_2]}{[TzN_2]_T} = \frac{10^{pH-pK}}{1+10^{pH-pK}} \tag{5.11}$$

where the subscript T denotes the sum of all forms of that species. Graphically, plots of Equations (5.10) and (5.11) show that a maximum reaction rate is expected (see Figure 5.4).

Substituting back into Equation (5.10), the rate depends on pH and the total concentrations of the diazonium and nitrite ions (Figure 5.5).

$$\frac{d[NaNT]}{dt} = k_2 f(pH)[TzN_2]_T[NO_2^-]_T$$

$$f(pH) = \frac{10^{pK-pK_a}}{\left(1+10^{pH-pK_a}\right)\left(1+10^{pK-pH}\right)} \tag{5.12}$$

100

We write the nitrite ion in terms of the diazotetrazole to obtain the following expression:

$$[NO_2^-]_T = \left([NO_2^-]_{T,o} - X_1[5AT]_o\right) - \left(X_1[5AT]_o - [TzN_2]_T\right) \tag{5.13}$$
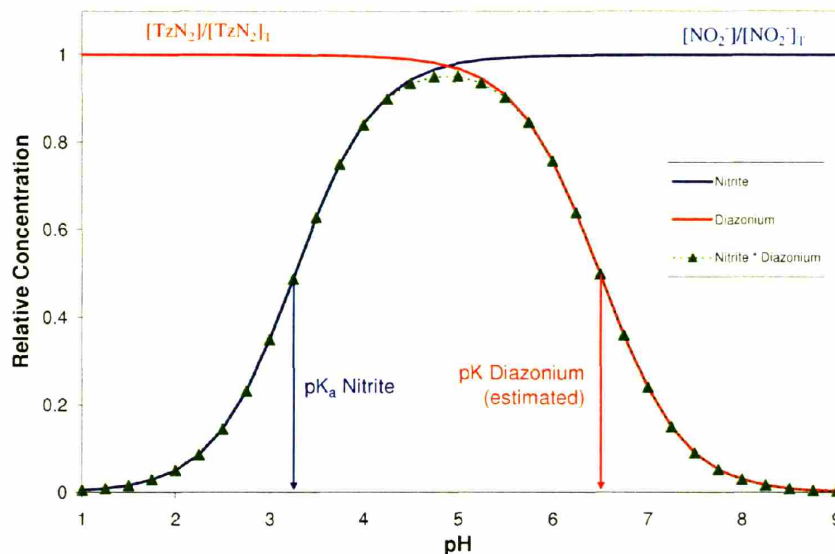
Figure 5.5 The relative concentration of the reagents depends on the pH of the reaction mixture. The product of the two concentrations (green triangles) shows that a maximum reaction rate is expected.

The term X_1 is the conversion of the diazotization reaction, usually ~ 0.95-1. Equation (5.13) is substituted back into (5.12), and the *NaNT* concentration is expressed as a function of time.

$$[NaNT] = X_1[5AT]_o\left(1 + \frac{[NO_2^-]_{T,o} - 2X_1[5AT]_o}{X_1[5AT]_o - \left([NO_2^-]_{T,o} - X_1[5AT]_o\right)e^{k_2 f(pH)\left([NO_2^-]_{T,o} - 2X_1[5AT]_o\right)t}}\right) \tag{5.14}$$

As before, rearrangement gives k_2 as a function of the [*NaNT*].

$$k_2 = \frac{-\ln\dfrac{X_1[5AT]_o\left([NaNT] + X_1[5AT]_o - [NO_2^-]_{T,o}\right)}{[NaNT]\left([NO_2^-]_{T,o} - X_1[5AT]_o\right) + X_1[5AT]_o\left(X_1[5AT]_o - [NO_2^-]_{T,o}\right)}}{f(pH)\cdot\left(2X_1[5AT]_o - [NO_2^-]_{T,o}\right)\cdot t} \tag{5.15}$$

101

It has been noted that ionic strength, particularly halide concentration, has a significant catalytic effect on the rate of dediazotization and substitution [95]. In this study, the use of halides was avoided to prevent the possible formation of a halo-tetrazole (i.e. chloro-tetrazole). According to Debye-Hückel theory, the natural log of the activity should scale with $I^{0.5}$. However, the ionic strength of the reaction medium was not varied significantly, as values of $I^{0.5}$ ranged from 1.5-2.2 molal$^{0.5}$.

5.2.4 Experimental Results – Nitration Reaction

First, we examined the effect of pH on the substitution reaction by varying the buffer flowrate. We used 0.4 M citric acid in 2 M sodium hydroxide to control the pH in the range of 3-6. Below pH ~3, very little conversion to NaNT was observed. Once the pH was raised to 3-6, NaNT formation was observed via HPLC detection. In the pH range 7-9, we could not collect significant data due to the ineffectiveness of the buffer to give repeatable pH control. We observed an optimum conversion rate (Figure 5.6) at ~ pH 5. Assuming an Arrhenius temperature dependence of rate on temperature, the activation energy was 60.0 ± 7.9 kJ/mol, and the $\ln(k_o')$ was 16.6 ± 3.2 (M s)$^{-1}$ to give a rate constant of $5.1 \cdot 10^{-4}$ (M s)$^{-1}$ at 298 K (Figure 5.7).
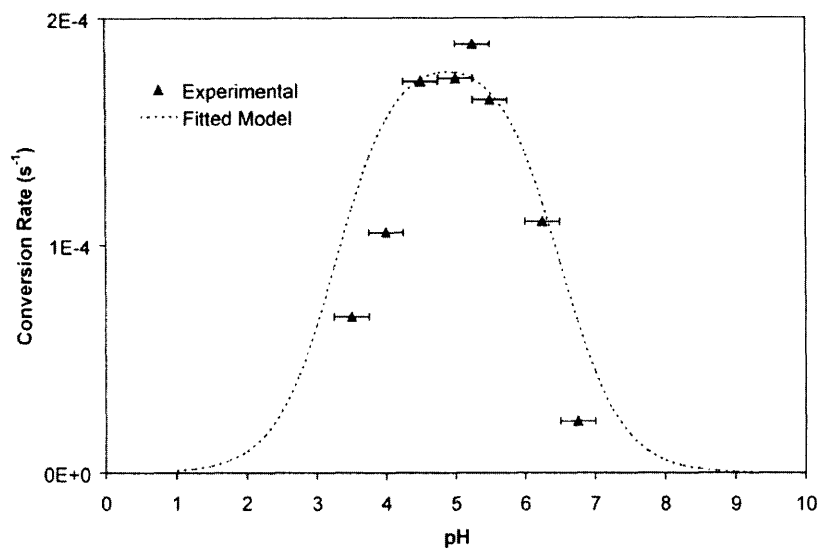
Figure 5.6 Effect of pH on the conversion to NaNT. The experimental conversion rates for one data run are shown compared with a model using fitted parameters for the effective diazonium pK and the peak conversion rate.
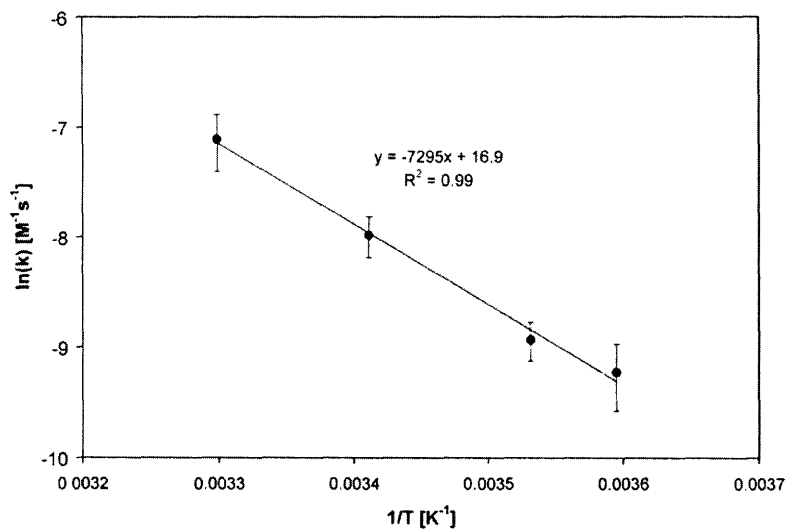
Figure 5.7 Plot of kinetic parameters for the nitro substitution of the diazo group on the tetrazole ring. The slope is E_a/R and the intercept is the $\ln(k_o)$.

5.2.5 Estimated Maximum Production Rates

We found that the mixing time was the most important factor limiting throughput in this system, as heat transfer and residence time are easily controlled. Based on the current design, a throughput of 150 µL/min (total flow) could be achieved and maintain complete mixing. Using 0.5 M 5-AT in 1.5 M sulfuric acid with 2 equivalents of sodium nitrite maintains excess acid for the reaction to proceed. This can be achieved using a 3:1 flow ratio with 3 M NaNO$_2$. For the second reaction step, the total flow from the buffer stream and diazotization reaction streams (1:1) would total 150 µL/min. This effectively dilutes the 5-AT reagent by 0.375, corresponding to a production rate of $2.8 \cdot 10^{-5}$ mol NaNT/min.

5.3 Conclusions

This microfluidic system enabled studying the kinetic behavior of 5-AT diazotization and the subsequent nitration reactions in the synthesis of NaNT at temperatures normally deemed too hazardous for benchtop synthesis. The diazotization reaction and subsequent nitration reaction both appeared to be second order. To our knowledge, this study is the first to determine kinetic parameters for the NaNT synthesis. Controlling pH was an important factor in optimizing conversion in the second step, indicating nitrite ion is likely responsible for the nitration instead of nitrous acid. In addition, we were able to streamline the overall synthesis taken from the batch process by removing the copper nitrotetrazolate salt precipitate without byproduct formation or degradation of the diazonium intermediate.

PDMS microdevices bonded to silicon substrates were used to mix the reagents, enabling fast mixing and high heat transfer rates to maintain isothermal reaction conditions. Parallel reaction chains were run co-currently to double the rate of data acquisition. Based on the results of this study, we determined that the maximum production rate for a single reaction chain is ~0.028 mmol/min. However, the recommended material of construction for devices used to produce NaNT should be glass or silicon, as the long-term PDMS stability may be an issue. A full description of the fabrication and packaging and material selection and compatibility are discussed in the Appendicies.

Chapter 6. Conclusions and Recommendations for Future Work

The study of continuous-flow separations for microchemical systems is summarized, with highlights of the technologies and models developed during this thesis work. A discussion on current challenges is also presented, as well as recommendations for further development and application of the work presented.

6.1 Conclusions and Summaries

6.1.1 Continuous Dielectrophoretic Size-Based Particle Sorting

A microfluidic device with slanted planar interdigitated electrodes was developed and used to sort particles based on size. An analytical model describing particle motion was developed using the physical parameters of the system to simulate the behavior of solid polymer spheres subjected to fluid flow. This model was useful in device design and provided insight into the scaling of the particle motion with flowrate, E-field strength, and particle size. Single-size particle motion was characterized using a parametric study varying particle size, flowrate, and E-field strength, and showed good agreement with the theoretical model. A mixture of similarly sized particles was then continuously separated.

6.1.2 Electric-field Enhanced Coalescence for Surfactant-Enhanced Liquid-Liquid Extraction

Chemical extraction exploiting the high surface-to-volume ratios of emulsions formed in microchannels is effective in reducing the time to reach equilibrium, but phase separation of the two liquid phases must be separated before further processing can be done. Common methods of demulsification include salting the aqueous phase and temperature changes, but these approaches can be ineffective for water-in-oil emulsions. Such systems are commonly encountered in crude oil production, and it has long been established that electric fields can induce coalescence of the dispersed aqueous phase if sufficiently large electric fields are applied. This technique was found to scale with decreasing size and was implemented in microchemical systems using moderate applied voltages ~10 V to generate large AC E-fields ~10^5 V/m that drive droplet coalescence.

In addition, reverse micellar extraction using microemulsions formed in the continuous organic phase were exploited to improve single-stage extraction yields of two model chemical species. Due to the general difficulty and lack of multistage microfluidic extraction processes available, it is important to achieve high extraction yield from each extraction step. This was demonstrated in our system using two model compounds whose apparent solubility increased with increasing surfactant concentration.

6.1.3 Integrated Liquid-liquid Extraction and Phase Separation by Capillary Forces

Phase separation of immiscible liquid-liquid fluids in microfluidic devices was achieved using preferential wetting and capillary forces with a porous PTFE membrane. A detailed analysis of the pressure requirements for phase separation using capillary forces revealed throughput limitations depend primarily upon pore size and density, but also on hydrodynamic pressure drops associated with both separated fluid streams. Using the Young-Laplace equation for capillary pressure, interfacial tension and the three-phase liquid-liquid-solid contact angle define the maximum operating pressure at the point of phase separation. For systems with a high fraction of a partially miscible component, which is not uncommon in a practical chemical extraction, the maximum throughput is significantly reduced due to reductions in capillary pressure. A porous PTFE membrane was found to give the widest range of operation for the greatest number of liquid-liquid systems, due mainly to the hydrophobic nature of the material. Using a membrane compressed between two fluid channels, a model system of hexane-water with varying amounts of isopropanol was separated and the maximum operating flowrate at each concentration were found.

An integrated liquid-liquid extraction device was fabricated in silicon that incorporated mixing, phase contacting, and a porous membrane separator. Solvent extraction of N,N-dimethylformamide (DMF) from two organic phases was demonstrated and agreed well with equilibrium extraction experiments. A solvent switch of the antibiotic erythromycin ethylsuccinate was performed, transferring it from DMF to dichloromethane without detectable loss of the antibiotic to the aqueous phase.

6.1.4 Kinetic Studies of Sodium Nitrotetrazolate Formation via Multistep Synthesis in Microreactors

Microreactors were used to study the synthesis of the energetic material sodium nitrotetrazolate (NaNT). The two major reactions to synthesize NaNT involve diazotization of the aminotetrazole starting compound, followed by a de-diazotization (nitro substitution) reaction. Microreaction technology enabled studying the chemical kinetics of each reaction at 25-40°C, far beyond what is normally considered safe for a benchtop synthesis. The synthesis was streamlined to remove a solid intermediate that requires additional reaction steps and separation, and poses a significant explosion hazard during manufacture. Insight into the reaction mechanism was also gained as the pH of solution was found to be an important parameter controlling the substitution reaction rate, with a significant increase in rate corresponding to the pK_a of the substituting species. This enabled optimization of the substitution reaction rate and overall synthesis.

6.2 Outlook and Suggestions for Future Work

6.2.1 Multistage Separations Processing

In practice on the macroscale, multistage separations are employed for complete separation of chemical species. This is highly effective because density difference of the two phases drive the flows countercurrent to one another, full or partial equilibrium is established along the height of the column, achieving a high degree of separation. Countercurrent flow in microfluidic devices is largely unrealized because of laminar flow of the fluids. For those that have achieved countercurrent flow, maintaining stable countercurrent flow in microdevices is difficult without small surface-to-volume ratios or

surface modification of the channels. This was documented in Chapters 3 and 4 of this thesis.

To achieve multistage separation, multiple co-current flow devices can be arranged in series with fresh solvent added for each stage. This utilizes the advantages of slug flow contacting for high mass transfer rates while maintaining simple contacting and separation steps. Another way to achieve countercurrent flow is to use a porous solid partition between the two fluid phases. In principle, a thin membrane with thin film flow would offer little mass transfer resistance [96, 97]. Practically, long channel lengths are required to allow sufficient contact time for multistage separation and control of the pressure is an issue.

6.2.2 Distillation

Chemical separation based on differences in boiling point is ubiquitous in chemical processing. In many ways it is similar to extraction as a species partition between a gas and liquid phase depending on their chemical potentials. Typically, countercurrent flow is employed with multistage contacting, ranging from one to several hundred (e.g. ethane-ethylene systems) stages. The biggest problem on the microscale, aside from the difficulty of using countercurrent flow, is that liquids are ~1000 times denser than gases. As such, the volumes occupied and velocities of the two phases would be extremely different, making control in the system difficult. Heat pipes have been demonstrated as small total-reflux distillation devices using capillary forces to drive liquids and heating to induce vaporization and gas flow, but control of the fluid flow is still a major hurdle [98-100]. Other work of microfabricated distillation devices have yet to prove any chemical separation [101].

110

6.2.3 Multistep Chemical Synthesis

Ultimately, the purpose of microchemical technology is to facilitate and enable new chemical syntheses [102]. There are already a number of mixer, reactor, and now separator designs that can be found in the literature, most demonstrating model chemistries well-suited to their designs. These demonstrations have served a useful purpose to enlighten the chemical and biological communities as to the potential of microfluidic devices and have initiated scientific dialog between engineers and scientists. Now, research involving microchemical systems must begin to include significantly more applications rather than simply technology development. It is the difficulties encountered when linking micro unit operations together that will help to drive the technology forward. Clearly, collaboration between scientists and engineers will be required for this to be successful.

Microfluidic multistep synthesis is inherently difficult because of the time required to control and characterize each step. However, as each step is optimized it should become relatively straightforward to control the individual process steps. Areas such as packaging and process control will be tested to ensure the devices behave as designed and the data obtained from the devices are believable.

Robust continuous multistep microchemical synthesis is still largely unrealized; and several hurdles, both known and undiscovered, must be overcome before this technology becomes the standard for chemical research. Continuous separations are an integral part of these systems, and their development is critical to achieve the goal of rapid on-demand chemical synthesis and optimization.

Appendix A. Detailed   Microfabrication   and

Packaging Procedures

This appendix details the fabrication procedures used to manufacture the devices in Chapters 2-5 of this thesis. Fabrication was performed in the Microsystems Technologies Laboratory (MTL) at MIT, with the majority of work performed in the Technologies Research Laboratory (TRL) Class 100 cleanroom. Some fabrication was performed in the Integrated Circuits Laboratory (ICL) Class 10 cleanroom and the Exploratory Materials Laboratory (EML). Detailed fabrication procedures, photomasks, fluid packaging, and special procedures are explained in the following sections.

A.1 Dielectrophoretic Particle Separator Fabrication

The particle separator was fabricated in two parts consisting of an interdigitated electrode structure and a PDMS-molded microchannel. The key to successful fabrication of this device was both to keep the design simple and overall footprint small. Early problems were experienced with the interdigitated electrode structure due to small feature sizes (20μm) and very high feature density over a large area. In the final designs, the active electrode areas were shrunk to 10x30 mm and device size 22.5x40 mm. This gives 14 devices per 150mm wafer.

A.1.1 Detailed Process Description

The processes submitted to the process technology committee (PTC) are listed below. The electrode structures utilized a metal lift-off process, and the PDMS molds were made using soft-lithography techniques.

A.1.2 Electrode Structures

The procedure was followed as described with the exception that exposure of the photoresist was shortened to ~ 3 s. We also attempted to deposit other metals (e.g. copper) instead of Ti/Pt, however these corroded with an applied potential and aqueous solution.

DEP-focuser Process Flow   Jason Kralj (jkralj@mit.edu)

last modified: 6/19/03   Saif Khan (saifkhan@mit.edu)

Purpose: Fabricate a part of a micro dielectrophoretic focuser by patterning PYREX wafers with metal.

Starting Material:

1 6-in PYREX 7740 wafer

General Process:

Perform metallization lift-off to pattern interdigitated electrodes (Electrodes photomask) onto the pyrex wafer, then dice the wafer.

Process Steps

NOTE: All process steps should be conducted using RED labeled equipment

1. PATTERN WAFER FOR LIFTOFF

1.1	TRL	acidhood	piranha clean wafer
1.2	TRL	HMDS	deposit HMDS
1.3	TRL	coater	2 um coat frontside with AZ 5214 image reversal resist
1.4	TRL	prebakeoven	prebake 30 min at 90°C
1.5	TRL	EV1	Align wafer w/ Electrodes photomask and expose ~10 s
1.6	TRL	prebakeoven	postbake resist for 30 min at 90°C

| 1.7 | TRL | EV1 | Flood exposure for 45 s |

| 1.8 | TRL | photowet-r | develop resist using AZ422 for 2 min |

2. METALLIZATION AND LIFTOFF

| 2.1 | TRL | e-beam-Au | deposit 10 nm Ti/100 nm Pt for electrodes, leds, and contacts |

| 2.2 | TRL | photowet-Au | acetone soak for metal liftoff from PYREX wafer |

3. BOND AND DICE DEVICE

| 3.1 | ICL | diesaw | Dice wafer |

A.1.2.1 Fluidic Channel Mold

This procedure was based on the manufacturer's suggested process listed at microchem.com. At the time of writing this thesis, MTL had discontinued use of the SU8-10 photoresist, though a new SU8-2010 resist is allowed.

DEP-focuser-fluidics Process Flow   Jason Kralj (jkralj@mit.edu)

last modified: 5/29/03   Saif Khan (saifkhan@mit.edu)

Purpose: Fabricate the micro dielectrophoretic focuser fluidics using a patterned silicon master as a mold for PDMS.

Starting Material:

1 4-in undoped silicon wafer

General Process:

Spincoat and develop SU8 photoresist on a silicon wafer.

Process Steps

1. PATTERN WAFER

1.1	TRL	acidhood	piranha clean wafer
1.2	TRL	hotplate	dehydration bake at >120C for >30 min
1.3	TRL	pispinner	Dispense 3-5 mL SU8-10, spincoat to 30 um at 1000rpm for 60s
1.4	TRL	hotplate	65°C for 1 min, 95°C for 30 min to bake off solvent
1.5	TRL	EV1	Expose 5x5s using SU8 channels photomask
1.6	TRL	hotplate	65°C for 1 min, ramp to 95°C for 5 min
1.7	TRL	photowet-Au	Develop using PGMEA about 10 min, check with isopropanol
1.8	TRL	hotplate	*optional* hardbake SU8 at 200C for 30 min.

A.1.3 Masks

A.1.3.1 Electrodes

The masks were drawn with AutoCAD LT 2002 and printed by Pageworks (Cambridge,

MA) at the highest possible resolution. The electrodes were 50 μm lines and spaces on a

45° slant. A negative image transparency mask (5080 dpi) was printed emulsion up and

transferred to a chrome plate.
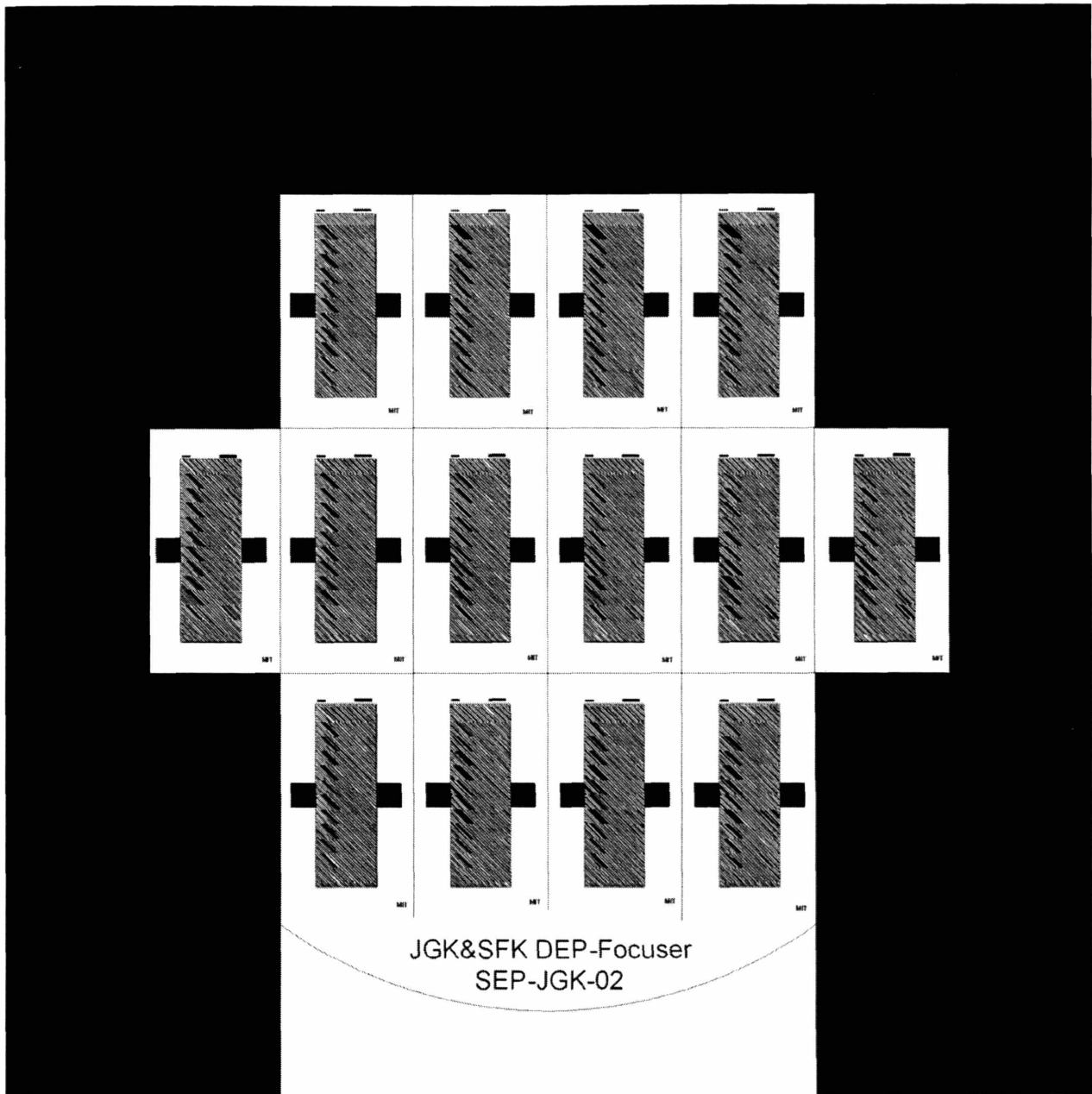
Figure A.1 Layout of the electrodes on a 150mm glass substrate. The final design had 50 μm lines and spaces on a 45° bias.

A.1.3.2 Fluidic Channels

The masks were also drawn with AutoCAD LT 2002 and printed by Pageworks (Cambridge, MA) at 5080 dpi with emulsion down for SU8 processing.
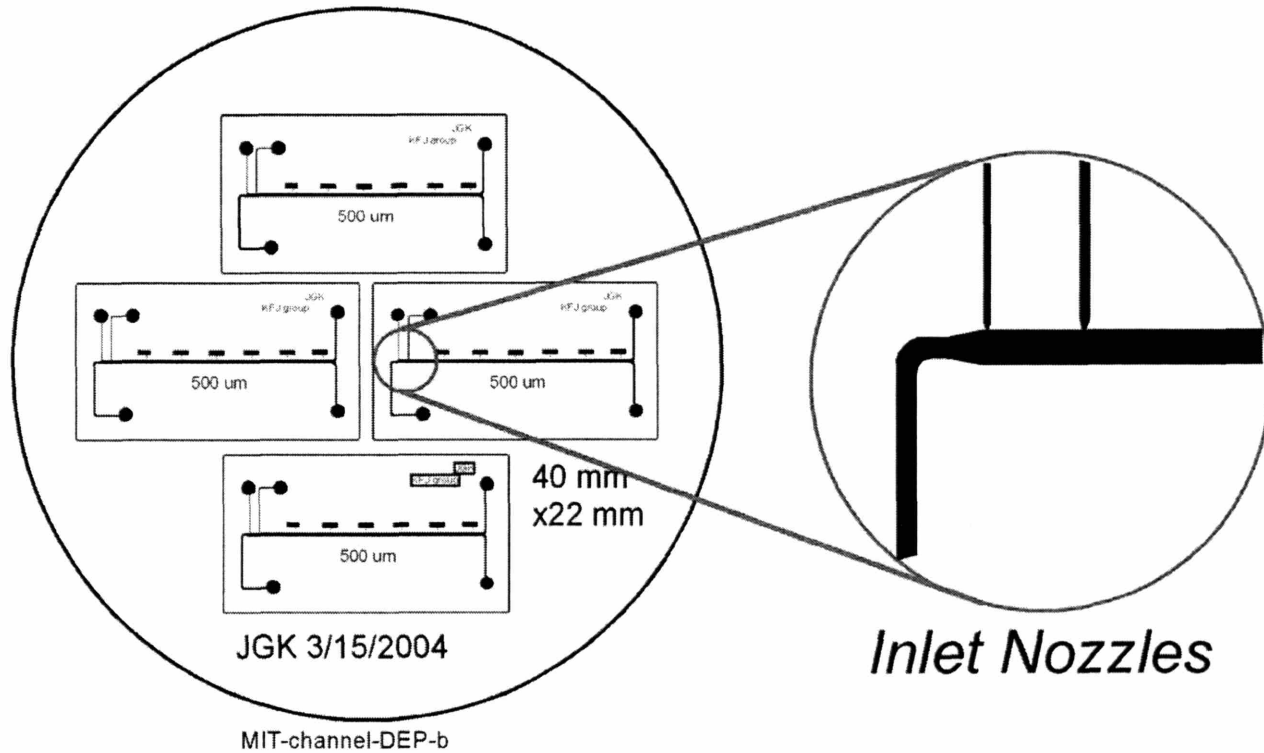
Figure A.2 An SU8 master was fabricated on a 100-mm silicon wafer. The inlet section is magnified to view the nozzles that ensure proper flow.

A.1.4 Packaging

To properly package the device, cleanliness and timeliness must be observed at all times. Be sure PDMS and glass surfaces, especially those being bonded, are cleaned with alcohol and Scotch tape is used to remove surface debris and protect the surface before moving to the plasma asher.

A trapezoidal piece was cut from both sides of the PDMS device to allow access to the electrode pads. A punch was used to make 1/16" holes in the device for the Upchurch

119

tubing. A sharp-edged punch is required to avoid tearing the PDMS, and practicing the punching technique on waste PDMS is helpful. The holes should be cleaned of debris using a piece of tape rolled into a small cone sticky-side out (a pencil is useful for this). The PDMS should be tape-cleaned several times until all surface debris are gone, and new tape used to protect the surface until bonding.

Activate the vacuum pump and plasma ash the bare glass surface for bonding (leave the tape on the other side) on high for ~ 1 min. This removes tape scum and any residual alcohol. It may be necessary to bleed a small amount of air through the needle valve to increase the plasma pressure (it should glow bright pink/purple). Again, this should be practiced beforehand. Turn the pump off and vent the chamber through the needle valve. Do not touch the exposed glass surface.

Next, remove the protective tape from the PDMS surface for bonding, taking utmost care not to touch the surface with anything, and place side-by-side with the glass substrate into the plasma asher on a tape-covered glass slide and pump down. Activate the plasma on high and time for 35 seconds. Each type of device may require slightly more or less time, but few devices bond permanently if ashed outside the 30-40 s window. Turn off the pump and vent through the needle valve. Carefully remove both pieces, align the devices as best as possible and place them in contact. Allow the surfaces to contact and bond without pressure for ~10-15 s, then press the PDMS gently where areas have not bonded. This should then rest for ~ 5 min before further processing.

For attaching tubing for pressure-driven flow, the desired tube length should be long enough so that fittings do not interfere with each other. We epoxied the tubing into place with 5-minute epoxy, though slower-drying formulations could be used. The bonded

120

devices are cleaned with Scotch tape once more and plasma ashed for ~60 s using the procedure detailed above. It may help to put the tubing in place while ashing. The goal is to help the epoxy adhere to the surface, though the bond was only satisfactory in our studies and failed after several hours of use. Compression sealing the PDMS device with the tubing in place (where the PDMS acts as its own gasket) could be used but was not employed here.

Electrical wiring was attached to the electrodes with conductive epoxy. Wiring was cut 3 cm long and exposed ~ 5 mm on each end. Epoxy was mixed and used to attach the wires and electrodes, then allowed to dry 24 hours. This can be done before or after plasma bonding the PDMS.

A.2 Electrocoalescence Device

This device was designed to have one inlet and two outlets, plus access to electrode structures. The key features were the electrodes patterned on the sidewalls of the channel in the device using a shadow mask and the use of CYTOP fluoropolymer to bond wafers and passivate the electrodes.

A.2.1 Detailed Process Description

The process submitted to the PTC is given below:

MicroDEP-3 Process Flow   Jason Kralj (jkralj@mit.edu)

last modified: 11/15/02

Purpose: Fabricate a micro dielectrophoretic separator by etching a Si wafer and bonding to a PYREX wafer.

Starting Material:

      1   6-in, double-side polished (100) Si wafers (undoped)
      1   6-in PYREX 7740 wafer

General Process:

First, etch flow channels in silicon wafer and oxidize. Next, deposit metal for electrodes. Finally, bond the wafers and dice the devices.

Process Steps

1. DEPOSIT NITRIDE ON SI WAFERS 1, 2, 3

1.1   ICL   rca   rca clean wafers for cvd

1.2   ICL   6D_Nitride   Deposit 1000-A Silicon Nitride on both sides of wafers

2. PATTERN FRONTSIDE OF SI WAFER TO DEFINE FLOW CHANNELS

2.1   TRL   HMDS   deposit HMDS

2.2   TRL   coater   1.2 um coat frontside with AZ915 resist

2.3   TRL   prebakeoven   prebake 30 min at 90°C

2.4   TRL   EV1   use channel mask, expose ~3-5 s

2.5   TRL   photowet-1   develop resist using OCG 834

2.6   TRL   postbakeoven   postbake 120°C for 30 min

2.7   ICL   LAM490   Remove exposed nitride layer using standard-nit-etch

2.8   TRL   acidhood   piranha clean wafer

3. PATTERN FRONTSIDE OF SI WAFER TO DEFINE INLET CHANNELS

123

3.1   TRL   HMDS   deposit HMDS

3.2   TRL   coater   1.2 um coat frontside with AZ915 resist

3.3   TRL   prebakeoven   prebake 30 min at 90°C

3.4   TRL   EV1   use inlet mask, expose ~3-5 s

3.5   TRL   photowet-1   develop resist using OCG 834

3.6   TRL   postbakeoven   postbake 120°C for 30 min

3.7   ICL   LAM490   Remove exposed nitride layer using standard-nit-etch

3.8   TRL   acidhood   piranha clean wafer

3. KOH ETCH FLOW CHANNELS AND PORTS

3.1   Schmidt Hood   KOH etch wafer ~4 hr (now YELLOW)

3.2   TRL   acidhood   post KOH clean (2 piranhas; 50:1 water:HF dip, 30 s)

4. GROW THERMAL OXIDE LAYER

4.1   TRL   tube B1   grow 4500-A wet oxide layer (~66 min, 1000°C) (now RED)

5. METALLIZATION OF WAFER BY GOLD LIFT-OFF

5.1   TRL   HMDS   deposit HMDS

5.2   TRL   coater   10 um coat frontside with AZ 5214-E

5.3   TRL   prebakeoven   prebake 30 min at 90°C

5.4	TRL	EV1	use electrodes mask, expose ~100-120 s
5.5	TRL	photowet-r	develop resist AZ 422 MIF
5.6	TRL	EV1	short flood exposure
5.7	TRL	postbakeoven	postbake 120°C for 60 min
5.8	TRL	e-beam	deposit 10 nm Ti/100 nm Pt for electrodes, leds, and contacts
5.9	TRL	photowet-Au	acetone soak to liftoff excess Pt

6. CLEAN PYREX

6.1	TRL	acidhood	Piranha clean wafer from vendor

7. BOND AND DICE DEVICE (1)

7.1	TRL	EV501-620	Anodically bond Si wafer and PYREX, 500 C, 800 V
7.2	ICL	diesaw	dice devices

KOH etching was performed in the Schmidt lab hood, however this is no longer allowed and should be performed in ICL/EML. Due to the fact that each wafer was etched a full wafer thickness, the wafer edges etched significantly from small scratches and left the wafer prone to breaking. Gentle rinsing after cleaning steps was employed to reduce shaking and damaging the wafers. Predrilled wafers were obtained from Dupont. Platinum was unavailable at the time, and gold was substituted. The actual anodic bond

recipe was 325C at 800 V. A lower temperature was selected because of fears that the gold might soften. Also, it was necessary to pump down and purge the bonding chamber twice before anodic bonding was successful. Arcing between the electrode and the bonding chuck due to residual oxygen was suspected.

Not included in this process is the wafer bonding using CYTOP CTL809M. Device bonding was performed on a die-by-die basis with a layer of CYTOP spun onto the backside of a channel wafer at ~ 1-2 krpm for 30s. This is baked 30 min at 95C to drive the solvent off. The inlet piece and channel/pyrex wafer stack were then aligned using a microscope and carefully transferred to a hotplate. Typically 2-3 devices were bonded each attempt, with a 6" square aluminum diffuser plate used to balance the load of ~ 20 kg of weight placed on the devices. The hotplate was then heated to ~ 200°C (above the reflow temperature of the polymer) and slowly cooled to ambient overnight.

A.2.2 Masks

All three masks were made by transparency transfer onto chrome plates. The highest resolution was employed (2560 dpi at the time). The top channel mask defined the flow channels, the inlet and outlet channels were defined by the KOH inlets mask, and the KOH shadow mask defined the areas for the KOH shadow mask. The KOH top channel was designed to have a small gap at the bottom of ~ 100 μm. The KOH inlets left a ~ 300 μm hole at the wafer bottom, making alignment of top and bottom wafers much more straightforward since this was done by hand.

A.2.2.1 Top

JGK March 2002
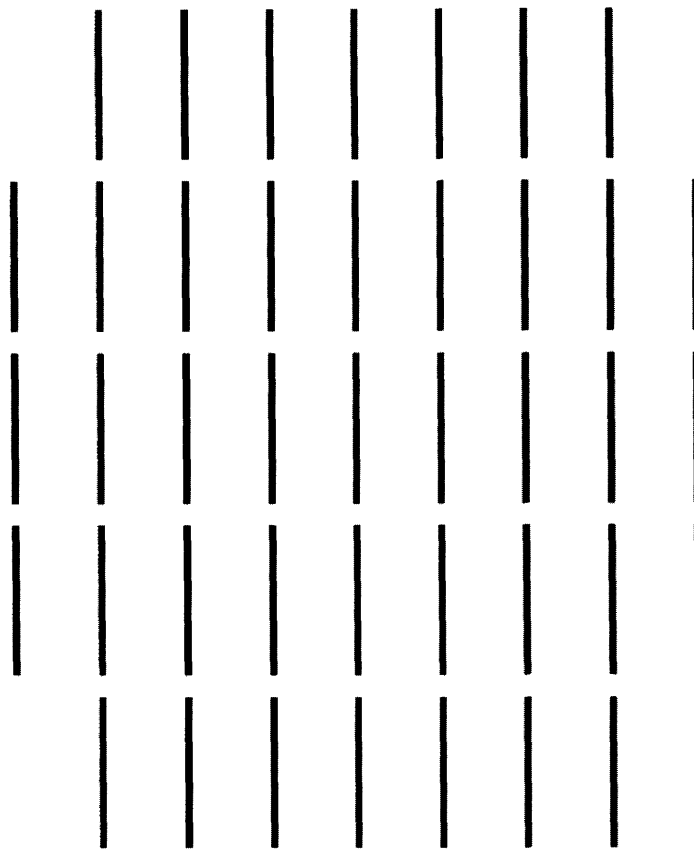
KOH Channel Mask

Figure A.3 Mask for flow channel. The lines near the bottom of the mask allow for alignment with the wafer flat.

A.2.2.2 Bottom

KOH Inlet Mask
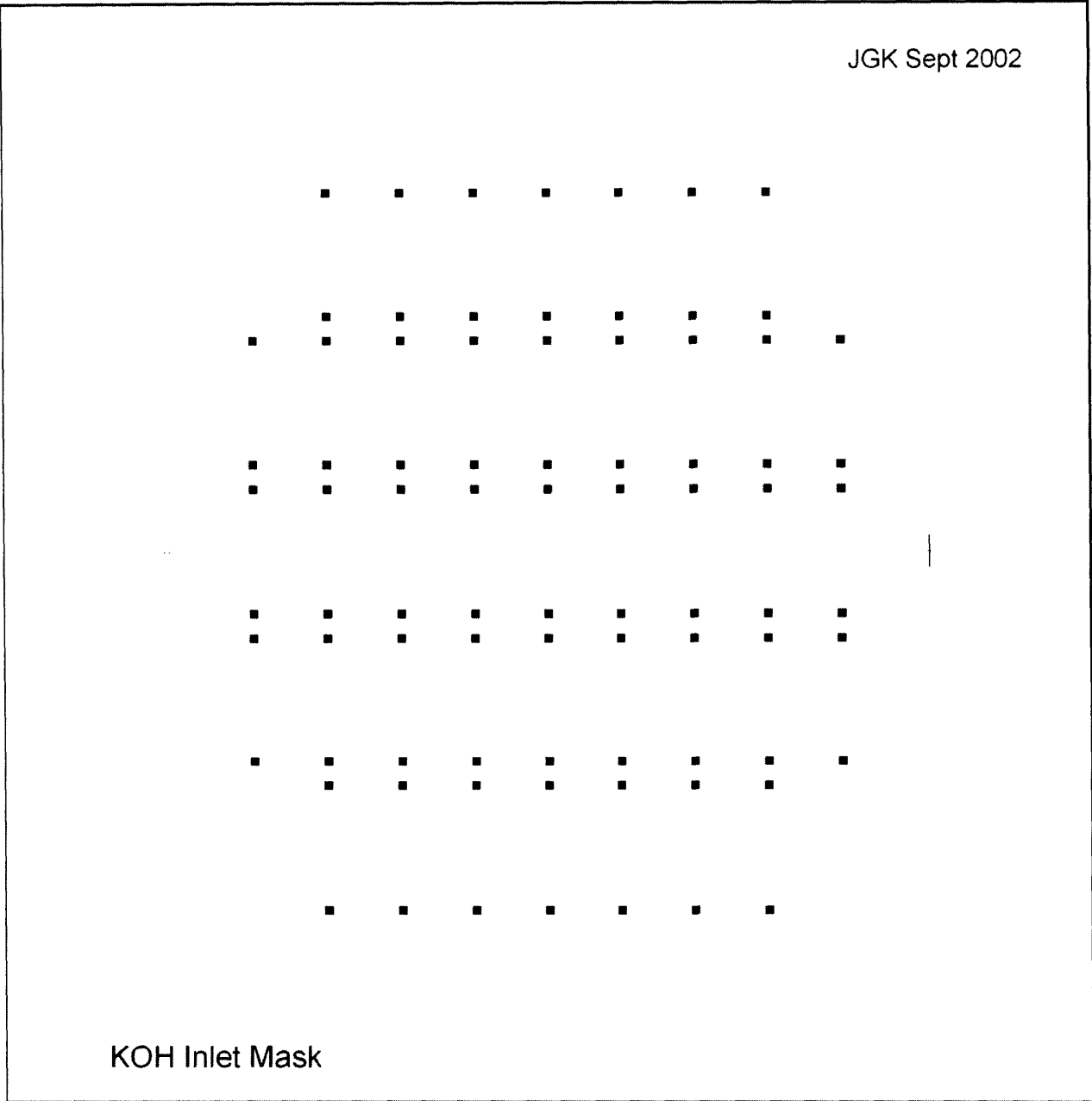
Figure A.4 Inlets and outlets are defined using the backside mask.

A.2.2.3 Shadow
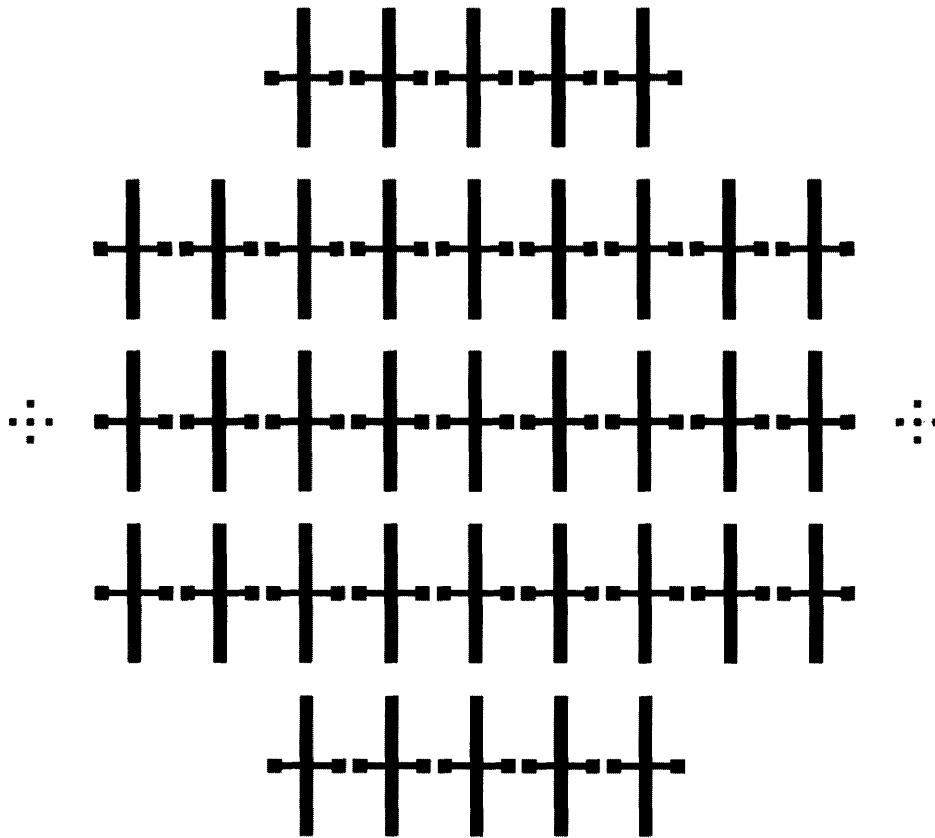
Figure A.5 KOH Shadow Mask was used to define the areas on a silicon wafer for through etching. The silicon shadow mask was used to define the electrode structure on the channel wafer with alignment achieved using a microscope.

A.2.3 Packaging

A.2.3.1 Fluid Chuck

The fluid chuck was machined in aluminum and acrylic. The aluminum piece was 3.4 x 2.2 x 1 mm in size, and holes were machined corresponding to the inlets/outlets of the device with ¼"-28 threaded holes made to fit with Upchurch fittings. The acrylic top was ½" thick with holes drilled for the compression screws, electrical pogo pins, and top outlet. A Viton gasket was cut to fit the chuck and holes punched to allow fluid to pass.

A.2.3.2 Mixer

The mixer was machined in aluminum and a viton gasket was used with a topplate to seal the mixer. A small magnetic stir bar was placed inside the mixer which was actively run at ~500-800 rpm during experiments.
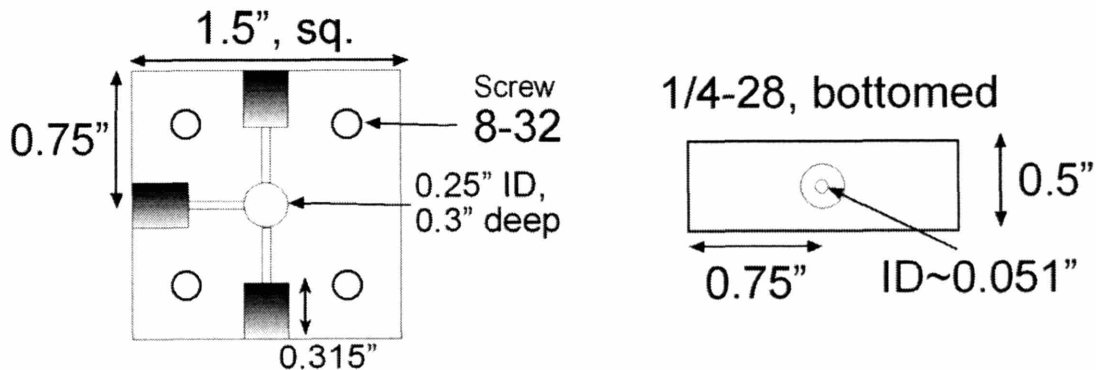
Figure A.6 The top view of the aluminum mixer (left) shows the screw holes (shaded), flow channels, and center mixer. The side view (right) shows the other dimensions of the device.

A.2.3.3 Electrical

Pogo pins were epoxied into the acrylic top plate and wiring screwed into an electrical relay epoxied to the side of the acrylic top plate. The relay made for simple connection to the function generator using alligator clips.

130

A.3 Membrane Separator

Fabrication of an extraction device with integrated mixing, extraction, and separation zones required good device layout and packaging the membrane in such a way that fluidic connections and the membrane were properly sealed.

A.3.1 Detailed Process Description

This silicon process utilized a two-step KOH etch for front and backside etching with mask compensation features to protect exposed corners from significant underetching. The details of the corner compensation are documented in the section devoted to masks.

STEP	DATE	FAC	wafer #	MACHINE	ACTION	NOTES	CODE
1					**PATTERN AND ETCH FLUIDIC CHANNELS**		
1.1					*BACKSIDE OF SI WAFER TO DEFINE FLOW PORTS*		
1.1.1		TRL	1	HMDS	Coat wafer with HMDS		
1.1.2		TRL	1	coater	coat frontside with 1 um OCG825 resist		
1.1.3		TRL	1	prebake	Bake at 95°C for 30 minutes		
1.1.4		TRL	1	EV1	Expose resist for 2 seconds (Separator backside mask)		
1.1.5		TRL	1	photowet-1	Develop AZ915, 1-3min		
1.1.6		TRL	1	postbake	Postbake at 120°C for 30 minutes		
1.1.7		ICL	1	Lam490	etch 5000A nitride using nitride-on-si		
1.1.8		TRL	1	acidhood	piranha clean wafer		
1.2					*KOH Etch Inlets/Outlets*		
1.2.1		ICL	1	TMAH-KOH hood	25%, 80°C KOH etch wafer to 340 um (~5 hr)		
1.2.2		TRL	1	acidhood	post KOH clean (2 piranhas; 50:1 HF dip)		

1.3				*FRONTSIDE OF SI WAFER TO DEFINE FLOW CHANNELS*	
1.3.1	TRL	1	HMDS	Coat wafer with HMDS	
1.3.2	TRL	1	coater	coat frontside with 1 um OCG825 resist	
1.3.3	TRL	1	prebake	Bake at 95°C for 30 minutes	
1.3.4	TRL	1	EV1	Expose resist for 2 seconds (Separator channels mask)	
1.3.5	TRL	1	photowet-1	Develop AZ915, 1-3min	
1.3.6	TRL	1	postbake	Postbake at 120°C for 30 minutes	
1.3.7	ICL	1	Lam490	etch 5000A nitride using nitride-on-si	
1.3.8	TRL	1	acidhood	piranha clean wafer	
1.4				*KOH Etch channels*	
1.4.1	ICL	1	TMAH-KOH hood	25%, 80°C KOH etch wafer to 200 um (~2 hr)	
1.4.2	TRL	1	acidhood	post KOH clean (2 piranhas; 49% HF)	Combines process steps to clean + rmv nitride film
1.5				*OXIDIZE WAFER*	
1.5.1	TRL	1	TubeB1	Grow 0.5 um wet oxide, 0.8 h @ 1000°C	
2				**DEVICE PACKAGING**	
2.1				*CAP DEVICE*	
2.1.1	TRL	2	acidhood	piranha cleaned Pyrex	
2.1.2	TRL	1,2	EV620	Align and bond Pyrex and channel wafers	
2.2				*DICE DEVICE*	
2.2.1	ICL	1,2	diesaw	dice devices	

One unusual step is the use of 49% HF acid to remove the silicon nitride film. Typically, this is done using hot phosphoric acid. However, we found that it was easier to combine film removal and post-process cleaning procedures and actually saved time by

132

eliminating a process step despite the slow (5000 Å in 20-60 min) etch rate of nitride in HF.

A.3.2 Masks

Mask making for this process required taking into account design requirements for mixing and extraction while addressing the issue of corner protection. The mixer is capable of relatively high throughput due to the long length and bifurcation of the flow, but has a high pressure drop of ~ 6 bar at flowrates approaching 40 μl/min. The contactor is designed to talk the droplets/slugs formed from the contactor and expand into a wide channel for an increased surface-to-volume ratio. And the separator was simply a wide trench through the wafer. Each posed different problems for the mask as corner compensation calculations give a maximum etch depth beyond which the exposed corner will undercut. We optimized for the extraction channel, as the mixing would probably not worsen significantly and the separator configuration was not critical.

The relationship between feature sizes and etch depths was solved previously [79].

$$\frac{V_{411}}{V_{100}} D_e = 0.857 \left(0.424B - 0.4w_2 + 0.4w_3 \right) \tag{A.1}$$

The dimensions are shown in Figure A.6 and D_e is the etch depth. Solving for D_e gives the maximum depth the corner compensation structure can protect.

$$D_e \leq \frac{\left(w_3 - w_2 \right)}{0.398 + 0.730 \dfrac{V_{411}}{V_{100}}} \tag{A.2}$$

As a rule of thumb, the depth must not exceed ~0.6-0.7 of w_3, meaning etching to the bottom of a channel is also not possible.

133
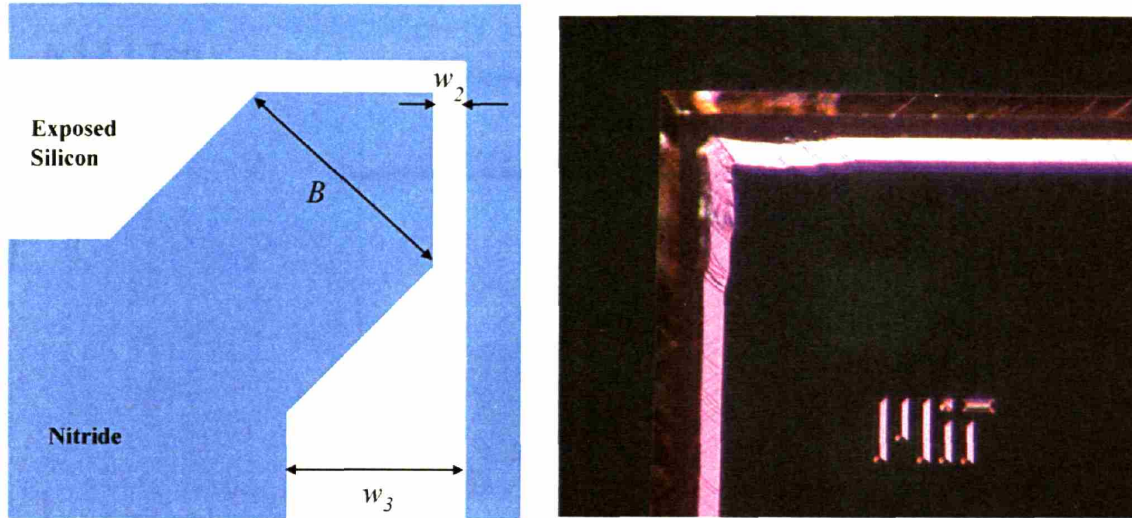
Figure A.7 The KOH corner compensation utilizes nitride "tabs" on exposed corners to slow etching under that area. The (411) crystal plane etch rate vs. the (100) etch rate ultimately determines the maximum depth of etching.
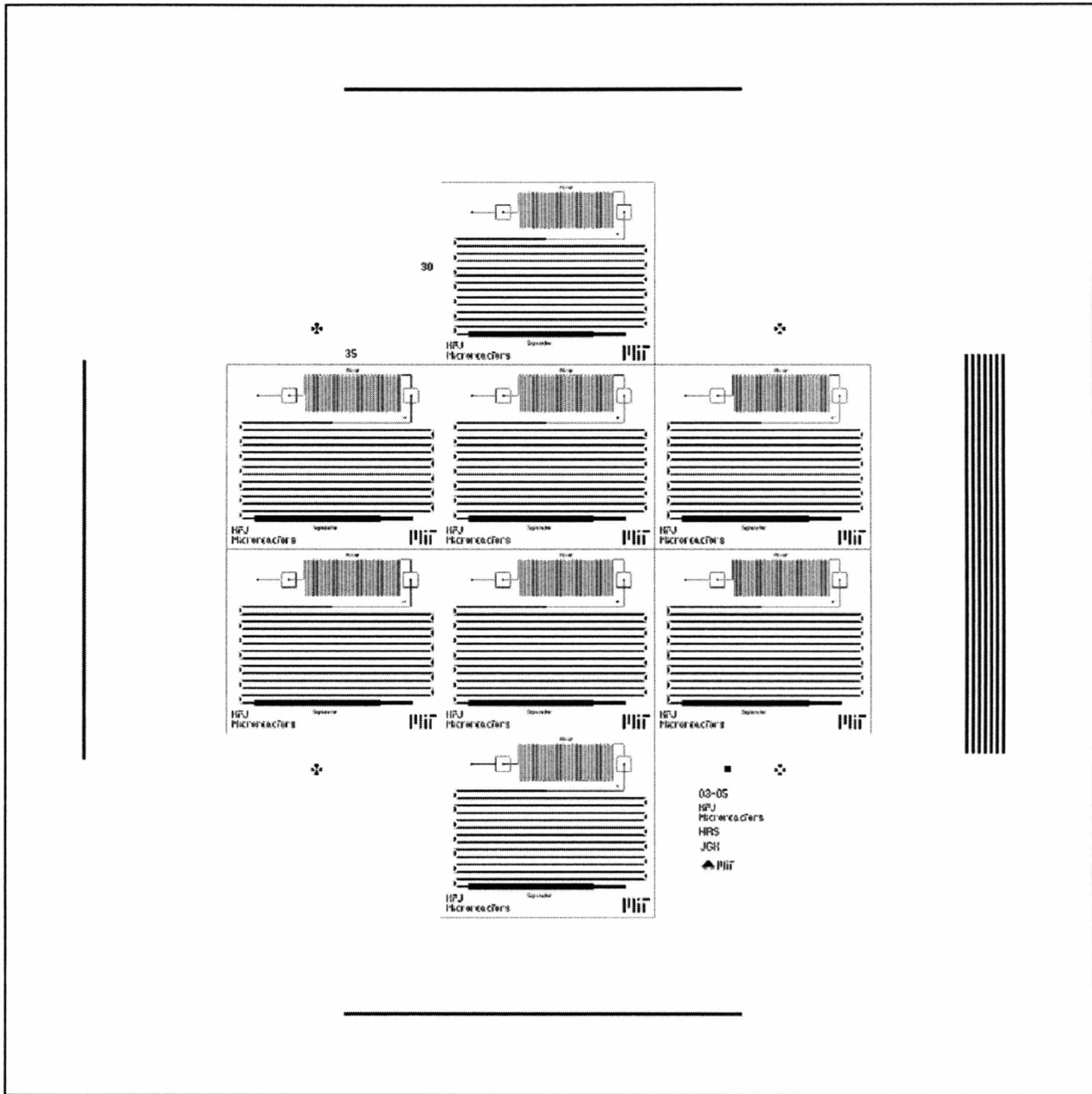
Figure A.8 Frontside layout of the 8 devices for a 150-mm wafer. The 7 lines to the right aide in alignment and orientation of the wafer flat which is along the (100) crystal plane.

A.3.2.2 Bottom
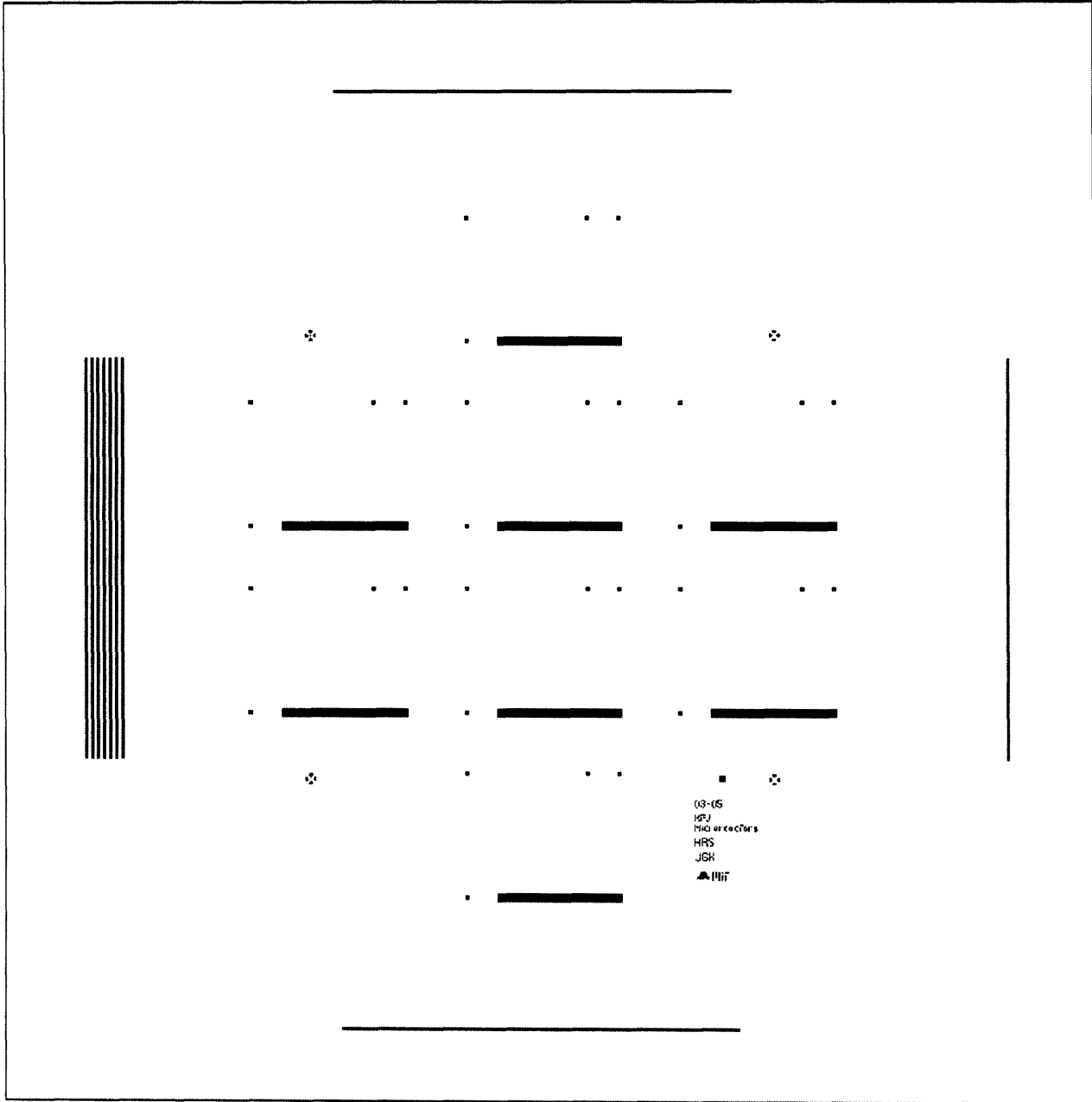
Figure A.9 The inlet and outlet ports with the separation trenches are visible. The alignment features were not visible for backside alignment and should have been nearer the centerline.

A.3.2.3 Membrane-only

The purpose of this device was to test the PTFE membrane with a hexane/water system. The chuck was machined from polycarbonate, which resists attack by hexanes, with 0.5x0.5 mm channel cross-sections. Each half of the device was outfitted with an inlet and outlet tapped with ¼"-28 screw fittings for tubing connections.
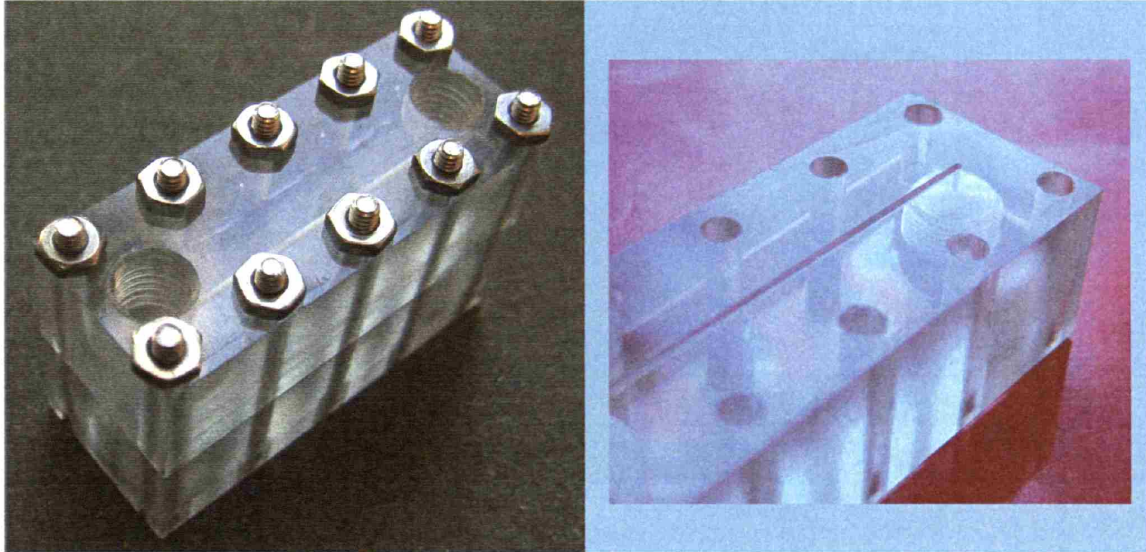
Figure A.10 The membrane-only microfluidic device machined from polycarbonate with a porous teflon membrane in compression (left). The 0.5x0.5 mm channel (right) was interfaced with 1/4"-28 fittings for simple packaging.

A.3.2.4 Integrated Silicon Device Fluid Chuck

The chuck was manufactured from glass-filled PTFE. This material is easier to machine, tougher, and is still practically inert compared with pure PTFE. Figure A.11 gives an isometric view of the construction with the final product. Recesses for the o-rings were machined to a depth level with the Zefluor membrane. This provides excellent sealing for all fluid pathways. The three inlets and two outlets were tapped with ¼"-28 threads and the top was ½" polycarbonate. A thick top plate is important to prevent breaking the device, as any bowing of the top will likely result in device failure.

137
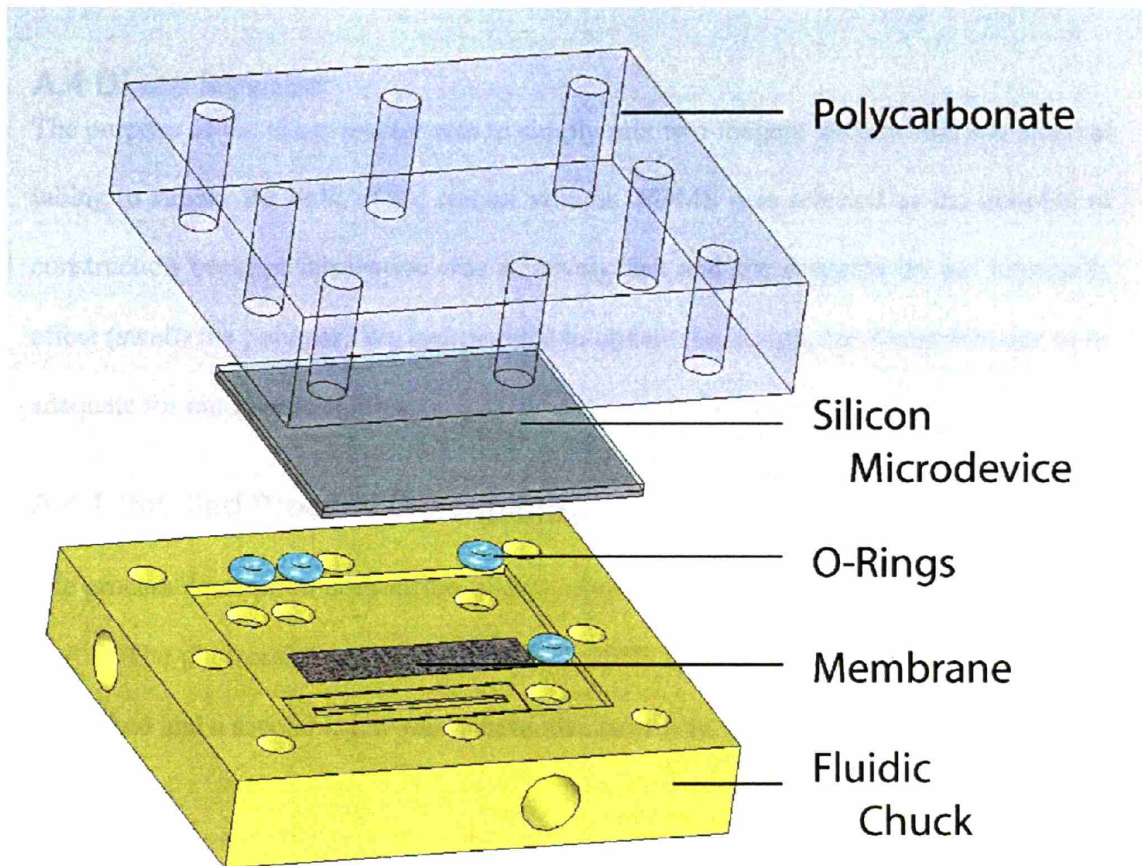
Figure A.11 Isometric view of fluid chuck for device packaging.

Polycarbonate

Silicon
Microdevice

O-Rings

Membrane

Fluidic
Chuck

A.4 Diazo Reactor

The purpose of the diazo reactor was to simply mix two reagent streams and use external tubing to supply the bulk of the reactor volume. PDMS was selected as the material of construction because fabrication was relatively fast and the reagents do not nominally affect (swell) the polymer. We had planned to update the design, but found this one to be adequate for our kinetic studies.

A.4.1 Detailed Process Description

The process description does differs slightly from the DEP device manufacture described in A.1. The photoresist was changed to SU8 2050, spun at 1000 rpm for 60s. This was soft baked and a second layer was spun on the same way, and prebaked before processing as before.

General process:
> The equipments used are the SU8spinner, the UV aligner and the hot plates.

Starting mat 4in Silicon wafers, Test grade, Single-side polished.

STEP	FAC	MACHINE	ACTION	NOTES	CODE
1			*Patterning of SU8 layer*		
1.1	TRL	hot plate	Dehydration bake @ 200 Celsius (20 min)		
1.2	TRL	SU8spinner	Spin coating of 100um thick SU8-2050 layer		
1.3	TRL	hot plate	Prebake (5 min @ 65 C and 45 min @ 95 C)		
1.4	TRL	SU8spinner	Spin coating of 100um thick SU8-2050 layer		
1.5	TRL	hot plate	Prebake (5 min @ 65 C and 45 min @ 95 C)		
1.6	TRL	EV1	UV Exposure (EV1, 8x5 seconds with 2s interval)		
1.7	TRL	hot plate	Bake (5 min @ 65 C and 30 min @ 95 C)		
2	TRL		*Development of the wafer*		
2.1		photowet-Au	Development in PGMEA	Takes 30-60 min. Use fresh developer about every 15 min with gentle agitation.	

A.4.2 Mask

The mask was drawn in AutoCAD LT 2002. The 100 μm wide channels are folded onto each other to minimize the footprint of the device and the flow was bifurcated once to improve the mixing rate.
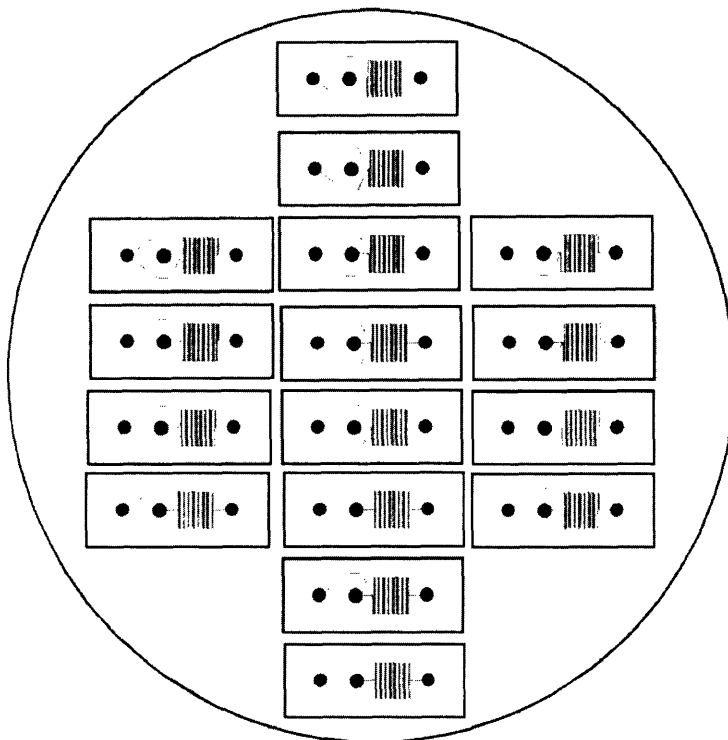
Figure A.12 SU8 Master negative image for the diazo kinetic experiments.

A.4.3 Packaging

The devices were sealed to a piece of silicon with roughly the same dimensions as the individual devices cut from PDMS. They were cleaned, plasma treated, and sealed in the exact same way as described in A.1.3. We also developed a way to epoxy seal PTFE tubing to the PDMS using metal ferrules as anchors. A metal ferrule was mechanically sealed to a piece of PTFE tubing about ¼" from the bottom so that the bottom of the

ferrule was just flush with the PDMS surface. Epoxy adheres well to the metal and plasma-treated PDMS surfaces, enabling good fluid seals while the fluid remains in contact with only PTFE and PDMS surfaces (Figure A.13).
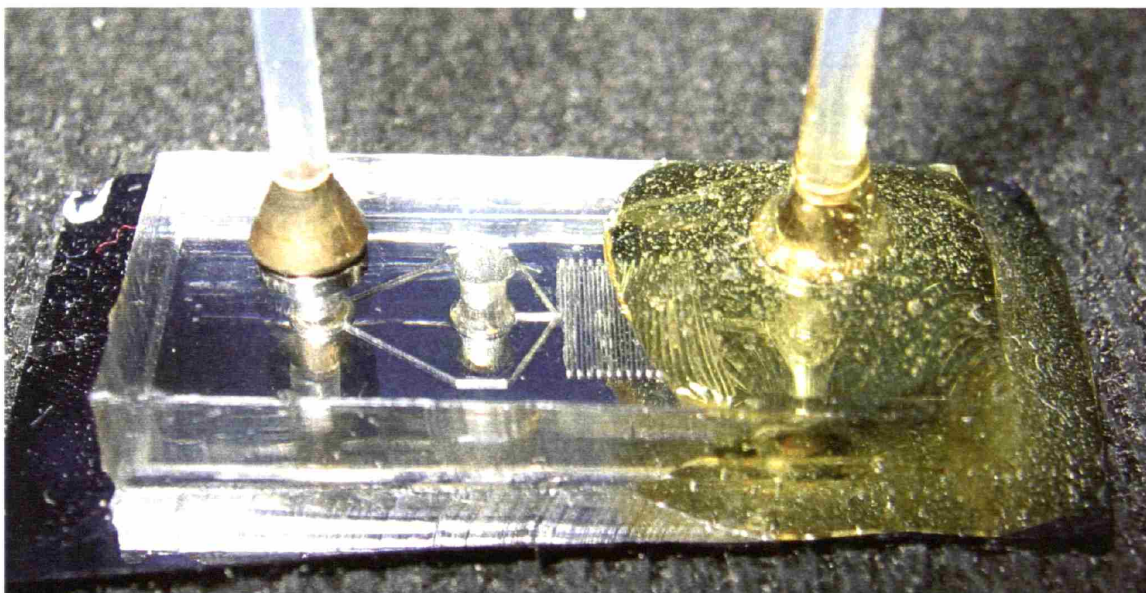
Figure A.13 Demonstration of fluidic coupling to PDMS device—the ferrule is attached to the PTFE tubing and inserted into a hole (left), then epoxied in place after plasma ashing (right).

Appendix B. Stability of Devices for Nitrotetrazole Reaction Studies

This appendix details the material selection for and stability of PDMS microdevices used in the kinetic studies of nitrotetrazole formation. The chemical compatibility of the PDMS, experimental observations, and fluid connection stability are discussed. Fabrication and packaging of these devices is described in Appendix A.

B.1 Material Selection

Chemical compatibility is a significant issue for the studies of tetrazole diazotization and substitution. In the first reaction step, sulfuric and nitrous acids are mixed to form the diazonium intermediate. We investigated the use of PDMS as the device material because of the straightforward fabrication process and found that it did not swell significantly in the presence of 1M sulfuric, hydrochloric, and nitric acids [103]. In the second step, high concentrations of sodium hydroxide are required to adjust the pH of the solution. Lee, et al. also found that 10M NaOH did not significantly swell the PDMS. It is worth noting that according to this study, few acids or bases had any strong effect on the swelling of PDMS other than pure dipropylamine, concentrated sulfuric acid, and pure trifluoroacetic acid, which all dissolved the PDMS.

The tubing connecting the devices was a fluorinated polymer. Some difficulty was encountered when attempting to package the fluoropolymer tubing to the devices as no epoxy could adhere to its surface. The packaging technique in Appendix A using metal ferrules to mechanically deform the tubing and provide an adherent surface was devised to overcome this challenge. The tubing itself is chemically stable for all acids and bases. Fluoropolymers are known to be significantly permeable to gases. [104] The second reaction produces nitrogen gas as a byproduct in small amounts, though we could not quantitatively say how this compared with theory. It was not studied in this work, but a significant amount of gas could permeate through the PTFE tubing and be continuously removed by drawing a vacuum on the exterior of the tubing. A similar principle is used for inline degassers for HPLC solvents.

B.2 PDMS Stability

During the course of a reaction, the PDMS did change appearance significantly (Figure B.1). The polymer changed from clear to an opaque milky white color over the course of ~ 1 hour. We speculated that nitrous oxide gas was responsible for this change, though we could find no reports in the literature to support this claim.
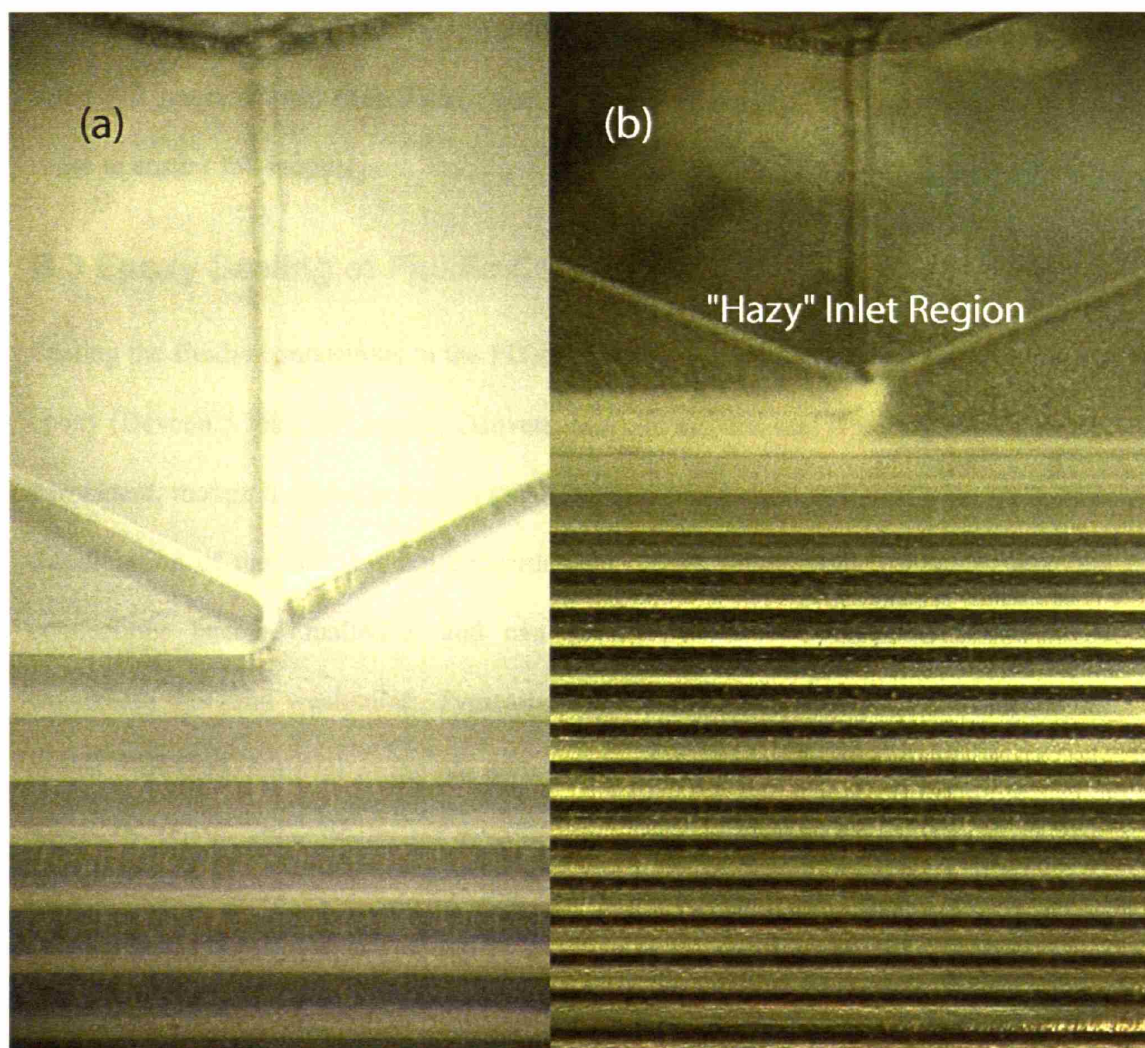
Figure B.1 A change in the appearance of the PDMS was observed in this device. In (a), the device has not been used and is clear. After running the device for some time, the inlet region becomes hazy (b).

We did find that the device could be recovered after some time, and placing the device in an oven seemed to help. This suggests that the substance dissolved in the PDMS is a liquid or a gas and not a salt.

No change in the flow behavior was observed over the course of an experiment. It may be that any swelling was slight and only enhanced mixing, or that the species partitioning into the PDMS did not do so significantly compared with the transport via convection. After ~ 3 hours of use, each device was dried and allowed to rest for 24 hours before reuse to ensure full recovery.

B.3 Epoxy Sealing of Fluidic Connections

Sealing the fluidic connections to the PDMS devices was achieved using two-component epoxy (Devcon 5 Minute® Epoxy; Danvers, MA). In air, this seal is very good and nearly permanent, though high temperatures (>50°C for several hours) will result in a yellowish discoloration of the material and embrittlement. When submerged in a water bath, the connections become malleable and can fail if pressurized. Elevated temperatures exacerbate this joint weakening. Typically, the connections fail after 2-10 experimental cycles. However, removal of the old epoxy and resealing with the procedure detailed in Appendix A does allow the device to be recycled ~3-4 times. This was acceptable for the kinetic experiments, but would be poor for long-term device operation for chemical production.

Literature Cited

1. Campbell, S.A., *The Science and Engineering of Microelecronic Fabrication*. 1996, New York: Oxford University Press.

2. Madou, M.J., *Fundamentals of Microfabrication*. 2nd ed. 2002, Boca Raton: CRC Press.

3. Wilhite, B.A., M.A. Schmidt, and K.F. Jensen, *Palladium-based micromembranes for hydrogen separation: Device performance and chemical stability*. Industrial & Engineering Chemistry Research, 2004. **43**(22): p. 7083-7091.

4. Arana, L.R., S.B. Schaevitz, A.J. Franz, M.A. Schmidt, and K.F. Jensen, *A microfabricated suspended-tube chemical reactor for thermally efficient fuel processing*. Journal of Microelectromechanical Systems, 2003. **12**(5): p. 600-612.

5. Losey, M.W., R.J. Jackman, S.L. Firebaugh, M.A. Schmidt, and K.F. Jensen, *Design and fabrication of microfluidic devices for multiphase mixing and reaction*. Journal of Microelectromechanical Systems, 2002. **11**(6): p. 709-717.

6. Ajmera, S.K., C. Delattre, M.A. Schmidt, and K.F. Jensen, *Microfabricated differential reactor for heterogeneous gas phase catalyst testing*. Journal of Catalysis, 2002. **209**(2): p. 401-412.

7. Rice, C., S. Ha, R.I. Masel, and A. Wieckowski, *Catalysts for direct formic acid fuel cells*. Journal of Power Sources, 2003. **115**(2): p. 229-235.

8. Ratner, D.M., E.R. Murphy, M. Jhunjhunwala, D.A. Snyder, K.F. Jensen, and P.H. Seeberger, *Microreactor-based reaction optimization in organic chemistry glycosylation as a challenge*. Chemical Communications, 2005(5): p. 578-580.

9. Pennemann, H., P. Watts, S.J. Haswell, V. Hessel, and H. Lowe, *Benchmarking of microreactor applications*. Organic Process Research & Development, 2004. **8**(3): p. 422-439.

10. Cullen, C.J., R.C.R. Wootton, and A.J. de Mello, *Microfluidic systems for high-throughput and combinatorial chemistry*. Current Opinion in Drug Discovery & Development, 2004. **7**(6): p. 798-806.

11. de Mas, N., A. Gunther, M.A. Schmidt, and K.F. Jensen, *Microfabricated multiphase reactors for the selective direct fluorination of aromatics*. Industrial & Engineering Chemistry Research, 2003. **42**(4): p. 698-710.

12. Mogensen, K.B., H. Klank, and J.P. Kutter, *Recent developments in detection for microfluidic systems*. Electrophoresis, 2004. **25**(21-22): p. 3498-3512.

13. Fortt, R., R.C.R. Wootton, and A.J. de Mello, *Continuous-flow generation of anhydrous diazonium species: Monolithic microfluidic reactors for the chemistry of unstable intermediates*. Organic Process Research & Development, 2003. **7**(5): p. 762-768.

14. Yamada, M., M. Nakashima, and M. Seki, *Pinched flow fractionation: Continuous size separation of particles utilizing a laminar flow profile in a pinched microchannel.* Analytical Chemistry, 2004. **76**(18): p. 5465-5471.

15. Lapizco-Encinas, B.H., B.A. Simmons, E.B. Cummings, and Y. Fintschenko, *Dielectrophoretic concentration and separation of live and dead bacteria in an array of insulators.* Analytical Chemistry, 2004. **76**(6): p. 1571-9.

16. Duerr, M., J. Kentsch, T. Mueller, T. Schnelle, and M. Stelzle, *Microdevices for manipulation and accumulation of micro- and nanoparticles by dielectrophoresis.* Electrophoresis, 2003. **24**(4): p. 722-731.

17. Dittrich, P.S. and P. Schwille, *An integrated microfluidic system for reaction, high-sensitivity detection, and sorting of fluorescent cells and particles.* Analytical Chemistry, 2003. **75**(21): p. 5767-5774.

18. Treybal, R.E., *Mass-Transfer Operations.* 3rd ed. 1981, London: McGraw-Hill.

19. Losey, M.W., M.A. Schmidt, and K.F. Jensen, *Microfabricated multiphase packed-bed reactors: Characterization of mass transfer and reactions.* Industrial & Engineering Chemistry Research, 2001. **40**(12): p. 2555-2562.

20. Burns, J.R. and C. Ramshaw, *The intensification of rapid reactions in multiphase systems using slug flow in capillaries.* Lab-on-a-chip, 2001. **1**: p. 10-15.

21. Wojik, A. and R. Marr, *Mikroverfahrenstechnicsche Prinzipien in der Fluessig/Fluessig-Extraktion.* Chemie Ingenieur Technik, 2005. **77**(6): p. 653-668.

22. Kralj, J.G., M.A. Schmidt, and K.F. Jensen, *Surfactant-enhanced liquid-liquid extraction in microfluidic channels with inline electric-field enhanced coalescence.* Lab on a Chip, 2005. **5**(5): p. 531-535.

23. Aota, A., M. Nonaka, A. Hibara, and T. Kitamori, *Micro counter-current flow system for highly efficient extraction.* Proceedings, 7th Intl. Conf. on Miniaturized Chem. and Biochem. Anal. Systems, 2003: p. 441-444.

24. Fang, Q., H. Chen, and Z.-X. Cai, *Stopped-flow liquid-liquid extraction on microfluidic chips.* Gaodeng Xuexiao Huaxue Xuebao, 2004. **25**(2): p. 261-263.

25. Tokeshi, M., T. Minagawa, and T. Kitamori, *Integration of a Microextraction System on a Glass Chip: Ion-Pair Solvent Extraction of Fe(II) with 4,7-Diphenyl-1,10-phenanthrolinedisulfonic Acid and Tri-n-octylmethylammonium Chloride.* Anal. Chem., 2000. **72**: p. 1711-1714.

26. Fair, J.R., D.E. Steinmeyer, W.R. Penney, and B.B. Crocker, *Gas Absorption and Gas-Liquid System Design*, in *Perry's Chemical Engineers' Handbook*, R.H. Perry and D.W. Green, Editors, McGraw-Hill: New York.

27. Jhunjhunwala, M., *Control of Fluid Path on Microscale*, in *Chemical Engineering.* 2003, Massachusetts Institute of Technology: Cambridge.

28. Gascoyne, P.R.C. and J. Vykoukal, *Particle separation by dielectrophoresis.* Electrophoresis, 2002. **23**(13): p. 1973-83.

147

29. Pohl, H.A., *The motion and precipitation of suspensoids in divergent electric fields.* Journal of Applied Physics, 1951. **22**: p. 869-71.

30. Jones, T., *Electromechanics of Particles.* 1995, Cambridge: Cambridge University Press.

31. Hughes, M., Electrophoresis, 2002. **23**: p. 2569-2582.

32. Becker, F.F., P.R.C. Gascoyne, Y. Huang, and X.-B. Wang, *Fractionation using dielectrophoresis and field flow fractionation*, in *PCT Int. Appl.* 1997. p. 86.

33. Huang, Y., X.-B. Wang, F.F. Becker, and P.R.C. Gascoyne, *Introducing dielectrophoresis as a new force field for field-flow fractionation.* Biophysical Journal, 1997. **73**(2): p. 1118-1129.

34. Wang, X.-B., J. Vykoukal, F.F. Becker, and P.R.C. Gascoyne, *Separation of polystyrene microbeads using dielectrophoretic/gravitational field-flow-fractionation.* Biophysical Journal, 1998. **74**(5): p. 2689-2701.

35. Yang, J., Y. Huang, X.-B. Wang, F.F. Becker, and P.R.C. Gascoyne, *Cell Separation on Microfabricated Electrodes Using Dielectrophoretic/Gravitational Field-Flow Fractionation.* Analytical Chemistry, 1999. **71**(5): p. 911-918.

36. Gascoyne, P.R.C. and J.V. Vykoukal, Proceedings of the IEEE, 2002. **92**(1).

37. Choi, S. and J.-K. Park, *Microfluidicsystem for dielectrophoretic separation based on a trapezoidal electrode array.* Lab on a Chip, 2005. **5**: p. 1161-1167.

38. Lapizco-Encinas, B., B. Simmons, E. Cummings, and Y. Fintschenko, Electrophoresis, 2004. **25**(10-11).

39. Voldman, J., M. Toner, M. Gray, and M. Schmidt, Journal of Electrostatics, 2003. **57**(1): p. 69-90.

40. Li, H., Y. Zheng, D. Akin, and R. Bashir, *Characterization and Modeling of a Microfluidic Dielectrophoresis Filter for Biological Species.* Journal of Microelectromechanical Systems, 2005. **14**(1): p. 103-112.

41. Rousselet, J., G. Markx, and R. Pethig, Colloids and Surfaces A - Physicochemical and Engineering Aspects, 1998. **140**(1-3): p. 209-216.

42. Suehiro, J. and R. Pethig, Journal of Physics D - Applied Physics, 1998. **31**(22): p. 3298-3305.

43. Pethig, R., V. Bressler, C. Carswell-Crumpton, Y. Chen, L. Foster-Haje, M. Garcia-Ojeda, R. Lee, G. Lock, M. Talary, and K. Tate, *Dielectrophoretic studies of the activation of human T lymphocytes using a newly developed cell profiling system.* Electrophoresis, 2002. **23**(13): p. 2057-2063.

44. Nieuwenhuis, J.H. and M.J. Vellekoop, Sensors and Actuators B, 2004. **103**: p. 331-338.

45. Albrecht, D., S. Sah, and S. Bhatia, Biophysical Journal, 2004. **87**: p. 2131-2147.

46.	Duffy, D.C., J.C. McDonald, O.J.A. Schueller, and G.M. Whitesides, *Rapid Prototyping of Microfluidic Systems in Poly(dimethylsiloxane)*. Analytical Chemistry, 1998. **70**(23): p. 4974-4984.

47.	Khusid, B. and A. Acrivos, *Effects of interparticle interactions on dielectophoresis in colloidal suspensions*. Physical Review E, 1996. **54**(5): p. 5428-5435.

48.	Padua, G.W., *Proton NMR and Dielectric Measurements on Sucrose Filled Agar Gels and Starch Pastes*. Journal of Food Science, 1993. **58**(3): p. 603-4.

49.	Deen, W., *Analysis of Transport Phenomena*. 1998: Oxford.

50.	Happel, J. and H. Brenner, *Low Reynolds Number Hydrodynamics*. 2nd ed. Vol. Netherlands. 1991, Dorecht: Kluwer Academic.

51.	Auroux, P.-A., D. Iossifidis, D.R. Reyes, and A. Manz, Anal. Chem., 2002. **74**: p. 2637-2652.

52.	Burns, J.R. and C. Ramshaw, *A microreactor for the nitration of benzene and toluene*. Chemical Engineering Communications, 2002. **189**(12): p. 1611-1628.

53.	Ueno, M., H. Hisamoto, T. Kitamori, and S. Kobayashi, *Phase-transfer alkylation reactions using microreactors*. Chemical Communications, 2003: p. 936-937.

54.	Cottrell, F.G. and J.B. Speed, *Separating and collecting particles of one liquid suspended in another*. US Patent, 1911. **987 115**.

55.	Eow, J.S. and M. Ghadiri, *Electrostatic enhancement of coalescence of water droplets in oil: a review of the technology*. Chemical Engineering Journal, 2002. **85**: p. 357-368.

56.	Zhang, X. and O.A. Basaran, *Electric Field-Enhanced Coalescence of Liquid Drops*. Separation Science and Technology, 1995. **30**(7-9): p. 1169-1187.

57.	Fadnavis, N.W., B. Satyavathi, and A.A. Deshpande, *Reverse micellar extraction of antibiotics from aqueous solutions*. Biotechnology Progress, 1997. **13**(4): p. 503-505.

58.	Pandit, P. and S. Basu, *Removal of organic dyes from water by liquid-liquid extraction using reverse micelles*. Journal of Colloid and Interface Science, 2002. **245**(1): p. 208-214.

59.	Haverkamp, V., W. Ehrfeld, K. Gebauer, V. Hessel, H. Lowe, T. Richter, and C. Wille, Fresenius Journal of Analytical Chemistry, 1999. **364**(7): p. 617-624.

60.	Umbanhowar, P., V. Prasad, and D. Weitz, Langmuir, 2000. **16**(2): p. 347-351.

61.	Davis, M.H., *Two Charged Spherical Conductors in a Uniform Electric Field: Forces and Field Strength*. Quart. Journ. Mech. and Applied Math., 1964. **XVII**(4).

62.	Zeng, J. and T. Korsmeyer, *Principles of droplet electrohydrodynamics for lab-on-a-chip*. Lab on a Chip, 2004. **4**: p. 265-277.

63. Langkruis, G.B. and J.B.F.N. Engberts, *Partitioning of Organic Solutes Between the Micellar and the Aqueous Phase as Studied with an Artificial Kidney.* Tetrahedron Letters, 1979. **20**(41): p. 3991-3994.

64. Guenther, A., M. Jhunjhunwala, M. Thalmann, M.A. Schmidt, and K.F. Jensen, *Micromixing of Miscible Liquids in Segmented Gas-Liquid Flow.* Langmuir, 2005. **21**(4): p. 1547-1555.

65. Hisamoto, H., M. Tokeshi, A. Hibara, and T. Kitamori, *Molecular transport and extraction in liquid microspace - a key to develop microchemical systems.* Journal of Ion Exchange, 2003. **14**(1): p. 38-43.

66. Maruyama, T., T. Kaji, T. Ohkawa, K.-i. Sotowa, H. Matsushita, F. Kubota, N. Kamiya, K. Kusakabe, and M. Goto, *Intermittent partition walls promote solvent extraction of metal ions in a microfluidic device.* Analyst (Cambridge, United Kingdom), 2004. **129**(11): p. 1008-1013.

67. Maruyama, T., H. Matsushita, J.-i. Uchida, F. Kubota, N. Kamiya, and M. Goto, *Liquid Membrane Operations in a Microfluidic Device for Selective Separation of Metal Ions.* Analytical Chemistry, 2004. **76**(15): p. 4495-4500.

68. Tokeshi, M., T. Minagawa, K. Uchiyama, A. Hibara, K. Sato, H. Hisamoto, and T. Kitamori, *Continuous-Flow Chemical Processing on a Microchip by Combinging Microunit Operations and a Multiphase Flow Network.* Anal. Chem., 2002. **74**: p. 1565-1571.

69. Asami, K., K. Kuwabara, and K. Ohtaguchi, *Study on the partitioning extraction of protein under microflow aqueous polymer two-phase systems.* Kagaku Kogaku Ronbunshu, 2004. **30**(2): p. 164-168.

70. Benz, K., K.-P. Jaeckel, K.-J. Regenauer, J. Schiewe, K. Drese, W. Ehrfeld, V. Hessel, and H. Loewe, *Utilization of micromixers for extraction processes.* Chemical Engineering & Technology, 2001. **24**(1): p. 11-17.

71. Kumemura, M. and T. Korenaga, *Liquid-liquid extraction in microfluidic system using dispersed liquid droplet.* AIP Conference Proceedings, 2004. **708**(Slow Dynamics in Complex Systems): p. 104-105.

72. Martin, P.M., D.W. Matson, and W.D. Bennett. *Microfabrication Methods for Microchannel Reactors and Separations Systems.* in *Process Miniaturization: 2nd International Converence on Microreaction Technology.* 1998. New Orleans, LA: AIChE.

73. Sawai, H., *Development of microextraction device for biochemically active substances by reversed micelle extraction in laminar flow,* in *Jpn. Kokai Tokkyo Koho.* 2004, (Sumitomo Bakelite Co., Ltd., Japan). Jp. p. 6 pp.

74. Shaw, J., R. Nudd, B. Naik, C. Turner, D. Rudge, M. Benson, and A. Garman, *Liquid/liquid extraction systems using micro-contactor arrays.* Micro Total Analysis Systems 2000, Proceedings of the mTAS Symposium, 4th, Enschede, Netherlands, May 14-18, 2000, 2000: p. 371-374.

75. Wenn, D.A., J.E.A. Shaw, and B. Mackenzie, *A mesh microcontactor for 2-phase reactions.* Lab on a Chip, 2003. **3**(3): p. 180-186.

76. Khan, S.A., A. Guenther, M.A. Schmidt, and K.F. Jensen, *Microfluidic Synthesis of Colloidal Silica.* Langmuir, 2004. **20**(20): p. 8604-8611.

77. Guenther, A., K.F. Jensen, M. Jhunjhunwala, and M.A. Schmidt, *Fluid separation*, in *PCT Int. Appl.* 2004, Massachusetts Institute of Technology, USA: Wo. p. 49 pp.

78. TeGrotenhuis, W., R. Wegeng, G. Whyatt, V. Stenkamp, and P. Gauglitz, *Microsystem Capillary Separations.* 2003.

79. Zhang, Q., L. Liu, and Z. Li, *A new approach to convex corner compensation for anisotropic etching of (100) Si in KOH.* Sensors and Actuators A, 1996. **56**: p. 251-254.

80. Mayer, G.K., H.L. Offereins, H. Sandmaier, and K. Kuehl, *Fabrication of Non-Underetched Convex Corners in Anisotropic Etching of (100)-Silicon in Aquoeous KOH with Respect to Novel Micromechanical Elements.* Journal of the Electrochemical Society, 1990. **137**(12): p. 3947-3950.

81. Brittain, S., S. Ficarro, A. Brock, and E. Peters, *Enrichment and analysis of peptide subsets using fluorous affinity tags and mass spectrometry.* Nature Biotechnology, 2005. **23**(4): p. 463-468.

82. Zhang, W., *Fluorous synthesis of heterocyclic systems.* Chemical Reviews, 2004. **104**(5): p. 2531-2556.

83. Skrzecz, A., D. Shaw, and A. Maczynski, *IUPAC-NIST Solubility Data Series 69. Ternary Alcohol-Hydrocarbon-Water Systems.* Journal of Physical Chemistry Reference Data, 1999. **28**(4): p. 983-1223.

84. Floyd, T., *A Novel Microchemical System for Rapid Liquid-Liquid Chemistry*, in *Chemical Engineering.* 2001, MIT: Cambridge, MA.

85. Hessel, V., H. Lowe, and F. Schonfeld, *Micromixers - a review on passive and active mixing principles.* Chemical Engineering Science, 2005. **60**(8-9): p. 2479-2501.

86. Kreutzer, M.T., F. Kapteijn, J.A. Moulijn, and J.J. Heiszwolf, *Multiphase monolith reactors: Chemical reaction engineering of segmented flow in microchannels.* Chemical Engineering Science, 2005. **60**: p. 5895-5916.

87. Characteristic values of the model parameters: D = 10-9 m2/s, dhyd = 157 m, L1+L2 = 40dhyd, U = 21 mm/s

88. Sorenson, J.M. and W. Arlt, *Liquid-Liquid Equilibrium Data Collection*, ed. DECHEMA. 1979, Frankfurt.

89. Karpenko, G.V., A.B. Koshokov, N.Y. Koryakov, G.M. Poltoratskii, and V.L. Rogachev, *Liquid-phase equilibrium in the water-dimethylformamide-organic solvent three-component systems.* Zhurnal Prikladnoi Khimii (Sankt-Peterburg, Russian Federation), 1979. **52**(9): p. 2109-12.

90. Ehrfeld, W., K. Golbig, V. Hessel, H. Lowe, and T. Richter, *Characterization of mixing in micromixers by a test reaction: Single mixing units and mixer arrays.* Industrial & Engineering Chemistry Research, 1999. **38**(3): p. 1075-1082.

91. Fletcher, P.D.I., S.J. Haswell, E. Pombo-Villar, B.H. Warrington, P. Watts, S.Y.F. Wong, and X.L. Zhang, *Micro reactors: principles and applications in organic synthesis.* Tetrahedron, 2002. **58**(24): p. 4735-4757.

92. Kikutani, Y., T. Horiuchi, K. Uchiyama, H. Hisamoto, M. Tokeshi, and T. Kitamori, *Glass microchip with three-dimensional microchannel network for 2 x 2 parallel synthesis.* Lab on a Chip, 2002. **2**: p. 188-192.

93. Ostrovskii, V.A.K., G. I., *Energetic Tetrazoles.* Rossiiskii Khimicheskii Zhurnal, 1997. **41**(2): p. 84-98.

94. Shevlin, P.B., *Formation of atomic carbon in the decomposition of 5-tetrazolyldiazonium chloride.* Journal of the American Chemical Society, 1972. **94**(4): p. 1379-80.

95. Hegarty, A.F., *Kinetics and mechanisms of reactions involving diazonium and diazo groups*, in *The chemistry of diazonium and diazo groups*, S. Patai, Editor. 1978, Wiley: Chichester.

96. Eberhardt, K., S. Andersson, C. Ekberg, B. Horn, J.V. Kratz, P. Loeb, M. Nilsson, G. Skarnemark, and N. Trautmann, *Extraction of Gd ,Hf, and Tc with the fast and continuous liquid-liquid-extraction System MicroSISAK*, in *Institut fuer Kernchemie Annual Report.* 2004, Universitaet Mainz.

97. Wang, X.S., C.; Mitra, S., *Microfluidic supported liquid membrane extraction.* Analytica Chimica Acta, 2005. **543**: p. 92-98.

98. Peterson, G.P. and M. H.B., *Temperature Response of Heat Transport in a Micro Heat Pipe.* Transaction of the ASME, 1999. **121**: p. 438-445.

99. Ramirez-Gonzalez, E.A., C. Martinez, and J. Alvarez, *Modleing Zero-Gravity Distillation.* Industrial and Engineering Chemistry Research, 1992. **31**: p. 901-908.

100. Tien, C.L. and A.R. Rohani, *Theory of Two-component Heat Pipes.* Journal of Heat Transfer, 1972. **94**(4): p. 479-484.

101. Hibara, A., K. Toshin, T. Tsukahara, K. Mawatari, and T. Kitamori. *Micro Distillation System on Chip Utilizing Selective Modification Gas-Liquid Separator and Capillary Condensation in Nanostructure.* in *Micro Total Analysis Systems.* 2005. Boston, MA.

102. Haswell, S.J. and V. Skelton, *Chemical and biochemical microreactors.* Trends in Analytical Chemistry, 2000. **19**(6): p. 389-395.

103. Lee, J.N., C. Park, and G.M. Whitesides, *Solvent Compatibility of Poly(dimethylsiloxane)-Based Microfluidic Devices.* Analytical Chemistry, 2003. **75**: p. 6544-6554.

104.   Dobson, J.V. and M.J. Taylor, *The permeability of gases through PTFE and other membranes at 25C.* Electrochimica Acta, 1985. **31**(2): p. 231-3.